SMART MATERIALS FOR ENERGY CONVERSION AND SENSOR BASED TECHNOLOGIES

EDITED BY: Mahendra Dashrath Shirsat, Bhaskar R. Sathe and Pankaj Madhukar Koinkar

PUBLISHED IN: Frontiers in Materials

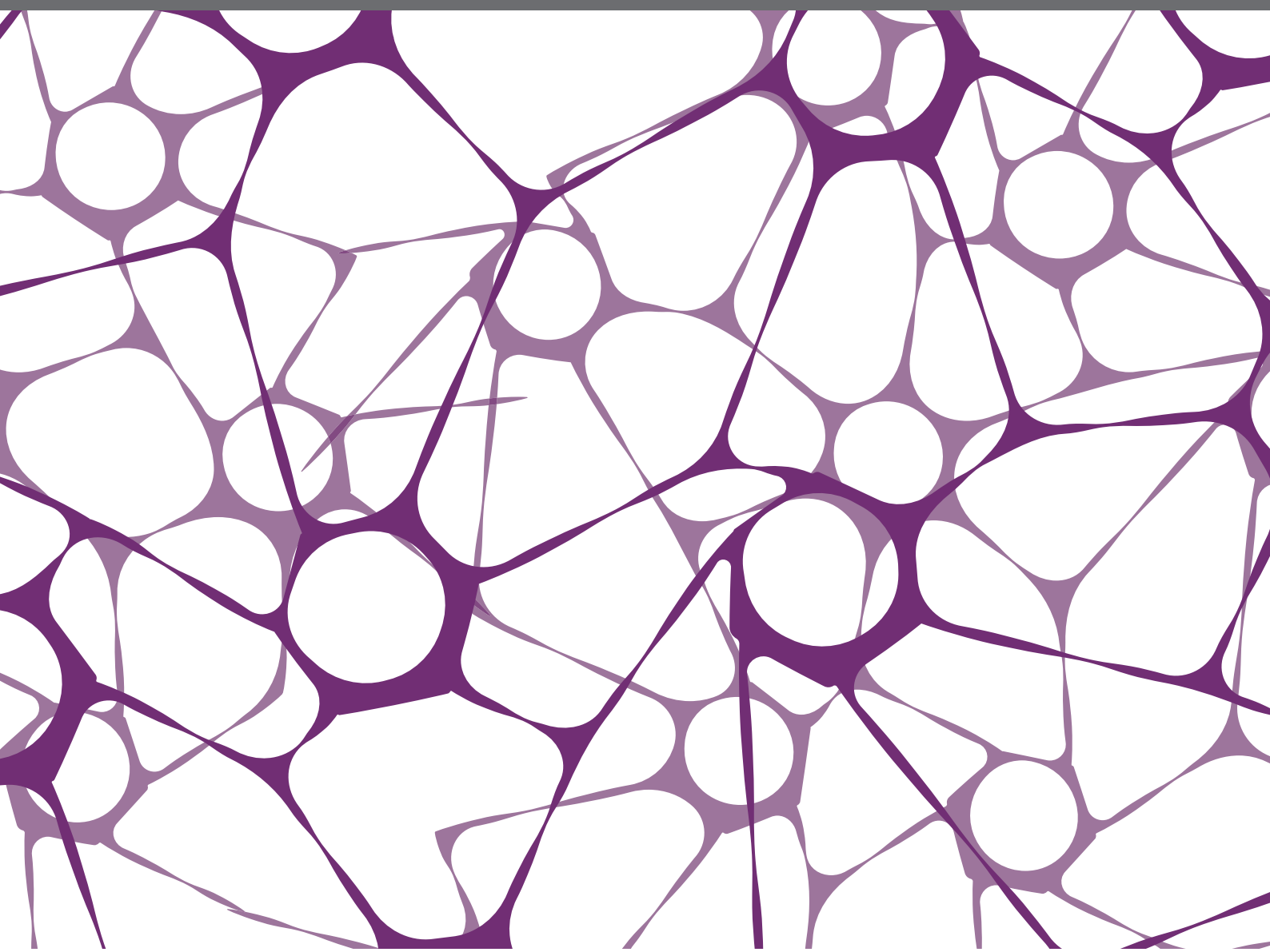

frontiers Research Topics

frontiers

ISSN 1664-8714
ISBN 978-2-88966-777-2
DOI 10.3389/978-2-88966-777-2

About Frontiers

Frontiers is more than just an open-access publisher of scholarly articles: it is a pioneering approach to the world of academia, radically improving the way scholarly research is managed. The grand vision of Frontiers is a world where all people have an equal opportunity to seek, share and generate knowledge. Frontiers provides immediate and permanent online open access to all its publications, but this alone is not enough to realize our grand goals.

Frontiers Journal Series

The Frontiers Journal Series is a multi-tier and interdisciplinary set of open-access, online journals, promising a paradigm shift from the current review, selection and dissemination processes in academic publishing. All Frontiers journals are driven by researchers for researchers; therefore, they constitute a service to the scholarly community. At the same time, the Frontiers Journal Series operates on a revolutionary invention, the tiered publishing system, initially addressing specific communities of scholars, and gradually climbing up to broader public understanding, thus serving the interests of the lay society, too.

Dedication to Quality

Each Frontiers article is a landmark of the highest quality, thanks to genuinely collaborative interactions between authors and review editors, who include some of the world's best academicians. Research must be certified by peers before entering a stream of knowledge that may eventually reach the public - and shape society; therefore, Frontiers only applies the most rigorous and unbiased reviews.
Frontiers revolutionizes research publishing by freely delivering the most outstanding research, evaluated with no bias from both the academic and social point of view. By applying the most advanced information technologies, Frontiers is catapulting scholarly publishing into a new generation.

What are Frontiers Research Topics?

Frontiers Research Topics are very popular trademarks of the Frontiers Journals Series: they are collections of at least ten articles, all centered on a particular subject. With their unique mix of varied contributions from Original Research to Review Articles, Frontiers Research Topics unify the most influential researchers, the latest key findings and historical advances in a hot research area! Find out more on how to host your own Frontiers Research Topic or contribute to one as an author by contacting the Frontiers Editorial Office: frontiersin.org/about/contact

SMART MATERIALS FOR ENERGY CONVERSION AND SENSOR BASED TECHNOLOGIES

Topic Editors:
Mahendra Dashrath Shirsat, Dr. Babasaheb Ambedkar Marathwada University, India
Bhaskar R. Sathe, Dr. Babasaheb Ambedkar Marathwada University, India
Pankaj Madhukar Koinkar, Tokushima University, Japan

Citation: Shirsat, M. D., Sathe, B. R., Koinkar, P. M., eds. (2021). Smart Materials for Energy Conversion and Sensor Based Technologies. Lausanne: Frontiers Media SA. doi: 10.3389/978-2-88966-777-2

Table of Contents

04 ***Editorial: Smart Materials for Energy Conversion and Sensor Based Technologies***

Mahendra Dashrath Shirsat, Bhaskar R. Sathe and Pankaj Madhukar Koinkar

06 ***Electrochemical Sensor: L-Cysteine Induced Selectivity Enhancement of Electrochemically Reduced Graphene Oxide–Multiwalled Carbon Nanotubes Hybrid for Detection of Lead (Pb^{2+}) Ions***

Theeazen AL-Gahouari, Gajanan Bodkhe, Pasha Sayyad, Nikesh Ingle, Manasi Mahadik, Sumedh M. Shirsat, Megha Deshmukh, Nadeem Musahwar and Mehendra Shirsat

19 ***EDTA Modified PANI/GO Composite Based Detection of Hg (II) Ions***

Manasi Mahadik, Harshada Patil, Gajanan Bodkhe, Nikesh Ingle, Pasha Sayyad, Theeazen Al-Gahaouri, Sumedh M. Shirsat and Mahendra Shirsat

27 ***Sulfur Dioxide (SO_2) Detection Using Composite of Nickel Benzene Carboxylic (Ni_3BTC_2) and OH-Functionalized Single Walled Carbon Nanotubes (OH-SWNTs)***

Nikesh Ingle, Savita Mane, Pasha Sayyad, Gajanan Bodkhe, Theeazen AL-Gahouari, Manasi Mahadik, Sumedh Shirsat and Mahendra D. Shirsat

34 ***PANI-ZnO Cladding-Modified Optical Fiber Biosensor for Urea Sensing Based on Evanescent Wave Absorption***

S. N. Botewad, V. G. Pahurkar, G. G. Muley, D. K. Gaikwad, Gajanan A. Bodkhe, Mahendra D. Shirsat and P. P. Pawar

43 ***Martensitic Transition, Magnetic, Microstructural and Exchange Bias Properties of Melt Spun Ribbons of Mn-Ni-Sn Shape Memory Heusler Alloy***

Jyoti Sharma, K. G. Suresh, M. Manivel Raja and Pravin Walke

frontiers in Materials

EDITORIAL
published: 25 March 2021
doi: 10.3389/fmats.2021.626397

Editorial: Smart Materials for Energy Conversion and Sensor Based Technologies

Mahendra Dashrath Shirsat[1]*, *Bhaskar R. Sathe*[1] and *Pankaj Madhukar Koinkar*[2]

[1] Department of Physics, Dr. Babasaheb Ambedkar Marathwada University, Aurangabad, India, [2] Department of Optical Science, Tokushima University, Tokushima, Japan

Keywords: smart materials, sensor, energy devices, catalyst, heavy metal

Editorial on the Research Topic

Editorial: Smart Materials for Energy Conversion and Sensor Based Technologies

It is a matter of great pride and gratification to come up with special issue of Frontiers in Materials: Smart Materials for Energy Conversion and Sensor Based Technologies.

Research articles covering the following topics (but not limited to) were invited for this special issue.

i) Nanomaterials for chemical and electrochemical sensors (gas, heavy metals, biomolecules, and other intermediates), energy conversion, storage, and utilization;
ii) Transition metal and carbon nanomaterials based photocatalysts and electrocatalysts;
iii) Electrochemical biosensors;
iv) Principle of electrochemical biosensors;
v) Electrochemical detection techniques;
vi) Potentiometric biosensors;
vii) Amperometric biosensors;
viii) Impedimetric biosensors;
ix) 2D material-based electrochemistry;
x) Mechanism of electrochemical sensing in nanomaterials-based electrodes;
xi) Hybrid biosensors;
xii) Nanostructures, nanofabrication, and nanoprobes by electrochemical sensing modality.

Smart Materials are at the forefront of scientific and technological exploration today. Continuous pursuit toward an in-depth understanding of the structure, properties, and employability of such materials has led to hitherto untrodden horizons by synergistic involvement of multidisciplinary research areas. The wide spectrum of smart materials includes metallic materials, ceramic materials, polymeric materials, nanocomposite materials, and biomedical materials. Researchers working on nanomaterials, in the last two decades, have invaluably contributed in the fields of photo-catalysts, electro-catalysts, lithium/sodium ion batteries, chemical sensors, supercapacitors, and their quantum of findings found successful technology conversions toward meeting continuously changing demands in the sectors of energy and environment.

The special issue of the Frontiers in Materials entitled **Smart Materials for Energy Conversion and Sensor-Based Technologies** has provided multidisciplinary research opportunity to present the results on the development in the field of smart materials for energy conversion and sensor-based technologies. This platform has played vital role in bringing prominent scientists, researchers, and scholars across the globe.

OPEN ACCESS

Edited and reviewed by:
Weihua Li,
University of Wollongong, Australia

****Correspondence:***
Mahendra Dashrath Shirsat
mdshirsat@gmail.com

Specialty section:
This article was submitted to Smart Materials, a section of the journal Frontiers in Materials

Received: *05 November 2020*
Accepted: *04 March 2021*
Published: *25 March 2021*

Citation:
Shirsat MD, Sathe BR and Koinkar PM (2021) Editorial: Smart Materials for Energy Conversion and Sensor Based Technologies. Front. Mater. 8:626397. doi: 10.3389/fmats.2021.626397

Nanostructure based chemical sensors have a significant contribution to critical as well as trivial characteristics of science, engineering, and technology. The identification based on accuracy, sensitivity, and reliability of different gas species/volatile organic compounds is very much essential in various field, for example, industrial and agricultural plants, food sciences, or environmental monitoring. In the past decade, chemical sensors based on nanomaterials have attracted many research scholars throughout the world because of their extraordinary sensing performance. At the same time, various challenges in the form of sensitivity, selectivity, quick response, robustness, and additional aspects have kept aplenty windows open for research and development in the area of nanostructured chemical sensor devices. Technological advancement in the area of development of an improved and new version of equipments has provided excellent opportunities for the development of emerging materials for various applications. At the same continuous efforts need to be directed toward understanding the properties of various function materials and their processes. And fundamentally, knowledge on sensing mechanisms has to be highly improved by the help of sound theoretical models and advance probing tools e.g., spectroscopic technologies. This special issue has given special emphasis on the articles having an exploration of smart materials for energy conversion and sensor based technologies.

We are quite sure that this special issue will be playing a role catalyst to have a more extensive exploration of materials for various technological applications to address unresolved issues of society.

AUTHOR CONTRIBUTIONS

All authors listed have made a substantial, direct and intellectual contribution to the work, and approved it for publication.

ACKNOWLEDGMENTS

We sincerely thanks frontiers for allowing us edit the special issue.

Conflict of Interest: The authors declare that the research was conducted in the absence of any commercial or financial relationships that could be construed as a potential conflict of interest.

frontiers in Materials

ORIGINAL RESEARCH
published: 31 March 2020
doi: 10.3389/fmats.2020.00068

Electrochemical Sensor: L-Cysteine Induced Selectivity Enhancement of Electrochemically Reduced Graphene Oxide–Multiwalled Carbon Nanotubes Hybrid for Detection of Lead (Pb^{2+}) Ions

*Theeazen AL-Gahouari[1,2], Gajanan Bodkhe[1], Pasha Sayyad[1], Nikesh Ingle[1], Manasi Mahadik[1], Sumedh M. Shirsat[3], Megha Deshmukh[1], Nadeem Musahwar[2] and Mehendra Shirsat[1]**

[1] Department of Physics, RUSA Center for Advanced Sensor Technology, Dr. Babasaheb Ambedkar Marathwada University, Aurangabad, India, [2] Department of Physics, University of Aden, Aden, Yemen, [3] Department of Electronics and Telecommunication Engineering, Jawaharlal Nehru Engineering College, Aurangabad, India

OPEN ACCESS

Edited by:
Xun Yu,
New York Institute of Technology,
United States

Reviewed by:
Zhaohong Su,
Hunan Agricultural University, China
Xiaoquan Lu,
Northwest Normal University, China

***Correspondence:**
Mehendra Shirsat
mdshirsat.phy@bamu.ac.in

Specialty section:
This article was submitted to Smart Materials, a section of the journal Frontiers in Materials

Received: 10 December 2019
Accepted: 04 March 2020
Published: 31 March 2020

Citation:
AL-Gahouari T, Bodkhe G, Sayyad P, Ingle N, Mahadik M, Shirsat SM, Deshmukh M, Musahwar N and Shirsat M (2020) Electrochemical Sensor: L-Cysteine Induced Selectivity Enhancement of Electrochemically Reduced Graphene Oxide–Multiwalled Carbon Nanotubes Hybrid for Detection of Lead (Pb^{2+}) Ions. Front. Mater. 7:68. doi: 10.3389/fmats.2020.00068

The selectivity improvement of Electrochemically reduced Graphene Oxide–Multiwalled Carbon Nanotubes–L-cysteine (ErGO–MWNTs–L-cys) nanocomposite modified Glassy Carbon Electrode (GCE) using drop casting method for electrochemical detection of lead (Pb^{2+}) ions was investigated. Initially, the graphene oxide–Multiwalled Carbon Nanotubes–L-cysteine (GO–MWNTs–L-cys) nanocomposite was synthesized by a facile and cost-effective method at room temperature. The as-prepared, GO–MWNTs–L-cys exhibited good stable aqueous dispersions due to high hydrophilic nature of GO components which led to inhibiting the hydrophobicity of MWNTs. Then, the electrochemical conductivity of ErGO–MWNTs–L-cys nanocomposite modified GCE (ErGO–MWNTs–L-cys/GCE) was improved by the direct electrochemical reduction of GO–MWNTs–L-cys nanocomposite. The GO–MWNTs–L-cys nanocomposites and its individual components were characterized by Attenuated Total Reflection Infrared (ATR-IR), Ultraviolet–visible spectroscopy, Raman spectroscopy, Atomic Force Microscopy, and X-ray diffraction (XRD). The synergistic effect of ErGO–MWNTs–L-cys nanocomposite was confirmed by Cyclic Voltammetry (CV) and Electric Impedance Spectroscopy (EIS) measurements in $[Fe(CN)_6]^{3-/4-}$ redox. Experimental parameters, such as pH, accumulation time and electrochemical reduction degrees, were optimized. Under optimal conditions, the electrochemical performance of modified electrodes toward Pb^{2+} ions was examined and it exhibited appreciable improvement at the ErGO–MWNTs–L-cys/GCE. In terms of applications, Differential Pulse Anodic Stripping Voltammetry (DPASV) was employed for the determination of Pb^{2+} ions on ErGO–MWNTs–L-cys/GCE. The calibration plots between anodic current and

Pb^{2+} ions exhibited linear relationship in the range of 0.2–40 μgL^{-1} with the detection limit calculated to be 0.1 μgL^{-1} (S/N = 3). Finally, the ErGO–MWNTs–L-cys/GCE showed satisfied selectivity and stable results, and the Relative Standard Deviation (RSD) was calculated to be (RSD = 2.15%).

Keywords: electrochemical reduction, graphene oxide, multiwalled carbon nanotubes, L-cysteine, nanocomposite, electrochemical conductivity, differential pulse anodic stripping voltammetry, Pb^{2+} ions detection

INTRODUCTION

Over the recent decade, the Heavy Metal Ions (HMIs) have been noticeably diffused into the environment from industrial activities such as electroplating, batteries, and geochemical mechanisms (Tinsley, 2004; Liu et al., 2011; Tiwari et al., 2011; Tongesayi et al., 2013; Adarakatti et al., 2017). Among the (HMIs), Pb^{2+} is of a great concern because of its severe risks to human health such as damaging human immune system, reproductive toxicity, respiratory disorders, negative effects on metabolism, and liver damage (Lee et al., 2007; Wang et al., 2007; Quang and Kim, 2010; Wan et al., 2010; Deshmukh et al., 2017a,b; Deshmukh et al., 2018a,b,c). Therefore, it is indigence to detect Pb^{2+} ions from aqueous media including excellent sensitive and simple detection method; with the aim of achieving the on-site, real-time and on-line determination of trace amounts of heavy metals.

There have been many sensitive and selective metal ion detection techniques used for detecting heavy metal ions, such as inductively coupled plasma atomic emission spectrometry, inductively coupled plasma mass spectrometry, atomic absorption spectrometry, atomic fluorescence spectrometry, surface enhanced Raman spectrometry, and electrochemical analysis technology (Grasso et al., 2009; Sanchez-Rodas et al., 2010; Koelmel and Amarasiriwardena, 2012; Siraj and Kitte, 2013; Massadeh et al., 2016; Lu et al., 2018). Although these techniques offer good sensitivity and selectivity toward metal ions, most of them require complicated procedures, expensive equipment, and specialized training. However, the electrochemical analysis has been referred to as an effective technique for the determination of HMIs due to its low operating cost high sensitivity, fast response, portable instrumentation, and low maintenance cost. Among the different electrochemical methods anodic stripping voltammetry (ASV) is considered the most suitable method for tracing metal analysis due to its short analysis time, high sensitivity, good selectivity, easy operation, etc. (de Souza et al., 2015).

Traditional hanging mercury drop (HMD) electrodes are considered most promising electrodes for the sensitive and selective detection of metal ions. Despite of its toxicity (HMD), electrodes have opened a door to the research community for new working electrodes achieving the friendly environment "green materials." Usually, the problem of electrochemical analysis is associated with a small surface area of working electrodes. Therefore, the aim lies in choosing such material which overcomes this drawback. In fact, the nanostructure materials have been proposed as an efficient solution to overcome this problem due to its ability to enlarge the surface area for working electrodes. Currently, carbon nanomaterials have been regarded as the ideal materials for modifying working electrodes due to their improved electrical conductivity, low cost and high readily accessible surface area (Zhang et al., 2015). Especially, from carbon nanostructures, graphene and carbon nanotubes (CNTs) have been considered as excited allotropy materials in the electrochemical detection of (HMIs) due to reasonable porous structure, environmental safety, excellent conductivity, fast electron transfer rate, and physico-chemical properties (Kong et al., 2001; Zhao et al., 2002, 2012; Novoselov and Geim, 2007; Fowler et al., 2009; Dua et al., 2010). Ceren Göde et al. studied an incorporated calixarene and reduced graphene oxide composite for simultaneous determination of Fe^{3+}, Cd^{2+}, and Pb^{2+} ions with detection limit of 2.0×10^{-11} and linear range of 1.0×10^{-10}-1.0×10^{-8} M (Göde et al., 2017). Hwang et al. employed bismuth-modified carbon nanotubes electrode for the simultaneous detection of Zn^{2+}, Cd^{2+}, Pb^{2+} ions, with linear range of 2–100 μgL^{-1}. The LOD was 1.3 μgL^{-1} for lead (Hwang et al., 2008). T. Priya et al. prepared nanocomposite of graphene oxide/K-carrageenan/L-cysteine for the simultaneous detection of Cd^{2+} and Pb^{2+}, in the range from 5–50 nM for both Cd^{2+} and Pb^{2+} with the detection limits as 0.58 and 1.08 nM, respectively (Priya et al., 2018). Wang et al. applied amination-based GO for detection lead ions in aqueous media, with the limit down to 0.1 pM; however, the negativity lies in the toxicity of Hg that used in the enrichment step of heavy metal ions (Wang et al., 2011). Nadtinan Promphet et al. developed electrochemical sensor based on graphene/polyaniline/polystyrene nanoporous fiber modified screen-printed carbon electrode for simultaneous determination of Pb^{2+} and Cd^{2+} in the presence of bismuth (Bi^{3+}). They suggested that the nanoporous fiber significantly improve the electrochemical sensitivity and graphene sheets improved the conductivity (Promphet et al., 2015). Xiaoyan Yuan et al. reported three-dimensional activated graphene networks-sulfonate-terminated polymer nanocomposite modified glassy carbon electrode (GCE) for the simultaneous determination of Cd^{2+} and Pb^{2+} in the presence of bismuth film. The result revealed linear response ranges of 1–70 μgL^{-1} for Cd^{2+} and 1–80 μgL^{-1} for Pb^{2+} with 0.1 μgL^{-1} and 0.2 μgL^{-1} LOD, respectively (Yuan et al., 2015). Jeffrey Morton et al. studied the trace of (HMIs) using CNTs functionalized covalently by cysteine. The detection limits were determined to be 1 and 15 ppb for Pb^{2+} and Cu^{2+}, respectively (Morton et al., 2009).

In the wide synthesis range of graphene, the raw material is graphene oxide (GO) which bears a lot of electroactive oxygen

containing functional groups with disorder on its basal planes and edges that decrease its conductivity. This causes significant effects on the graphene properties, resulting in lower values as compared to theoretical values (Zhao et al., 2011). CNTs also have drawbacks as its hydrophobic and surfactant dependent properties make it much complicated processing in composites. The inherent insolubility, thus greatly limits its integration in potential applications (O'connell et al., 2002; Dieckmann et al., 2003; Richard et al., 2003; Zheng et al., 2003). In fact, nanohybrid can often exhibit enhanced properties via combining the advantages of each component (Zhang and Wang, 2007; Xiao and Li, 2008; Yang et al., 2009). In order to overcome these problems, combining one-dimensional CNTs with two-dimensional graphene is worthwhile, which would provide a synergistic effect. Because GO sheets will act as best catalyst to disperse CNTs in water due to its hydrophilic property and CNTs will inhibit aggregation of GO sheets as a spacer due to its intimate reaction in sp2 hybridization of inherent material action (Zhang et al., 2010).

To the best of our knowledge there are few papers reported on the combination of CNTs and graphene for supper capacitors and biosensors, and very few papers that reported on the application of this combination for detection of Heavy Metal Ions (HMIs). One of them done by Hui Huang et al., where this hybrid was constructed with nafion film to enhance the stability for simultaneously detection of Pb^{2+} and Cd^{2+} in aqueous media in the presence of bismuth with linear range from 0.5 to 30 μgL^{-1} and low detection limit 0.2, 0.1 μgL^{-1} for Pb^{2+} and Cd^{2+}, respectively, in the case of a deposition time of 180 s (Huang et al., 2014). However, adding of bismuth and nafion to this composite hid the real effect of the nanocomposite.

In this present work, we aimed to study the effect of L-cysteine on the novel nanocomposite of three-dimensional graphene oxide/carbon nanotubes hybrid to improve its selectivity toward the detection of Pb^{2+} ions in aqueous media. The L-cysteine has been chosen for this purpose due to its role as an amino acid which contains a thiol group with electroactive mercapto groups which provide affinity to many HMIs. Moreover, L-cysteine considered as antioxidant which easily bridges the GO sheets through the rich oxygen-containing functional groups in the GO–MWNTs–L-cysteine nanocomposite.

EXPERIMENTAL

Reagents

Graphite powder (60 mesh), MWNTs (purity: >95 wt.%; O.D.: 20–30 nm; length: 0.5–2 mm) and L-cysteine were purchased from Sigma–Aldrich. Working solutions containing Zn^{2+}, Cd^{2+}, Pb^{2+}, Na^{+}, K^{+}, Mg^{2+}, Fe^{3+}, Co^{2+}, Ca^{2+}, NO_3^{2-}, and Cu^{2+} ions were prepared from respective metal salts. A 0.1 M acetate buffer (HAc-NaAc) solution was prepared by mixing appropriate amount of CH_3COOH and CH_3COONa for adjusting pH = 3, 4.5, 6, 7.5, and 9 which served as a supporting electrolyte during the analysis of metal ions. DI water was used throughout the experiments. All other chemicals used were of analytical reagent grade, and were used without further purification.

Apparatus

A CHI660C electrochemical workstation was used to perform differential pulse anodic stripping voltammetry (DPASV), Cyclic Voltammetry (CV), and Electric Impedance Spectroscopy (EIS) in a three-electrode cell made of glass beaker. All potentials presented in this work were measured with respect to the SCE. High-purity nitrogen was used to remove the oxygen molecule from the solutions prior to each experiment. Non-Contact mode Atomic Force Microscopy (AFM; Park Systems; XE-7) was performed to examine a surface morphology of synthesized composite on the Si/SiO_2 substrates. Raman spectrum was obtained with an AIRIX corp STR150 Raman, Japan (an argon ion laser $\lambda = 532$ nm). The spectroscopic study of the synthesized composite was carried out by using Fourier Attenuated Total Reflection Infrared (ATR-IR; Bruker ALPHA-T), Ultraviolet–visible (UV-vis) spectroscopy (JASCO V-750, Japan) and X-Ray Diffractometer (XRD; BRUKER D8 Advance).

Preparation of GO–MWNTs –L-cys Nanocomposite Modified Electrode

Preparation and Purification of Graphite Oxide

Graphite oxide was synthesized by the improved Hummers' method (Marcano et al., 2010). In a typical process, a mixture of 120 mL of concentrated H_2SO_4 and 13.3 mL of concentrated H_3PO_4 (9:1 volume ratio) was prepared. The mixture of these acids was poured slowly into the mixture of 1 g graphite powder and 8 g potassium permanganate (1:8) in a circular bottom beaker under constant stirring by using a magnetic stirrer. The reaction was then heated to 40°C controlled by water bath and stirred for 12 h, vigorously. Then, the mixture was added into 400 mL of DI water to stop the reaction. After that 25 mL of H_2O_2 was added to the mixture to terminate the reaction. The addition of H_2O_2 resulted in yellow color, indicating high level of oxidation. The solution was further filtered to remove metal ions from the solution resulting in yellow color slurry. The yellow colored slurry was washed with 5% HCl solution using centrifuge until SO_4^{2-} was removed completely which was tested by reagents such as barium chloride $BaCl_2$. The supernatant was decanted away and the remaining solid material was collected. Then the mixture was purified multiple times with de-ionized water using centrifuge until the pH of the supernatant became neutral. Finally, the material was dried at 50°C for 24 h and a brown black material was obtained.

Segmentation and Carboxylation of MWCNTs

The segmentation and carboxylation of MWCNTs prepared by mixing it in concentrated acids media containing of HNO_3 and H_2SO_4 with volume ratio of (1:3), respectively, for 4 h continuously, followed by filtering, rinsing with water, and drying in proper order (Jeykumari et al., 2007).

Preparation of GO–MWNTs Hybrid

Prior to use, 0.5 $mgmL^{-1}$ of MWNTs dispersed in DI water was prepared by ultrasonication for 2 h. Even so, the obtained dispersion was not stable since most of MWNTs were hydrophobic. 1.0 $mgmL^{-1}$ of GO nanosheets was obtained by exfoliation of graphite oxides by using ultrasonication bath in

DI water for 2 h (Kovtyukhova et al., 1999; Li et al., 2008). Afterwards, 10 mL of the prepared MWNTs were dispersed in 10 mL of the prepared GO hydrosol and mixed together ultrasonically for 2 h to obtain a 2:1 concentration ratio of GO: MWNTs hydrosol, respectively. The obtained mixture was further treated by using centrifugation for 30 min at 8,000 rpm to remove the unstabilized MWNTs. The obtained supernatant was consisting of the GO–MWNTs hybrid and the excess GO sheets. In order to remove the excess GO sheets, the centrifugation for 20 min at 14,000 rpm was used. Finally, the obtained sediment was washed by DI water twice and dried in vacuum oven at 50°C for 12 h to get stable nanocomposite.

Functionalization of GO–MWNTs Nanocomposites by L-cys

For functionalizing GO–MWNTs hybrid by L-cysteine (L-cys), an 1 h ultrasonication was used to disperse 10 mg of the GO–MWNTs hybrid nanocomposites into a 5 M of HCl solution containing 0.1 M L-cys to produce 4:1 weight ratio of (GO–MWNTs:L-cys). Then, the mixture was stirred constantly for 1 h at 80°C. Once again, the GO–MWNTs–L-cys nanocomposites were centrifuged for 30 min at 14,000 rpm and the solution phase was discarded. The sediment has been repeatedly washed with DI by using centrifugation until the solution phase became neutral. Finally, the obtained GO–MWNTs–L-cys nanocomposites were dried in vacuum 80°C for 12 h.

Electrode Preparation

Prior, a 10 mL suspension of GO–MWNTs–L-cys nanocomposites dispersed in DI water was sonicated for 1.5 h to produce 0.2 $mgmL^{-1}$ of GO-MWNTs–L-cys colloids. A bare glassy carbon electrode (GCE) was smoothed with 1.0, 0.3, and 0.05 mm alumina slurry, respectively. Then, it was ultrasonicated by DI water, ethanol, and ultrapure water and dried by nitrogen stream in desiccator. An aliquot of 6 μL of the colloid was cast on the GCE surface, and then the solvent was dried in vacuum at room temperature with nitrogen ambient. In this way, the GO–MWNTs–L-cys/GCE was prepared. Similarly, for comparison, the GCEs modified by GO, MWNTs, and GO–MWNTs hybrid were prepared to get GO/GCE, MWNTs/GCE, and GO–MWNTs/GCE, respectively.

Procedure for Electrochemical Testing

A three-electrode configuration was employed, consisting of GO–MWNTs–L-cys/GCE as a working electrode, Ag/AgCl containing 4 M KCl as a reference electrode and platinum wire as a counter electrode which were immersed in 50 mL of 0.1 M acetate buffer solution (pH 4.5) as a supporting electrolyte. All the solutions used for electrochemical experiments were deoxygenated by purging with pure nitrogen (99.99%) for 5 min prior to analysis. For (DPASV) test, a modified electrode (GO–MWNTs–L-cys/GCE) was immersed into the electrolyte containing metal ions under strong stirring to give a great chance of HMIs to concentrate at the modified electrode. The deposition potential was chosen as −1.2 V and the pre-accumulation time was 180 s. Prior to the next analysis, a preconditioning step with 60 s time period at 0.4 V in stirred solution was carried out to remove adsorbed residual metal ions from the surface of modified electrode. For the practical samples analysis, a 45 mL of electroplating effluent and 5 mL of 0.1 M acetate buffer (pH 4.5) were gently mixed and considered as the electrolytic solution (Huang et al., 2014).

RESULTS AND DISCUSSION

Spectroscopic Characterization of GO–MWNTs–L-cys Nanocomposites

FTIR Spectroscopy Study

ATR-IR analysis was used to investigate the functional groups and chemical bonding among the components in nanocomposite. **Figure 1** shows ATR-IR spectra of functional MWNTs, GO, GO–MWNTs hybrid, and GO–MWNTs–L-cys nanocomposite. In this spectra, the common absorption band in all spectra are observed at 2,360 and 1,615 cm^{-1} which are related to CO_2 stretch and aromatic C=C stretch groups, respectively. The aromatic group represents the skeletal vibrations of graphitic domains and CO_2 stretch assigns to atmosphere conditions. The broad absorption band in the range between 3,000 and 3,600 cm^{-1} of GO spectra represents the bending vibration and stretching of –OH groups of water molecules which has been adsorbed on GO surface through synthesis procedures. This absorption band is totally absent in the MWNTs spectra, whereas it appears again in GO–MWNTs and GO–MWNTs–L-cys spectra, with relative decrease in its magnitude, respectively, due to the non-covalent reaction in the GO–MWNTs hybrid and the reduction process by L-cysteine. The absorption bands at 1,720, 1,360 and 1,050 cm^{-1} represent the stretching and vibration of carbonyl C=O, epoxy C–O stretch and alkoxy C–O stretch groups, respectively. In the same manner with –OH group, these

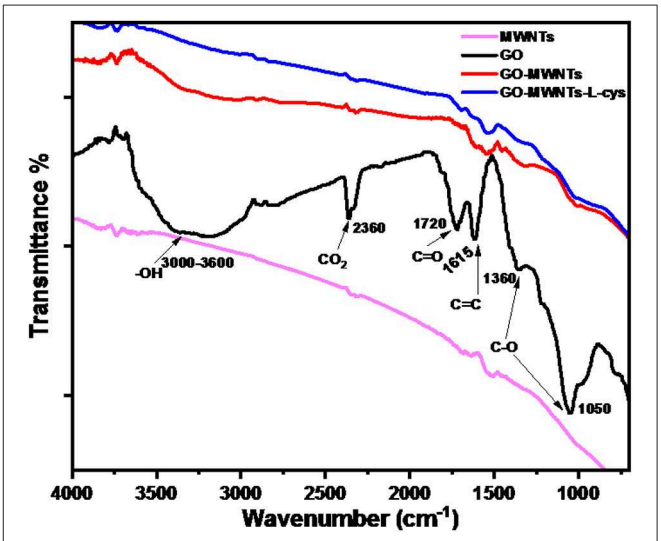

FIGURE 1 | FTIR spectra of functional MWNTs, GO, GO–MWNTs, and GO–MWNTs–L-cys from down to up, respectively.

groups decrease in the GO–MWNTs hybrid and GO–MWNTs–L-cys nanocomposite spectra due to the same reason. The FTIR results have provided additional information for the successful synthesis of GO–MWNTs–L-cys nanocomposite structure by confirming the existence of MWNTs in GO-MWNTs composite and reduction process in the presence of L-cysteine as reductant agent (Wang et al., 2007; Guo et al., 2009; Pham et al., 2011).

UV–Vis Spectroscopy Study

The UV–visible samples were prepared by dispersion of the same concentrations of GO, MWNTs, GO–MWNTs, and GO–MWNTs–L-cys in ethylene glycol with ratio of 0.2 $mgmL^{-1}$, then ultrasonicated for 1 h and then the large particles were removed by centrifugation for 10 min at 800 rpm. **Figure 2** shows the UV–visible absorption spectra of as-prepared GO, MWNTs, GO–MWNTs, and GO–MWNTs–L-cys dispersions. UV–vis spectroscopic measurements of GO dispersion display an strong absorption peak at 232 nm attributed to $\pi \rightarrow \pi^*$ transition bonding of C=C aromatic rings, shoulder peak at 302 nm arising from $n \rightarrow \pi^*$ transition of C-O bonds (Li et al., 2008; Marcano et al., 2010). The absorption peak of $\pi \rightarrow \pi^*$ transition bonding of C=C in MWNTs spectra is at 252 nm due to the easy transitions of electrons within π-conjugation network on sidewalls of the MWNTs. This peak was shifted into the moderate path at GO–MWNTs spectra confirms the formation of the hybrid between the sidewalls of the MWNTs and multiple aromatic regions of GO sheets via the π-stacking non-covalent interactions (Zhang et al., 2010; Huang et al., 2014). While this hybrid functionalized by L-cysteine, the absorption peak of $\pi \rightarrow \pi^*$ red-shifted to ~249 nm as shown in UV–vis spectra GO–MWNTs–L-cys. It implies that the aromatic structure of GO inside the GO–MWNTs–L-cys composite might be restored due to the L-cysteine (amino acid) which uses as a reductant agent for the preparation of reduced graphene oxide (Chen et al., 2011a).

The changes in the color of these dispersions are a good indicator for incorporation and reduction processes of the composite. As shown in **Figure 2** (inset), the yellow-brown and black colors of GO and MWNTs dispersion, respectively, gently mixed to make a dark brown color as in the GO–MWNTs dispersion. Finally, the color changed to black color at GO–MWNTs–L-cys dispersion due to the removal of oxygen from the GO–MWNTs when L-cysteine has been added.

Raman Spectroscopy Study

Raman spectroscopy is an efficient tool to identify ordered and disordered crystal structure of a carbon. Here, we concerned about two important bands; those of G-band and D-band within sp2 hybridization in 2D carbon material. **Figure 3** shows the characteristic peaks at 1,591 and 1,346 cm^{-1} corresponding to G- and D-band, respectively (Dong et al., 2011). The intensity ratios of characteristics peaks (I_D/I_G) are used to determine the degrees of disorder and the average size of sp2 domains. In this work, the intensity ratios of characteristics peaks (I_D/I_G) of GO, GO–MWNTs, and GO–MWNTs–L-cys films have been calculated to become (0.964, 0.980, and 0.975), respectively. The (I_D/I_G) of GO confirms the disordered in-plane sp2 due to presence of oxygen-containing functional groups, However, this disorder increase in GO–MWNTs hybrid indicated that, the MWNTs are effective as a spacer between the GO sheets which increase the average size of in-plane sp2 domains. Again, the (I_D/I_G) decreased markedly of the GO–MWNTs–L-cys nanocomposite indicated that the average size of in-plane sp2 decreased with relative less disordered, which could be explained that the partially removal of oxygen-containing functional groups results in a decrease in the average size of in-plane sp2 domain after L-cysteine treatments have been considered as a reductant agent (Tuinstra and Koenig, 1970).

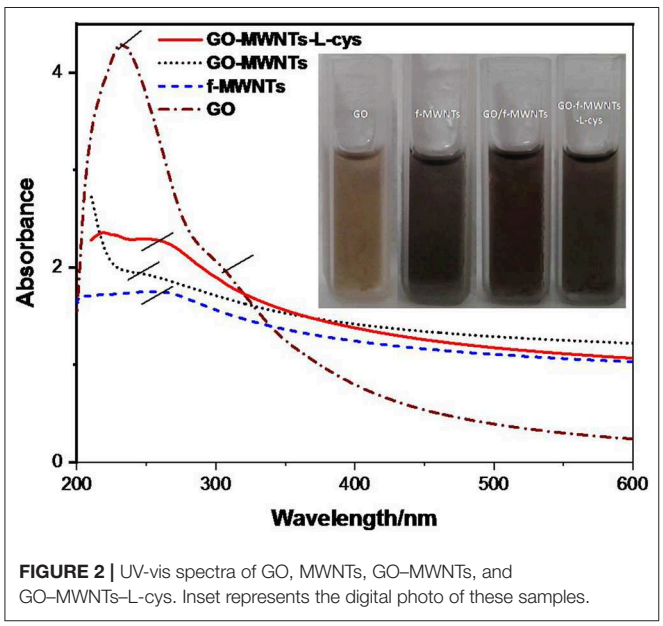

FIGURE 2 | UV-vis spectra of GO, MWNTs, GO–MWNTs, and GO–MWNTs–L-cys. Inset represents the digital photo of these samples.

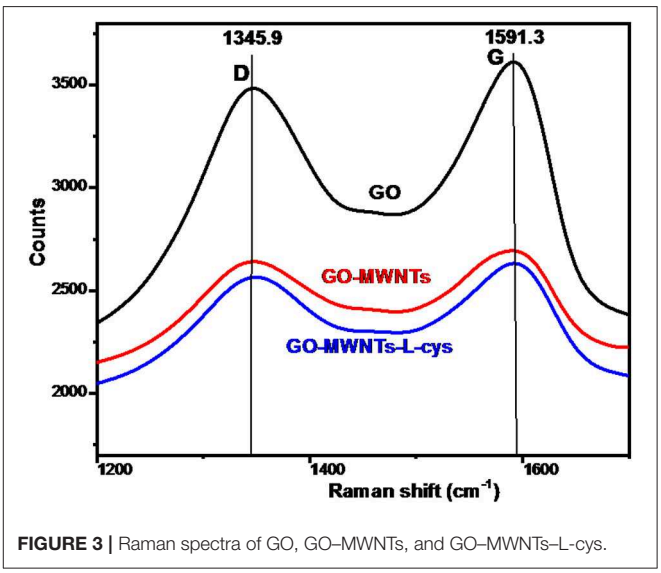

FIGURE 3 | Raman spectra of GO, GO–MWNTs, and GO–MWNTs–L-cys.

Morphological and Structural Characterizations

Morphological Study

AFM is currently one of the foremost methods to identify the morphology of carbon nanomaterial structure. **Figure 4** shows the AFM topography images of GO, functionalize MWNTs, and GO–MWNTs hybrid nanostructures. It can be seen that, the layers of GO and MWNTs films exhibit aggregations and accumulations led to a decrease in its conductivity as shown in **Figures 4A,B**, respectively. Though AFM topography image of GO–MWNTs hybrid nanostructure showed regulated and uniform distribution, as shown in **Figure 4C**, the result confirmed that the GO plays an important role in dispersing MWNTs which act as a good surfactant, in addition, the MWNTs act as a spacer between the GO sheets led to prevent the aggregations.

Structural Study

The Powder XRD patterns of Pristine Graphite (P-Graphite), Pristine MWNTs (P-MWNTs), GO, functional MWNTs, GO–MWNTs, and GO–MWNTs–L-cys nanocomposite are displayed in **Figure 5**. As observed from this figure, the XRD patterns of P-Graphite and P-MWNTs showed a character diffraction peaks at $2\theta = 26.57$ and 26.16°, respectively, indexed to the (002) crystal plane with d-spacing of 0.335 and 0.341 nm, respectively. The small increasing in the d-spacing of P-MWNTs returns to the bending effect of the graphite sheets. However, in XRD pattern of GO, this diffraction peak of Graphite material has been shifted

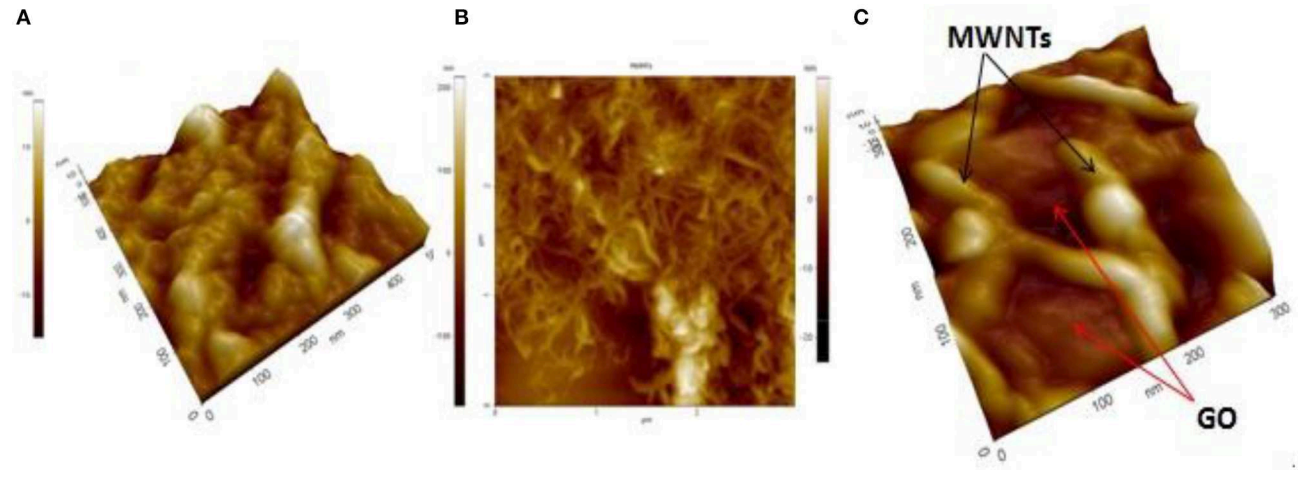

FIGURE 4 | Non-contact mode AFM images of: **(A)** exfoliated GO, **(B)** functionalize MWNTs, and **(C)** GO–MWNTs hybrid deposit by drop casting on Si/SiO_2 substrates.

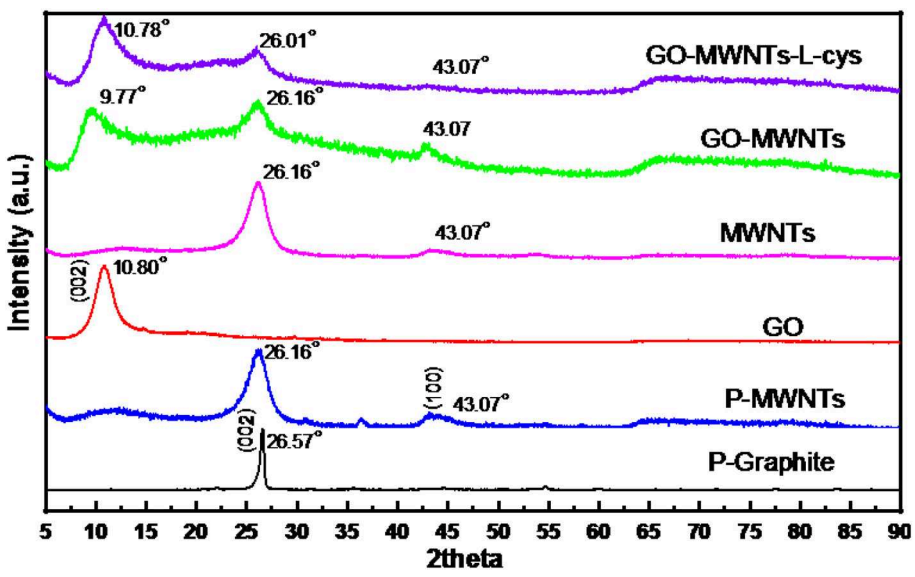

FIGURE 5 | Powder XRD patterns of P-Graphite, P-MWNTs, functionalized MWNTs, GO, GO–MWNTs, and GO–MWNTs–L-cys (from down to up), respectively.

to $2\theta = 10.80^{\circ}$, with extension in d-spacing of 0.819 nm due to the insertion of various oxygen-containing functional groups in the graphite structure. After Functionalization of MWNTs by acids treatments for cleaning and insolubility proposes, its XRD patterns show diffraction peak same that in the P-MWNTs pattern with a little decreasing in a grain size by considering (Scherrer equation) indicating that, the segmentation and carboxylation processes have taken place. The XRD patterns of GO–MWNTs hybrid showed a conservation of its individual diffraction peaks at $2\theta = 9.77$ and 26.16° for GO and MWNTs, respectively. A little extension in d-spacing of 0.905 nm of GO after mixing with MWNTs indicating that, the non-covalent interaction between functionalized MWNTs and GO sheets was affected through interlayer of the basal plane of GO sheets. The XRD patterns of GO–MWNTs–L-cys nanocomposite showed character diffraction peaks at $2\theta = 10.78$ and 26.01°, with d-spacing of 0.820 and 0.342 nm for GO and MWNTs, respectively. However, there were a little compression and extension in d-spacing of GO and MWNTS, respectively, in the GO–MWNTs–L-cys nanocomposite comparing with that in GO–MWNTs. This compression in d-spacing after adding L-cysteine to the composite is due to the effect of L-cysteine as reductant agent which removed the oxygen-containing functional groups partially from the edges of GO sheets. The extension in the d-spacing of MWNTs is also due to the strong interaction between thiol groups inside the L-cysteine and outer side of MWNTs which might lead to a little extension between the outer and inner sides of MWNTs.

Electrochemical Characterization of GO–MWNTs–L-cys Nanocomposite Modified Electrode

Electrochemical Reduction of GO–MWNTs–L-cys Nanocomposite

As prepared, GO–MWNTs–L-cys/GCE was reduced by carrying out repeated potential cycling within potential range between 0 and −1.7 V in the deoxygenized acetate (pH 4.5) buffer solution to produce the ErGO–MWNTs–L-cys (Jeykumari et al., 2007). The cyclic voltammetry (CV) of ErGO–MWNTs–L-cys showed a large reduction peak in the first potential scan at −1.2 V, as shown in **Figure 6A**. Moreover, for further subsegment cycles the reduction peak has been shifted toward more negative potentials indicating that the most of oxygen functional groups on the GO surface were removed during the first cycle. For comparison, a similar experiment has been performed by using a GO/GCE as shown in **Figure 6B**. However, the CV of GO/GCE showed a larger reduction peak in the first potential scan at −1.3 V and with less relatively reduction potential peaks difference comparing with that in ErGO–MWNTs–L-cys/GCE, which indicated that the Electrochemical reduction process of GO sheets needs relatively longer time compared with ErGO–MWNTs–L-cys nanocomposite, which almost achieved in the first cycle. A little remaining strong contact of oxygen-containing functional groups on the edge of graphene basal plan was reduced at drastically more negative potential. The results could be explained by saying that the CNTs don't only act as spacer between GO sheets to inhibit aggregation, but it also acts as conducting wires passed throw GO sheets which facilitate the reduction process of GO sheets.

Charge-Transfer Behavior of ErGO–MWNTs–L-cys Nanocomposite

The behavior of charge-transfer rate at the electrode/solution interface was explained by CV and Electric Impedance Spectroscopy EIS (Tang et al., 2009). In this work we compared the charge-transfer behavior of the bare GCE, GO/GCE, MWCNTs/GCE, GO–MWNTs/GCE, GO–MWNTs–L-cys/GCE, and ErGO-MWNTs-cys/GCE in 0.1 M KCl solution using a $[Fe(CN)_6]^{3-/4-}$ couple as a redox probe system. Cyclic Voltammograms (CVs) of modified and bare GCE are shown in **Figure 7A**. Initially, the CV of the bare GCE showed a peak potential difference (ΔE_P) 90 mV with ratio of 1:1 between anodic and cathodic peak currents. It can be considered as

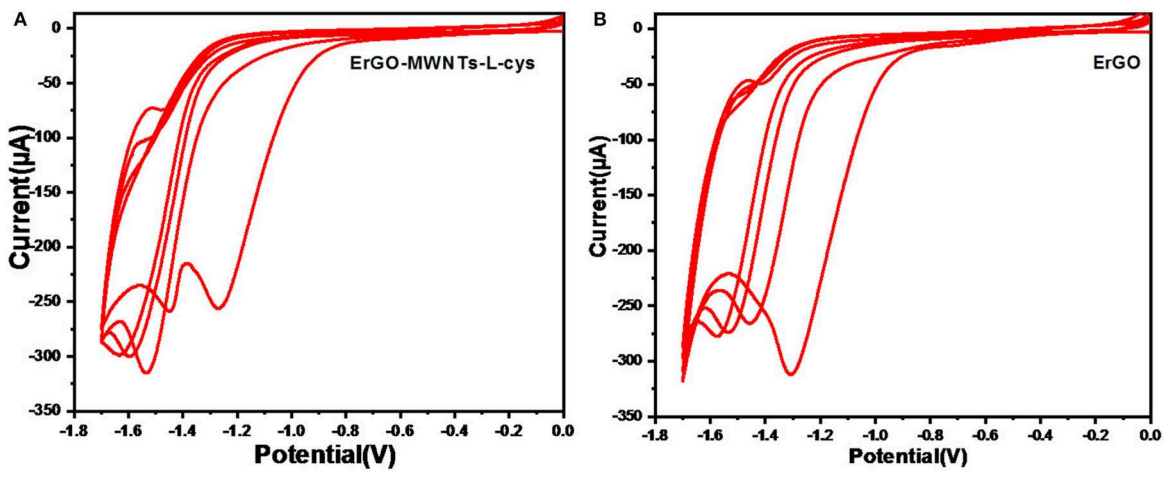

FIGURE 6 | Cyclic Voltammograms (CVs) with 0.05 Vs^{-1} scan rate for the electrochemical reduction of GCE modified with: **(A)** GO–MWNTs–L-cys nanocomposite and **(B)** GO sheets; in 0.1 M acetate buffer solution (pH 4.5) saturated with nitrogen gas. The range is between 0 and −1.7 V.

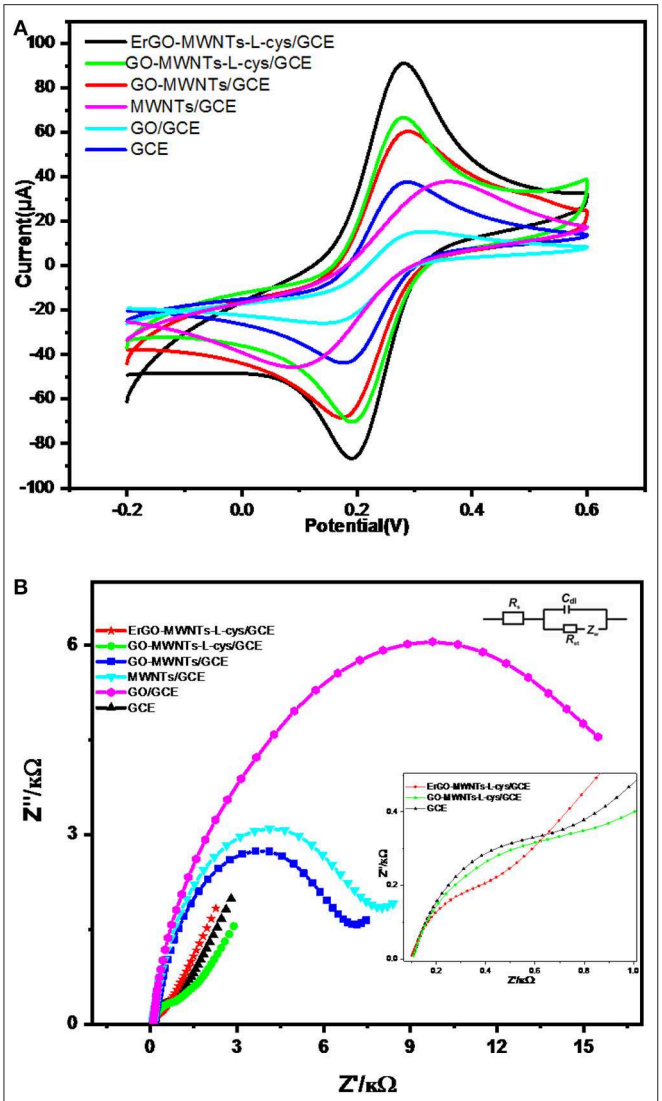

FIGURE 7 | (A) CV and **(B)** EIS characterizations of bare GCE, GO/GCE, MWCNTs/GCE, GO–MWNTs/GCE, GO–MWNTs–L-cys/GCE, and ErGO-MWNTs-cys/GCE in 0.1 M KCl solution containing 5 mM $[Fe(CN)_6]^{3-/4-}$ couple as a redox probe system. The parameters of CV and EIS are 0.5 Vs^{-1} scan rate repeated in the range between −0.2 and 0.6 V and frequency range from 0.1 to 105 Hz while applying 0.2 V AC amplitude, respectively. Inset: magnification plot of higher frequencies and equivalent electrical circuit used for fitting the impedance spectra.

a quasi-reversible redox process. The CV of GO showed the decrease peak currents to a very low value because of the bad conductivity of GO. However, increase in the peak currents was observed with MWNTs/GCE due to the good conductivity of CNTs, but it does not exceed the peak currents of the bare GCE because of its aggregation nature. It also shows a broad redox peaks potential difference due to the binding of the analytes with its curvature surface led to a slow charge-transfer rate at the electrode/solution interface. The CV of GO–MWNTs/GCE showed quasi-reversible redox processes and fast charge-transfer rate which indicated that the enhancements took place when both of GO and MWNTs were mixed. Moreover, the GO–MWNTs hybrid showed the peak redox currents larger than that of GO/GCE and MWNTs/GCE CVs which indicated that the individually disadvantages treated led to large surface area. The CV of GO–MWNTs–L-cys/GCE showed little enhancements in terms of the charge-transfer rate and peak redox currents due to the removal of oxygen- containing functional groups from GO–MWNTs hybrid when L-cysteine was added. Finally, the CV of ErGO–MWNTs–L-cys/GCE showed extremely large redox peak currents and lower peak potential difference (ΔE_P) as compared to others due to electrochemical reduction of the nanocomposite which was synergized. The reduction processes enhances the conductivity and surface area of the hybrid. These results showed excellent agreements with other characterizations.

EIS was used to monitor the electron transfer properties of these electrodes. The diameter of the semicircle in the EIS Nyquist plot represents the electron-transfer resistance R_{ct} of the electrode/electrolyte (Chen et al., 2011b). **Figure 7B** shows the Nyquist plot obtained for the bare GCE, GO/GCE, MWCNTs/GCE, GO–MWNTs/GCE, GO–MWNTs–L-cys/GCE, and ErGO–MWNTs–L-cys/GCE at AC amplitude 0.2 V within the frequency range from 0.1 to 10^5 Hz. For fitting of impedance spectra data, A Randles circuit model $[Rs+C_{dl}/(R_{ct}+Z_W)]$ was used. As shown in **Figure 7B**, the R_{ct} values of the bare GCE, GO/GCE, MWCNTs/GCE, GO–MWNTs/GCE, GO–MWNTs–L-cys/GCE, and ErGO-MWNTs-cys/GCE are 0.77, 9.95, 7.47, 6.90, 1.46, and 0.41 kΩ, respectively. These results exhibited totally agreement with the CV characterizations in terms of charge transfer rate.

Optimization of the Experimental Conditions

The influence of pH of acetate buffer solutions on the stripping signal was studied of the pH range from 3 to 9 by DPASV technique as shown in **Figure 8A**. It showed a significant impact of pH on current peaks and the maximum value of stripping signal was observed at pH = 4.5.

The range of accumulation time was from 30 to 220 s which showed direct proportional effect with the current peaks as shown in **Figure 8B**. However, its slope started decreasing beyond 180 s, therefore, 180 s was chosen as accumulation time due to efficiency considerations.

The amount of oxygen-containing functional groups on the reduced graphene oxide sheets play important roles on its band gab, leading to controlling its properties like conductivity, insolubility, stability, and its ability of HMIs adsorption (Raj and John, 2013; Promphet et al., 2015).

The effect of electrochemical reduction degrees of GO–MWNTs–L-cys nanocomposites on the stripping signal were achieved by two steps. First step, four identical GCEs modified by GO–MWNTs–L-cys nanocomposite were electrochemically reduced by applying CV technique with 0, 3, 4, and 6 number of cycles in acetate buffer solution bubbled by pure NO_2, respectively. Second step, the DPASVs of Four electrodes were performed in acetate buffer solution containing 40 μgL^{-1} of Pb^{2+} ions under the optimized conditions. The **Figure 8C**

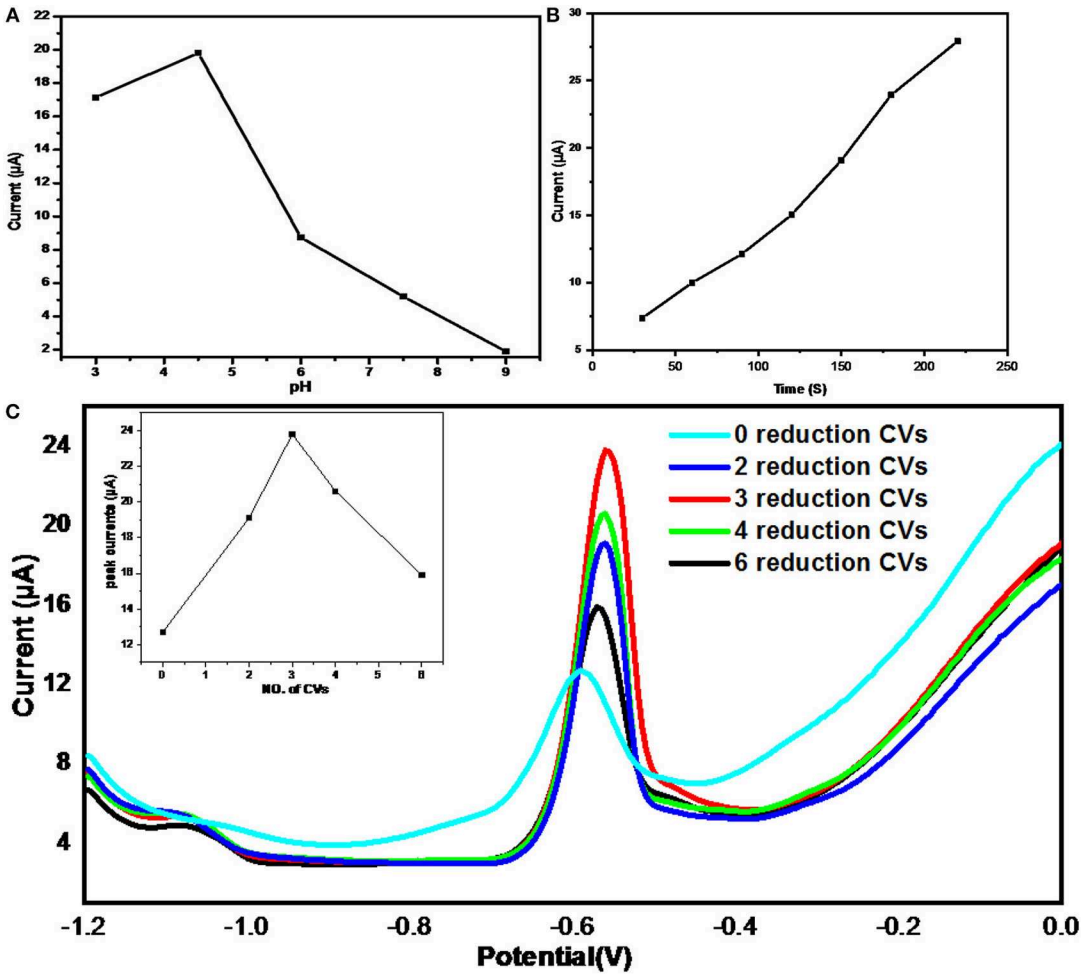

FIGURE 8 | The effects of **(A)** solution pH, **(B)** accumulation time, and **(C)** Electrochemical reduction degrees; (inset shows the peak currents vs. No. of CVs); on the stripping currents of Pb^{2+} ions from ErGO–MWNTs–L-cys/GCEs in 0.1 M HAc-NaAc buffer solution containing 40 μgL^{-1} of Pb^{2+} saturated with nitrogen gas under optimal conditions.

showed the stripping signals of Pb^{2+} ions from ErGO–MWNTs–L-cys/GCEs with different reduction degrees of (0, 3, 4, and 6 CVs). As observed in the **Figure 7C**, there were different stripping signal peak currents, it can be ordered from highest to lowest at ErGO–MWNTs–L-cys/GCEs have 3, 4, 2, 6, and 0 reduction CVs, respectively. Despite of the ErGO–MWNTs–L-cys/GCEs with 3 reduction CVs exhibited highest stripping signal, the ErGO–MWNTs–L-cys/GCEs with 4 reduction CVs has been selected for optimization conditions due to its short recovery time. A Reduction potential for Pb^{2+} ions has been directly selected as −1.2 V (Huang et al., 2014).

Electrochemical Performance of Modified Electrodes Toward Pb^{2+} Ions

Here we have studied the stripping signal responses toward Pb^{2+} ions at the bare GCE (dot line), GO/GCE (red line), GO–MWNTs/GCE (green line), GO–MWNTs–L-cys/GCE (blue line), and ErGO–MWNTs–L-cys/GCE (brown line) in acetate buffer solution containing 50 μgL^{-1} Pb^{2+} ions by DPASV technique under optimal conditions, as shown in **Figure 9**. It can be seen that the voltammograms of ErGO–MWNTs–L-cys/GCE exhibited anodic peak current of Pb^{2+} ions higher than the one measured on the GO–MWNTs–L-cys/GCE (blue line), GO–MWNTs/GCE (green line), GO/GCE (red line) and bare GCE (dot line) by 1.4, 1.9, 3.2, and 2.7-fold, respectively, with well-defined peak shapes centered at −0.555 V. This data could be explained in similar manner of CV for the $[Fe(CN)_6]^{3-/4-}$ standard redox couple shown in **Figure 7A**. This data confirm that the large surface area and excellent electrochemical conductivity of the ErGO–MWNTs–L-cys nanocomposite modified GCE lead to enhanced electrochemical sensitivity.

Sensing Study Toward Pb^{2+} ions at ErGO–MWNTs–L-cys/GCE

The sensing study of the ErGO–MWNTs–L-cys/GCE for determination of Pb^{2+} ions under optimal conditions has been evaluated. **Figure 10**, showed the voltammograms of DPASVs for Pb^{2+} ions with various concentrations in acetate buffer solutions. As shown in **Figure 10** (inset) It can be seen that

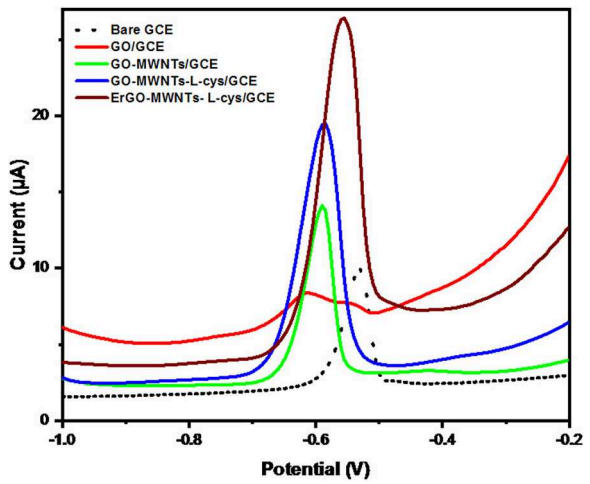

FIGURE 9 | The DPASVs for 50 μgL^{-1} Pb^{2+} at the bare GCE (dot line), GO/GCE (red line), GO–MWNTs/GCE (green line), GO–MWNTs–L-cys/GCE (blue line), and ErGO–MWNTs–L-cys/GCE (brown line) under optimal conditions.

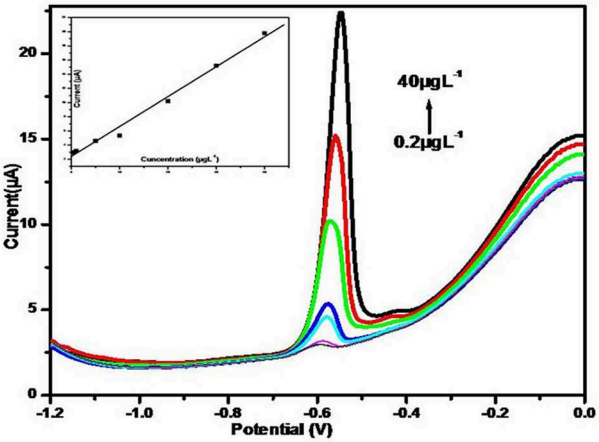

FIGURE 10 | The DPASVs for various concentrations (0.2, 0.5, 1, 5, 10, 20, 30, and 40 μgL^{-1} from bottom to top) of Pb^{2+} ions on the ErGO–MWNTs–L-cys/GCE. Inset shows the calibration curve of the Pb^{2+} ions. Supporting electrolyte: 0.1 M acetate buffer (pH = 4.5) under optimal conditions.

the anodic peak currents are direct proportional to the Pb^{2+} ions concentrations in the range from 40 μgL^{-1} to 0.2 μgL^{-1} represented in the regression equation of $I_p = 0.422\,C + 2.396$ (I_P: peak currents/μA, C: concentration/μgL^{-1}) with the correlation coefficient of $R = 0.990$. The limit of detection (LOD) was calculated to be 0.1 μgL^{-1} by using [LOD = 3 sc/x] formula; where s is the standard deviation of the peak currents of the sample (10 times), c is the concentration of the sample here (0.2 μgL^{-1}) was taken and x is the average value of the sample; which is lower than (10 μgL^{-1}) that has recommended by World Health Organization for Pb^{2+} ions in drinking water (WHO, 2011).

In fact, the nafion enhances the stability of G/MWNTs hybrid as mentioned in literature (Huang et al., 2014), but it influences the sensitivity of composite due to diffusion limitations imposed by Nafion (Gouveia-Caridade et al., 2006). In this work, we avoided the effect of nafion film by choosing L-cysteine as computable legend and reductant agent leading to improved selectivity, stability, and electrochemical conductivity.

Reproducibility, Stability, and Interference Study of the ErGO–MWNTs–L-cys Electrode

The study of the reproducibility and stability of ErGO–MWNTs–L-cys/GCEs was carried out in acetate buffer containing 40 μgL^{-1} of Pb^{2+} ions under optimized conditions. To investigate the reproducibility, four ErGO–MWNTs–L-cys nanocomposite modified GCEs were prepared with identical procedures. The relative standard deviations (RSD) for these electrodes were calculated to be 2.15% as shown in **Figure 11A**. Moreover, the modified electrode was kept for 17 days at room temperature for stability study and there was no significant change observed in the stripping signals when they were compared with fresh electrode. These results showed that the ErGO–MWNTs–L-cys nanocomposites modified electrodes have excellent life time with good stability which could be explained by the affect of L-cysteine and Electrochemical reduction which removed the weak oxygen-containing functional groups from the basal plane and only the strong functional groups and amino groups on its edges remained.

The interference effect on the ErGO–MWNTs-L-cys/GCE toward Pb^{2+} ions was studied by testing the DPASV in presence of 50 μgL^{-1} Pb^{2+} acetate buffer solution containing other ions. They were divided into two groups. In the first group, the DPASVs have been performed in acetate buffer solution containing 50 μgL^{-1} of (Pb^{2+}, Cd^{2+}, Na^{+}, K^{+}, Mg^{2+}, Fe^{3+}, Co^{2+}, Ca^{2+}, and NO_3^{2-}) ions under optimized conditions as shown in **Figure 11B**. Similarly, the second step was performed in presence of (Pb^{2+}, Cd^{2+}, Zn^{2+}, and Cu^{2+}) ions as shown in **Figure 11C**. However, it can be seen that, there were no significant effect on the stripping signal of Pb^{2+} ions from most interference ions except that of Cd^{2+}, Zn^{2+}, and Cu^{2+} ions which showed considerably stripping signals due to the hexagonal activated surface of GO–MWNTs hybrid and the affinity of L-cysteine toward HMIs. The results showed that a 5.8-fold mass ratio of Cd^{2+}, 2.5-fold mass ratio of Zn^{2+}, and 3.2-fold mass ratio of Cu^{2+} were found as the tolerance ratios for the detection of Pb^{2+} ions at 50 μgL^{-1}. However, this influence for real sample containing high levels of Cd^{2+}, Zn^{2+}, and Cu^{2+} can be neglected by diluting to a level that is less than their tolerance (Hynek et al., 2012; Lezi et al., 2012).

CONCLUSIONS

The electrochemical selectivity toward Pb^{2+} ions at three-dimensional of ErGO–MWNTs hybrid based electrode was successfully enhanced by adding L-cysteine. The large surface area, electrical conductivity, and rich amino-groups of the

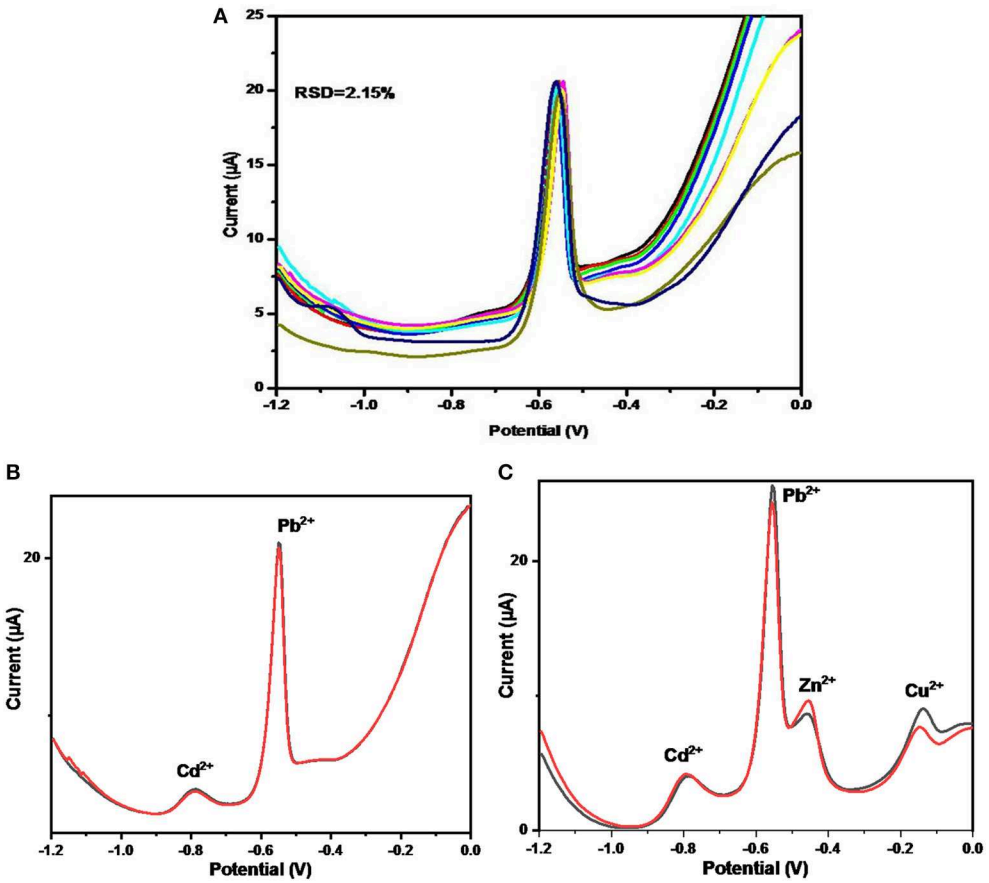

FIGURE 11 | The DPASV stripping signals on ErGO–MWNTs–L-cys modified GCEs for: **(A)** 9 times measurements with four identical modified GCEs toward 40 μgL^{-1} of Pb^{2+} ions **(B)**, 50 μgL^{-1} of (Pb^{2+}, Cd^{2+}, Na^{+}, K^{+}, Mg^{2+}, Fe^{3+}, Co^{2+}, Ca^{2+}, & NO3^{2-}) ions, and **(C)** 50 μgL^{-1} of (Pb^{2+}, Cd^{2+}, Na^{+}, K^{+}, Mg^{2+}, Fe^{3+}, Co^{2+}, Ca^{2+}, & NO_3^{2-}) ions in acetate buffer solution under optimal conditions.

ErGO–MWNTs–L-cys significantly improved the sensitivity and selectivity in the determination of Pb^{2+} ions. By modifying GCE with the ErGO–MWNTs–L-cys nanocomposite along with DPASV, a linear range of 0.2–40 μgL^{-1} for Pb^{2+} ions was obtained. The limit of detection (LOD) was calculated to be 0.1 μgL^{-1}. The results of stability and reproducibility study do not change appreciably for several days, so it may be used for the stable sensors fabrication.

DATA AVAILABILITY STATEMENT

The datasets generated for this study are available on request to the corresponding author.

AUTHOR'S NOTE

The improvement of large surface area by nanocomposite of carbon nanomaterial has avoided the distinguish problem associated with electrochemical sensors particularly in a small surface area of working electrode. Herein, we have chosen a particular reductant agent for reduction of GO in rGO/MWNTs hybrid that is L-cysteine which can employ also for detection of lead ions owing its structure with rich of amino and thiol groups. Therefore, we achieved main impact factors for construction of electrochemical sensor in terms of its sensitivity and selectivity.

AUTHOR CONTRIBUTIONS

TA-G performed the experimental work, analyzed the characterized part, and justified all the results. GB, PS, NI, MM, and SS guided for instrumentation technique. MD and NM checked the article grammar. MS was the guide and responsible of this work.

ACKNOWLEDGMENTS

The authors extend their sincere thanks to DST—SERB, New Delhi (Project No. EEQ/2017/000645), UGC—DAE CSR (RRCAT), Indore (Project No. CSR-IC-BL66/CRS- 183/2016-17/847), Inter University Accelerator Center (IUAC), New Delhi, India (UFR no. 62320), Rashtria Uchachatar Shiksha Abhiyan (RUSA), Government of Maharashtra, UGC-SAP Programme (F.530/16/DRS-I/2016(SAP-II) Dt.16-04-2016) and DST-FIST (Project No. No. SR/FST/PSI-210/2016(C) dtd. 16/12/2016) for providing financial support.

REFERENCES

Adarakatti, P. S., Foster, C. W., Banks, C. E., Arun Kumar, N. S., and Malingappa, P. (2017). Calixarene bulk modified screen-printed electrodes (SPCCEs) as a one-shot disposable sensor for the simultaneous detection of lead (II), copper (II) and mercury (II) ions: application to environmental samples. *Sens. Actuators A Phys.* 267, 517–525. doi: 10.1016/j.sna.2017.10.059

Chen, D., Li, L., and Guo, L. (2011a). An environment-friendly preparation of reduced graphene oxide nanosheets via amino acid. *Nanotechnology* 22:325601. doi: 10.1088/0957-4484/22/32/325601

Chen, W., Rakhi, R., Hu, L., Xie, X., Cui, Y., and Alshareef, H. N. (2011b). High-performance nanostructured supercapacitors on a sponge. *Nano Lett.* 11, 5165–5172. doi: 10.1021/nl2023433

de Souza, A. P. R., Foster, C. W., Kolliopoulos, A. V., Bertotti, M., and Banks, C. E. (2015). Screen-printed back-to-back electroanalytical sensors: heavy metal ion sensing. *Analyst* 140, 4130–4136. doi: 10.1039/C5AN00381D

Deshmukh, M. A., Celiesiute, R., Ramanaviciene, A., Shirsat, M. D., and Ramanavicius, A. (2018a). EDTA_PANI/SWCNTs nanocomposite modified electrode for electrochemical determination of copper (II), lead (II) and mercury (II) ions. *Electrochim. Acta* 259, 930–938. doi: 10.1016/j.electacta.2017.10.131

Deshmukh, M. A., Gicevicius, M., Ramanaviciene, A., Shirsat, M. D., Viter, R., and Ramanavicius, A. (2017b). Hybrid electrochemical/electrochromic Cu (II) ion sensor prototype based on PANI/ITO-electrode. *Sens. Actuators B Chem.* 248, 527–535. doi: 10.1016/j.snb.2017.03.167

Deshmukh, M. A., Patil, H., Shirsat, M., and Ramanavicius, A. (2017a). "Electrochemical detection of Hg (II) ions using EDTA-PANI/SWNTs nanocomposite modified SS electrode," in *AIP Conference Proceedings* (Aurangabad: AIP Publishing), 050084.

Deshmukh, M. A., Patil, H. K., Bodkhe, G. A., Yasuzawa, M., Koinkar, P., Ramanaviciene, A., et al. (2018b). EDTA-modified PANI/SWNTs nanocomposite for differential pulse voltammetry based determination of Cu (II) ions. *Sens. Actuators B Chem.* 260, 331–338. doi: 10.1016/j.snb.2017.12.160

Deshmukh, M. A., Shirsat, M. D., Ramanaviciene, A., and Ramanavicius, A. (2018c). Composites based on conducting polymers and carbon nanomaterials for heavy metal ion sensing. *Crit. Rev. Anal. Chem.* 48, 293–304. doi: 10.1080/10408347.2017.1422966

Dieckmann, G. R., Dalton, A. B., Johnson, P. A., Razal, J., Chen, J., Giordano, G. M., et al. (2003). Controlled assembly of carbon nanotubes by designed amphiphilic peptide helices. *J. Am. Chem. Soc.* 125, 1770–1777. doi: 10.1021/ja029084x

Dong, X., Wang, P., Fang, W., Su, C.-Y., Chen, Y.-H., Li, L.-J., et al. (2011). Growth of large-sized graphene thin-films by liquid precursor-based chemical vapor deposition under atmospheric pressure. *Carbon* 49, 3672–3678. doi: 10.1016/j.carbon.2011.04.069

Dua, V., Surwade, S. P., Ammu, S., Agnihotra, S. R., Jain, S., Roberts, K. E., et al. (2010). All-organic vapor sensor using inkjet-printed reduced graphene oxide. *Angew. Chem. Int. Ed. Engl.* 49, 2154–2157. doi: 10.1002/anie.200905089

Fowler, J., Allen, M., Tung, V., Yang, Y., Kaner, R., and Weiller, B. (2009). Practical chemical sensors from chemically derived graphene. *ACS Nano.* 3, 301–306. doi: 10.1021/nn800593m

Göde, C., Yola, M. L., Yilmaz, A., Atar, N., and Wang, S. (2017). A novel electrochemical sensor based on calixarene functionalized reduced graphene oxide: application to simultaneous determination of Fe (III), Cd (II) and Pb (II) ions. *J. Colloid Interface Sci.* 508, 525–531. doi: 10.1016/j.jcis.2017.08.086

Gouveia-Caridade, C., Pauliukaite, R., and Brett, C. M. (2006). Influence of nafion coatings and surfactant on the stripping voltammetry of heavy metals at bismuth-film modified carbon film electrodes. *Electroanalysis* 18, 854–861. doi: 10.1002/elan.200603482

Grasso, G., D'Urso, L., Messina, E., Cataldo, F., Puglisi, O., Spoto, G., et al. (2009). A mass spectrometry and surface enhanced raman spectroscopy study of the interaction between linear carbon chains and noble metals. *Carbon* 47, 2611–2619. doi: 10.1016/j.carbon.2009.05.013

Guo, H.-L., Wang, X.-F., Qian, Q.-Y., Wang, F.-B., and Xia, X.-H. (2009). A green approach to the synthesis of graphene nanosheets. *ACS Nano* 3, 2653–2659. doi: 10.1021/nn900227d

Huang, H., Chen, T., Liu, X., and Ma, H. (2014). Ultrasensitive and simultaneous detection of heavy metal ions based on three-dimensional graphene-carbon nanotubes hybrid electrode materials. *Anal. Chim. Acta* 852, 45–54. doi: 10.1016/j.aca.2014.09.010

Hwang, G. H., Han, W. K., Park, J. S., and Kang, S. G. (2008). Determination of trace metals by anodic stripping voltammetry using a bismuth-modified carbon nanotube electrode. *Talanta* 76, 301–308. doi: 10.1016/j.talanta.2008.02.039

Hynek, D., Krejcova, L., Sochor, J., Cernei, N., Kynicky, J., Adam, V., et al. (2012). Study of interactions between cysteine and cadmium (II) ions using automatic pipetting system off-line coupled with electrochemical analyser. *Int. J. Electrochem. Sci.* 7, 1802–1819.

Jeykumari, D. S., Ramaprabhu, S., and Narayanan, S. S. (2007). A thionine functionalized multiwalled carbon nanotube modified electrode for the determination of hydrogen peroxide. *Carbon* 45, 1340–1353. doi: 10.1016/j.carbon.2007.01.006

Koelmel, J., and Amarasiriwardena, D. (2012). Imaging of metal bioaccumulation in Hay-scented fern (*Dennstaedtia punctilobula*) rhizomes growing on contaminated soils by laser ablation ICP-MS. *Environ. Pollut.* 168, 62–70. doi: 10.1016/j.envpol.2012.03.035

Kong, J., Chapline, M. G., and Dai, H. (2001). Functionalized carbon nanotubes for molecular hydrogen sensors. *Adv. Mater.* 13, 1384–1386. doi: 10.1002/1521-4095(200109)13:18<1384::AID-ADMA1384>3.0.CO;2-8

Kovtyukhova, N. I., Ollivier, P. J., Martin, B. R., Mallouk, T. E., Chizhik, S. A., Buzaneva, E. V., et al. (1999). Layer-by-layer assembly of ultrathin composite films from micron-sized graphite oxide sheets and polycations. *Chem. Mater.* 11, 771–778. doi: 10.1021/cm981085u

Lee, G.-J., Lee, H.-M., and Rhee, C.-K. (2007). Bismuth nano-powder electrode for trace analysis of heavy metals using anodic stripping voltammetry. *Electrochem. Commun.* 9, 2514–2518. doi: 10.1016/j.elecom.2007.07.030

Lezi, N., Economou, A., Dimovasilis, P. A., Trikalitis, P. N., and Prodromidis, M. I. (2012). Disposable screen-printed sensors modified with bismuth precursor compounds for the rapid voltammetric screening of trace Pb (II) and Cd (II). *Anal. Chim. Acta* 728, 1–8. doi: 10.1016/j.aca.2012.03.036

Li, D., Müller, M. B., Gilje, S., Kaner, R. B., and Wallace, G. G. (2008). Processable aqueous dispersions of graphene nanosheets. *Nat. Nanotechnol.* 3, 101–105. doi: 10.1038/nnano.2007.451

Liu, J., Zhang, X.-H., Tran, H., Wang, D.-Q., and Zhu, Y.-N. (2011). Heavy metal contamination and risk assessment in water, paddy soil, and rice around an electroplating plant. *Environ. Sci. Pollut. Res. Int.* 18, 1623–1632. doi: 10.1007/s11356-011-0523-3

Lu, Y., Liang, X., Niyungeko, C., Zhou, J., Xu, J., and Tian, G. (2018). A review of the identification and detection of heavy metal ions in the environment by voltammetry. *Talanta* 178, 324–338. doi: 10.1016/j.talanta.2017.08.033

Marcano, D. C., Kosynkin, D. V., Berlin, J. M., Sinitskii, A., Sun, Z., Slesarev, A., et al. (2010). Improved synthesis of graphene oxide. *ACS Nano* 4, 4806–4814. doi: 10.1021/nn1006368

Massadeh, A. M., Alomary, A. A., Mir, S., Momani, F. A., Haddad, H. I., and Hadad, Y. A. (2016). Analysis of Zn, Cd, As, Cu, Pb, and Fe in snails as bioindicators and soil samples near traffic road by ICP-OES. *Environ. Sci. Pollut. Res.* 23, 13424–13431. doi: 10.1007/s11356-016-6499-2

Morton, J., Havens, N., Mugweru, A., and Wanekaya, A. K. (2009). Detection of trace heavy metal ions using carbon nanotube-modified electrodes. *Electroanalysis* 21, 1597–1603. doi: 10.1002/elan.200904588

Novoselov, K. S., and Geim, A. (2007). The rise of graphene. *Nat. Mater.* 6, 183–191. doi: 10.1038/nmat1849

O'connell, M. J., Bachilo, S. M., Huffman, C. B., Moore, V. C., Strano, M. S., Haroz, E. H., et al. (2002). Band gap fluorescence from individual single-walled carbon nanotubes. *Science* 297, 593–596. doi: 10.1126/science.1072631

Pham, V. H., Cuong, T. V., Hur, S. H., Oh, E., Kim, E. J., Shin, E. W., et al. (2011). Chemical functionalization of graphene sheets by solvothermal reduction of a graphene oxide suspension in N-methyl-2-pyrrolidone. *J. Mater. Chem.* 21, 3371–3377. doi: 10.1039/C0JM02790A

Priya, T., Dhanalakshmi, N., Thennarasu, S., and Thinakaran, N. (2018). A novel voltammetric sensor for the simultaneous detection of Cd2+ and Pb2+ using graphene oxide/κ-carrageenan/l-cysteine nanocomposite. *Carbohydr. Polym.* 182, 199–206. doi: 10.1016/j.carbpol.2017.11.017

Promphet, N., Rattanarat, P., Rangkupan, R., Chailapakul, O., and Rodthongkum, N. (2015). An electrochemical sensor based on

graphene/polyaniline/polystyrene nanoporous fibers modified electrode for simultaneous determination of lead and cadmium. *Sens. Actuators B Chem.* 207, 526–534. doi: 10.1016/j.snb.2014.10.126

Quang, D. T., and Kim, J. S. (2010). Fluoro-and chromogenic chemodosimeters for heavy metal ion detection in solution and biospecimens. *Chem. Rev.* 110, 6280–6301. doi: 10.1021/cr100154p

Raj, M. A., and John, S. A. (2013). Fabrication of electrochemically reduced graphene oxide films on glassy carbon electrode by self-assembly method and their electrocatalytic application. *J. Phys. Chem. C* 117, 4326–4335. doi: 10.1021/jp400066z

Richard, C., Balavoine, F., Schultz, P., Ebbesen, T. W., and Mioskowski, C. (2003). Supramolecular self-assembly of lipid derivatives on carbon nanotubes. *Science* 300, 775–778. doi: 10.1126/science.1080848

Sanchez-Rodas, D., Corns, W., Chen, B., and Stockwell, P. (2010). Atomic fluorescence spectrometry: a suitable detection technique in speciation studies for arsenic, selenium, antimony and mercury. *J. Anal. At. Spectrom.* 25, 933–946. doi: 10.1039/b917755h

Siraj, K., and Kitte, S. A. (2013). Analysis of copper, zinc and lead using atomic absorption spectrophotometer in ground water of Jimma town of Southwestern Ethiopia. *Int. J. Anal. Chem.* 4, 201–204. doi: 10.1016/j.ijcas.2013.07.006

Tang, L., Wang, Y., Li, Y., Feng, H., Lu, J., and Li, J. (2009). Preparation, structure, and electrochemical properties of reduced graphene sheet films. *Adv. Funct. Mater.* 19, 2782–2789. doi: 10.1002/adfm.200900377

Tinsley, I. J. (2004). *Chemical Concepts in Pollutant Behavior*. Corvallis, OR: John Wiley & Sons.

Tiwari, K., Singh, N., Patel, M., Tiwari, M., and Rai, U. (2011). Metal contamination of soil and translocation in vegetables growing under industrial wastewater irrigated agricultural field of Vadodara, Gujarat, India. *Ecotoxicol. Environ. Saf.* 74, 1670–1677. doi: 10.1016/j.ecoenv.2011.04.029

Tongesayi, T., Fedick, P., Lechner, L., Brock, C., Le Beau, A., and Bray, C. (2013). Daily bioaccessible levels of selected essential but toxic heavy metals from the consumption of non-dietary food sources. *Food Chem. Toxicol.* 62, 142–147. doi: 10.1016/j.fct.2013.08.052

Tuinstra, F., and Koenig, J. L. (1970). Raman spectrum of graphite. *J. Chem. Phys.* 53, 1126–1130. doi: 10.1063/1.1674108

Wan, M.-W., Kan, C.-C., Rogel, B. D., and Dalida, M. L. P. (2010). Adsorption of copper (II) and lead (II) ions from aqueous solution on chitosan-coated sand. *Carbohydr. Polym.* 80, 891–899. doi: 10.1016/j.carbpol.2009.12.048

Wang, B., Luo, B., Liang, M., Wang, A., Wang, J., Fang, Y., et al. (2011). Chemical amination of graphene oxides and their extraordinary properties in the detection of lead ions. *Nanoscale* 3, 5059–5066. doi: 10.1039/c1nr10901d

Wang, S., Forzani, E. S., and Tao, N. (2007). Detection of heavy metal ions in water by high-resolution surface plasmon resonance spectroscopy combined with anodic stripping voltammetry. *Anal. Chem.* 79, 4427–4432. doi: 10.1021/ac0621773

WHO (2011). *Guidelines for Drinking-Water Quality*. Geneva: World Health Organization, 303–304.

Xiao, Y., and Li, C. M. (2008). Nanocomposites: from fabrications to electrochemical bioapplications. *Electroanalysis* 20, 648–662. doi: 10.1002/elan.200704125

Yang, T., Zhou, N., Zhang, Y., Zhang, W., Jiao, K., and Li, G. (2009). Synergistically improved sensitivity for the detection of specific DNA sequences using polyaniline nanofibers and multi-walled carbon nanotubes composites. *Biosens. Bioelectron.* 24, 2165–2170. doi: 10.1016/j.bios.2008.11.011

Yuan, X., Zhang, Y., Yang, L., Deng, W., Tan, Y., Ma, M., et al. (2015). Three-dimensional activated graphene network–sulfonate-terminated polymer nanocomposite as a new electrode material for the sensitive determination of dopamine and heavy metal ions. *Analyst* 140, 1647–1654. doi: 10.1039/C4AN02263G

Zhang, C., Ren, L., Wang, X., and Liu, T. (2010). Graphene oxide-assisted dispersion of pristine multiwalled carbon nanotubes in aqueous media. *J. Phys. Chem. C* 114, 11435–11440. doi: 10.1021/jp103745g

Zhang, L., Huang, Y., Zhang, Y., Fan, W., and Liu, T. (2015). Three-dimensional nanoporous graphene-carbon nanotube hybrid frameworks for confinement of SnS2 nanosheets: flexible and binder-free papers with highly reversible lithium storage. *ACS Appl. Mater. Interfaces* 7, 27823–27830. doi: 10.1021/acsami.5b09115

Zhang, R., and Wang, X. (2007). One step synthesis of multiwalled carbon nanotube/gold nanocomposites for enhancing electrochemical response. *Chem. Mater.* 19, 976–978. doi: 10.1021/cm062791v

Zhao, F., Wang, F., Zhao, W., Zhou, J., Liu, Y., Zou, L., et al. (2011). Voltammetric sensor for caffeine based on a glassy carbon electrode modified with nafion and graphene oxide. *Microchim. Acta* 174, 383–390. doi: 10.1007/s00604-011-0635-y

Zhao, Q., Gan, Z., and Zhuang, Q. (2002). Electrochemical sensors based on carbon nanotubes. *Electroanalysis* 14, 1609–1613. doi: 10.1002/elan.200290000

Zhao, Z.-Q., Chen, X., Yang, Q., Liu, J.-H., and Huang, X.-J. (2012). Selective adsorption toward toxic metal ions results in selective response: electrochemical studies on a polypyrrole/reduced graphene oxide nanocomposite. *Chem. Commun.* 48, 2180–2182. doi: 10.1039/C1CC16735A

Zheng, M., Jagota, A., Semke, E. D., Diner, B. A., McLean, R. S., Lustig, S. R., et al. (2003). DNA-assisted dispersion and separation of carbon nanotubes. *Nat. Mater.* 2, 338–342. doi: 10.1038/nmat877

Conflict of Interest: The authors declare that the research was conducted in the absence of any commercial or financial relationships that could be construed as a potential conflict of interest.

frontiers in Materials

ORIGINAL RESEARCH
published: 17 April 2020
doi: 10.3389/fmats.2020.00081

EDTA Modified PANI/GO Composite Based Detection of Hg (II) Ions

*Manasi Mahadik[1], Harshada Patil[1], Gajanan Bodkhe[1], Nikesh Ingle[1], Pasha Sayyad[1], Theeazen Al-Gahaouri[1], Sumedh M. Shirsat[2] and Mahendra Shirsat[1]**

[1] RUSA-Center for Advanced Sensor Technology (CAST), Department of Physics, Dr. Babasaheb Ambedkar Marathwada University, Aurangabad, India, [2] Department of Electronics and Telecommunication Engineering, Jawaharlal Nehru Engineering College, Aurangabad, India

Electrochemical recognition of Hg (II) ions utilizing EDTA modified polyaniline (PANI)/Graphene Oxide (GO) composite is reported in the present communication. Graphene Oxide (GO) synthesis was carried out by a modified Hummer's method. Electrochemical characterizations, namely cyclic voltammetry (CV) and electrochemical impedance spectroscopy (EIS), were performed before and after modification of the composite. The topographies of the PANI/GO composite and EDTA_PANI/GO electrodes were studied using AFM. Roughness parameter values were compared for confirmation of surface modification. Fourier transform infrared spectroscopy (FTIR) was utilized for the compositional analysis of PANI/GO and EDTA_PANI/GO electrodes. The EDTA_PANI/GO composite exhibits sensitivity toward Hg (II) ions when probed using the differential pulse stripping voltammetry (DPSV) technique with a lower detection limit of 2 ppb. EDTA modified SS_PANI/GO composite (PANI/GO composite deposited on a stainless-steel substrate) showed superior sensitivity in the detection of Hg (II) ions. The sensitivity was observed to extend to 1 ppb, which is smaller than the maximum contaminant level (MCL) endorsed by the Environment Protection Agency (EPA, United States).

Keywords: PANI, GO, EDTA_PANI/GO, EIS, DPSV, Hg (II) ion detection

OPEN ACCESS

Edited by:
Ilkwon Oh,
Korea Advanced Institute of Science and Technology, South Korea

Reviewed by:
Jia Chu,
Xi'an University of Science and Technology, China
Luwei Zhou,
Fudan University, China

****Correspondence:***
Mahendra Shirsat
mdshirsat.phy@bamu.ac.in

Specialty section:
This article was submitted to Smart Materials, a section of the journal Frontiers in Materials

Received: *10 December 2019*
Accepted: *19 March 2020*
Published: *17 April 2020*

Citation:
Mahadik M, Patil H, Bodkhe G, Ingle N, Sayyad P, Al-Gahaouri T, Shirsat SM and Shirsat M (2020) EDTA Modified PANI/GO Composite Based Detection of Hg (II) Ions. Front. Mater. 7:81. doi: 10.3389/fmats.2020.00081

INTRODUCTION

Heavy metals are moderately scarce in the crust of the Earth. These heavy metals are characterized by comparatively high densities and atomic numbers (Tekaya et al., 2013). Heavy metals can harm air, water, and soil quality, and in this manner, cause hazards to human wellbeing and the environment (Bánfalvi, 2011; Turdean, 2011). Among them, some metals like iron, cobalt, and zinc provide crucial nutrients or are relatively innocuous (such as ruthenium, silver, and indium) but yet can be fatal in larger amounts. Some heavy metals like cadmium, mercury, and lead are profoundly poisonous and cancer-causing above trace levels (Nagajyoti et al., 2010; Lansdown, 2013). Of these, mercury has a greater affinity to sulfur and thiol-containing molecules, resulting also in nephrotoxicity and neurotoxicity (Gumpu et al., 2015; Jan et al., 2015). For these reasons, the need arises for sensors that can acquire real-time measurements of heavy metals in water.

Electrochemical detection of heavy metal ion concentration is a versatile tool. Anodic stripping voltammetry (ASV) is the commonly used technique (Bansod et al., 2017; Deshmukh et al., 2018a).

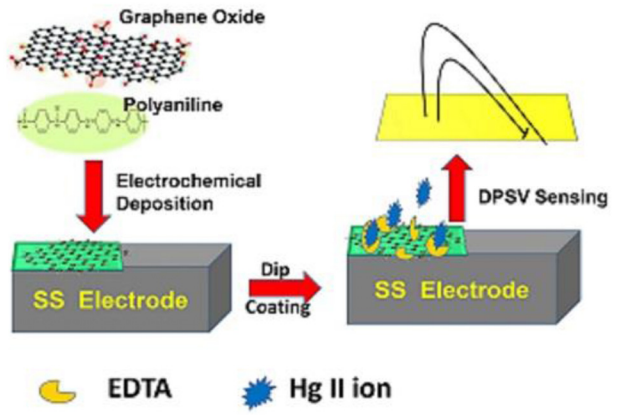

FIGURE 1 | Schematic diagram of the formation of EDTA_PANI/GO modified composite on an SS electrode for the detection of Hg (II) ions by the DPSV technique.

However, ASV has weaknesses such as instability, low sensitivity, and limits to detection (Zhao et al., 2014; Patil et al., 2018).

To conquer this problem, many advanced materials are being investigated, such as conducting polymers, carbon nanotubes (CNTs), graphene and its derivatives, and metal oxides (Choi et al., 2011; Oztekin et al., 2011; Strong et al., 2012; Lei et al., 2014). However, these advanced materials have certain limitations, e.g., organic conducting polymers have low selectivity, sensitivity, and a lack of environmental stability (Zhang et al., 2011; Das and Prusty, 2012). One of the shortcomings of carbon nanotubes (CNTs) is the entrapment of molecules at interstitial sites, which decreases reproducibility (Musameh et al., 2011; Herrera-Herrera et al., 2012).

To overcome such limitations, composite or functionalized materials are employed for the effective detection of metal ion concentration (Chen et al., 2012; Deshmukh et al., 2018b). Zhou et al. (2014) have reported on conducting polymers such as polyaniline (PANI), which performs as a *p*-type semiconductor and has demonstrated incredible potential for application because of its electrical conductivity, solubility, optical activity, easy processing, good sensitivity at room temperature, and good environmental stability. Graphene-based sensors are comparatively novel and can possibly meet the objective of quick *in situ* estimation of metals in water (Wang et al., 2010; Chang et al., 2014). It was reported that graphene has a huge hypothetical explicit surface area, high intrinsic mobility, and good electrical conductivity (Zhu et al., 2010). Graphene additionally has a honeycomb lattice with two sub-lattices bonded together with a σ-bond. Every carbon atom in the lattice contains a π orbital that offers ascent to a delocalized electron (Charlier et al., 2007; Roth and Carroll, 2015). Aside from these astounding properties, the remarkably low electronic clamor of graphene provides the opportunity to sensitively detect numerous analytes using graphene (Roth and Carroll, 2015).

It was as well reported that Graphene Oxides (GO) have layered, oxygenated graphene sheets that contain oxygen functional groups, for example, epoxides, carboxyls, hydroxyls, and alcohols, on their basal planes and edges. These groups in GO can be utilized as decent sites for surface alteration. As indicated by chemical examination, the carbon to oxygen ratio is 3:1 (Stankovich et al., 2006). GO can be reduced to nearly graphene by various chemical reduction methods; however, some promising applications of GO have recently been reported (Gilje et al., 2007; McAllister et al., 2007; Rao et al., 2009; Chen et al., 2012).

In recent years, compositing or modification of polyaniline (PANI) with carbon-based materials has received much attention. The properties of GO, such as its flat structure, charge transfer ability, incorporation of hydrophilic functional groups, and good dispersion ability in aqueous media, lead to more sites at which PANI can become attached (Dreyer et al., 2010; Vadivel et al., 2016). Also, the interaction of PANI with GO is by Π-Π stacking, electrostatic interaction, and hydrogen bonding (Wang et al., 2010). The Π-Π interaction will support faster signal processing and enhancement of the sensitivity of the sensor. Moreover, in coordination chemistry, EDTA falls within the

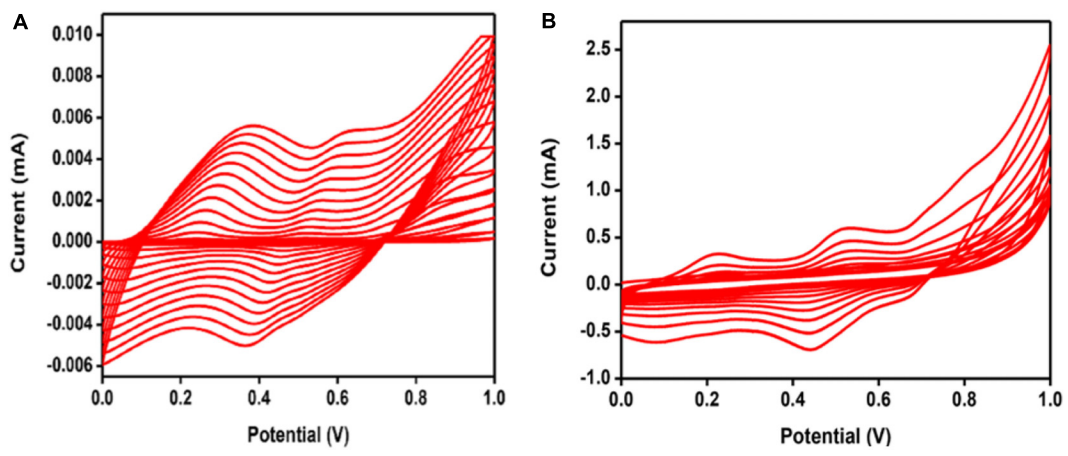

FIGURE 2 | Cyclic voltammogram recorded during the synthesis of **(A)** PANI and **(B)** PANI/GO composite for 20 potential cycles.

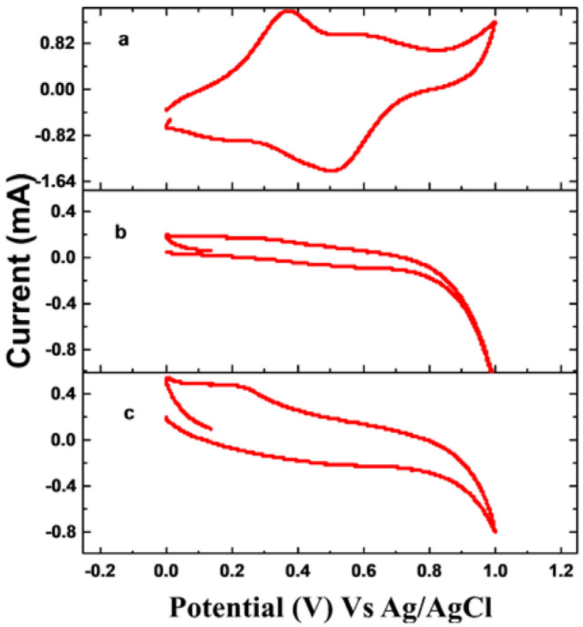

FIGURE 3 | Cyclic voltammogram of **(A)** PANI, **(B)** PANI/GO composite, and **(C)** EDTA modified PANI/GO composite electrodes in 0.5 M H_2SO_4 electrolyte.

aminopolycarboxylic acid family of ligands. Typically, EDTA ties to a metal cation through its two amines and four carboxylates. A significant number of the subsequent coordination compounds bear octahedral geometry. This octahedral geometrical structure assists with attaching the metal ion and furthermore expands the level of cross-linking inside the PANI film (Zagal et al., 1996). This implies that a composite of PANI/GO modified by EDTA will have better discrimination toward Hg (II) ion. The differential pulse stripping voltammetry (DPSV) technique is utilized for the identification of heavy metal ions.

In the present investigation, we have amalgamated a composite of polyaniline (PANI) and graphene oxide (GO), which was then modified by ethylenediaminetetraacetic acid (EDTA) for the detection of mercury ions (Hg II) using DPSV.

Over the most recent couple of years, the greater part of the information revealed shows the simultaneous identification of different heavy metal ions, which reflects the issue of selectivity (Gumpu et al., 2017; Ullah et al., 2018; Yi et al., 2019). In the present investigation, this problem is substantially resolved. Moreover, the present investigation also achieves the detection of Hg (II) ions beneath the MCL level, i.e., up to 1 ppb, with a quantifiable yield current.

MATERIALS AND METHODS

Materials

Aniline of reagent grade, sulfuric acid, and ethylenediaminetetraacetic acid (EDTA) were bought from Fluka (Germany), 1-ethyl-3-(3-dimethylaminopropyl) carbodiimide

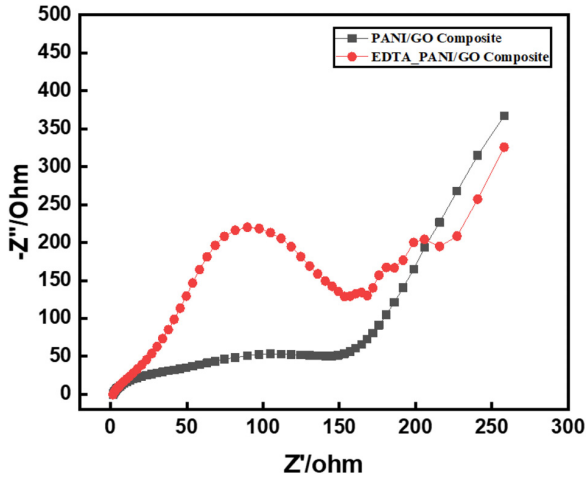

FIGURE 4 | EIS Nyquist plots of PANI/GO composite and EDTA modified PANI/GO composite electrodes in 0.5 M H_2SO_4 electrolyte.

(EDC) was acquired from Sigma Aldrich (Germany). The phosphate buffer solution (PBS) used was of pH 7. Graphene powder (~60 mesh size) was procured from Molychem (Mumbai, India), and potassium permanganate was from Kemphasol (India). An acetate buffer solution was set up by regulating 0.1 M sodium acetate (Aldrich) to the desired pH, 4.1. All the progressions were carried out in aqueous media using deionized water (DI).

Preparation of PANI/GO Composite

Graphene Oxide was produced from graphite powder using the Modified Hummer's Method (Shahriary and Athawale, 2014). Separately, PANI/GO composite was synthesized by an electrochemical method. First, 50 mL of aqueous 0.25 M aniline and 0.5 M H2SO4 suspension were mixed and maintained for

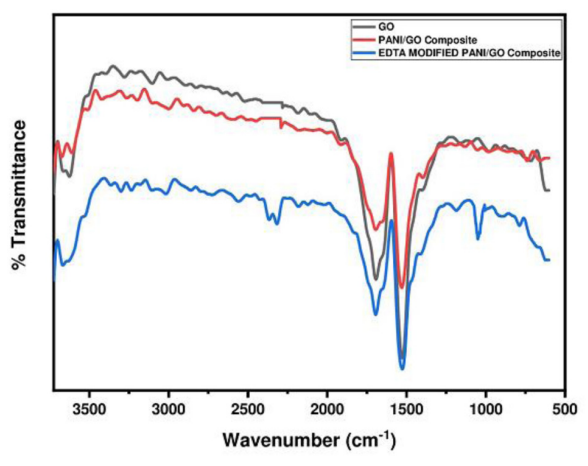

FIGURE 5 | FTIR spectrum of GO, PANI/GO composite, and EDTA modified PANI/GO composite.

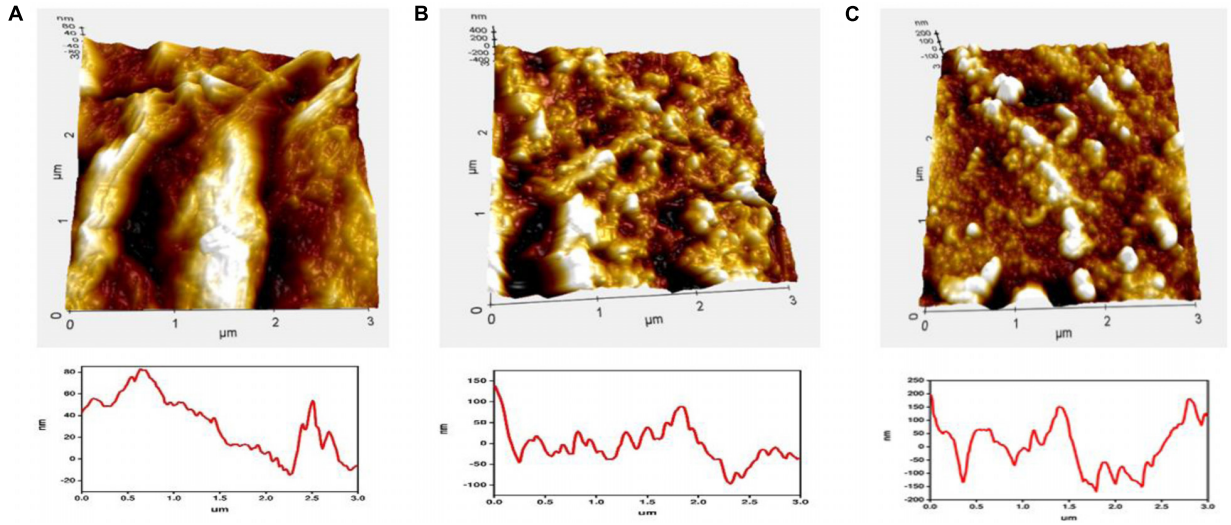

FIGURE 6 | Comparative atomic force microscope (AFM) images with respective line profiles of **(A)** GO, **(B)** PANI/GO composite, and **(C)** EDTA modified PANI/GO composite.

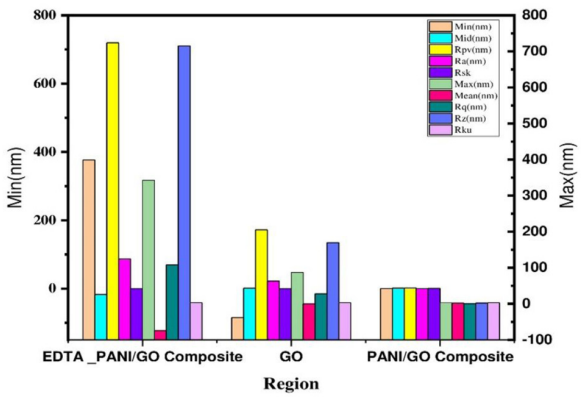

FIGURE 7 | Surface roughness parameters of bare GO, PANI/GO composite, and EDTA modified PANI/GO composite.

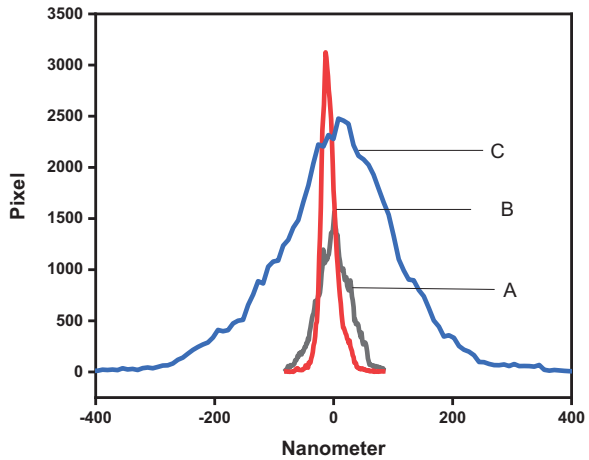

FIGURE 8 | Height distribution of (A) GO, (B) PANI/GO composite, (C) EDTA modified PANI/GO composite.

20 min, stirring. Then, 10 ml of GO in the ratio 0.1 mg/ml was mixed with the above electrolyte solution. The mixture was kept for 20 min, stirring, followed by 20 min sonication. The electrochemical synthesis of PANI/GO composite was carried out by the cyclic voltammetry method inside the potential scope of 0 to +1 V at a scan rate of 0.1 V/s for 20 cycles, with a stainless steel (SS) electrode as the working electrode, platinum as the counter electrode, and Ag/AgCl as the reference electrode. It was performed on a CHI 660C electrochemical workstation. After applying the voltage for 20 cycles, a blackish green-colored coating was observed on the working electrode. The deposited film was washed with deionized water to evacuate the concentration of electrolyte at the substrate surface, and the electrode was afterward dried at room temperature. A schematic of the synthesis of PANI/GO composite and the subsequent modification of the composite through the EDTA chelating ligand is represented in **Figure 1**.

Modification of SS_PANI/GO Composite

The SS_PANI/GO composite electrode (PANI/GO composite synthesized on a stainless steel substrate) was modified by EDTA chelation by a dip-coating method because, after polymerization of a conducting polymer, it is easy to attach another active group covalently. For modification, an EDTA suspension was set up in a 0.2 M phosphate buffer solution (PBS) at pH 7.2, having 0.1 M EDC as a triggering operator and 0.01 M EDTA. The SS PANI/GO electrode was inundated in the readied solution of EDTA and left for 12 h under non-stop stirring at room temperature. This resulted in the formation of covalent bonding

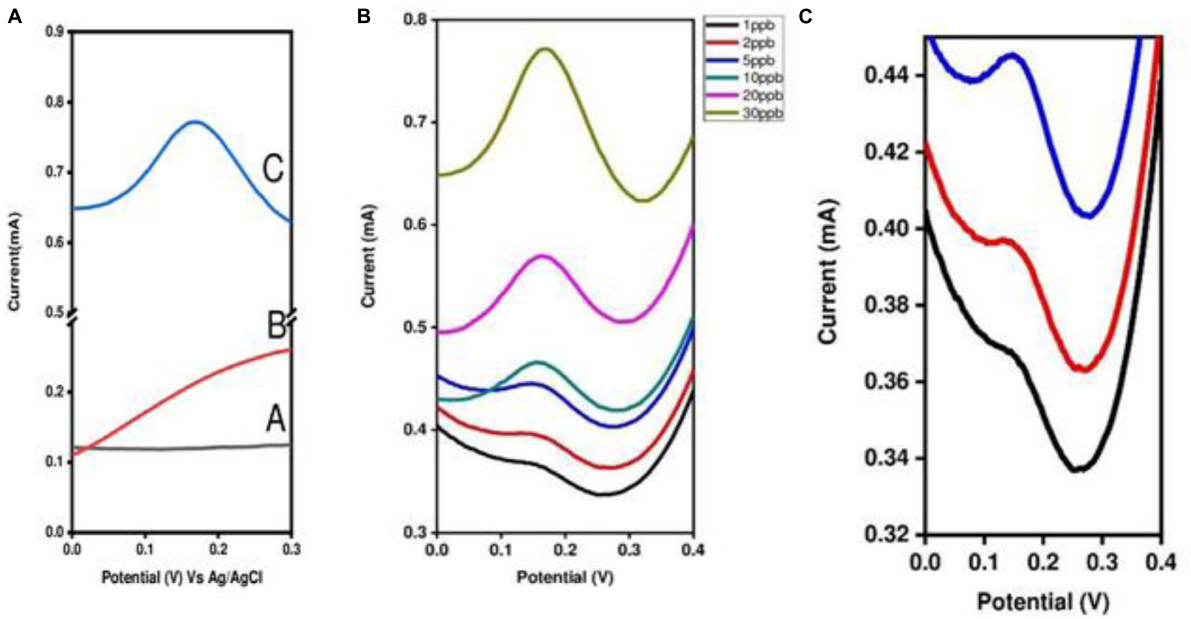

FIGURE 9 | Determination of Hg(II) ions by the DPSV technique **(A)** with three different electrodes at 30 ppb [(A) PANI/GO composite, (B) only PANI, and (C) EDTA modified PANI/GO composite] and **(B)** from 1 to 30 ppb with an EDTA modified PANI/GO composite electrode. **(C)** Enlarged image for 1 to 3 ppb with an EDTA modified PANI/GO composite electrode.

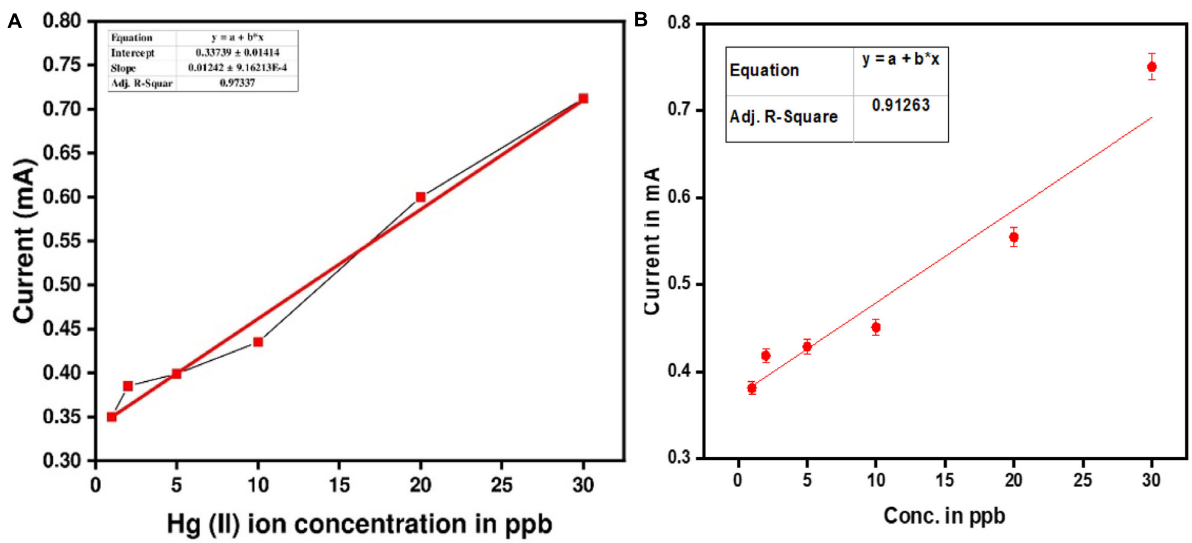

FIGURE 10 | (A) Linear relationship between Hg(II) ion concentration (in ppb) and measured current (mA). **(B)** Calibration plot of EDTA modified PANI/GO composite.

of COOH- with the NH2 group of the composite. The electrodes were subsequently cautiously washed with deionized water to expel the gently bound molecules.

Electrochemical Detection of Mercury [Hg (II)] Ions

Electrochemical detection of mercury ions was carried out by differential pulse stripping voltammetry (DPSV) employing a three-terminal arrangement at room temperature. The SS_PANI/GO/EDTA electrode filled in as the working electrode (1 cm^2) and Ag/AgCl and platinum as the reference and counter electrodes, respectively. The modified electrode was drenched in acetate buffer solution of pH 4.1 with different concentrations of Hg (II) ion and kept under continuous stirring for 2 min at 600 rpm for accumulation. This 120 s was the deposition time for Hg (II) ions. Since EDTA has the capacity of multidentate ligands to make a complex with many metal ions at various pH

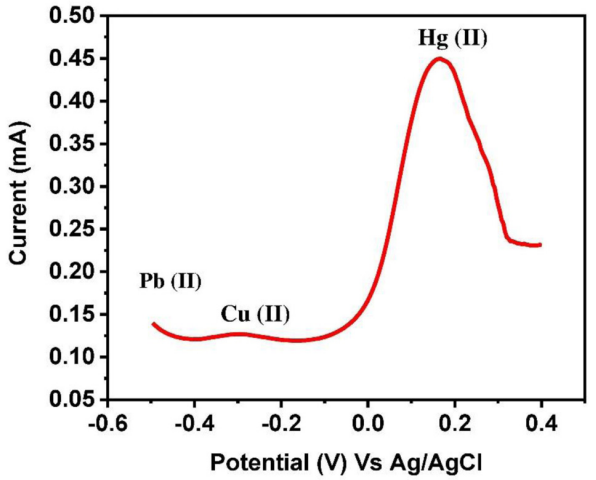

FIGURE 11 | Selective determination of Hg (II) ions from a Cu, Pb, and Hg ion-containing solution.

values, the pH for Hg (II) ions has been optimized as 4.1, achieved via the acetate buffer solution. After completing accumulation, DPSV scan was applied in the potential range of 0.0 to 0.4 V to oxidize mercury ions from the electrode surface.

RESULTS AND DISCUSSION

Electrochemical Synthesis of PANI/GO Composite

Electrochemical synthesis of PANI/GO composite was performed by cyclic voltammetry, as portrayed in **Figure 1**, between the range 0 to +1 V for 20 cycles on the SS electrode at a 0.1 V/s scan rate. **Figure 2** illustrates the relative cyclic voltammogram recorded during the amalgamation of PANI and PANI/GO composite film. During the synthesis of PANI, a greenish-colored film was observed to form, while for, the composite, a blackish green-colored film formed.

During synthesis, increase in the current in the PANI/GO composite as compared to PANI is clearly exhibited in **Figure 2B**, which relates to the development of composite film on the SS electrode. The conductivity of the film increments by expanding the applied potential, which affirms the formation of PANI/GO composite.

Electrochemical Characterization

Figure 3 represents the electrochemical behavior of PANI, PANI/GO Composite, and EDTA modified PANI/GO Composite in 0.5 M H2SO4 solution. The oxidation and reduction peaks of PANI are easily observed, and PANI/GO composite exhibits lower oxidation potential compared to PANI and EDTA modified PANI/GO composite. The PANI/GO composite exhibits an increase in oxidation potential after modification by EDTA due to the electrostatic interaction present on the surfaces of the electrodes.

The PANI/GO composite and EDTA modified PANI/GO electrodes were characterized by EIS in the frequency range of 1to 1000 Hz in 0.5 M H2SO4, which is a functioning strategy for evaluation of procedures occurring at electrode surfaces. **Figure 4** shows the EIS Nyquist plots of the PANI/GO composite and EDTA modified PANI/GO composite electrodes. The EIS for EDTA modified PANI/GO composite electrodes indicates a moderately large semi-circular province, which exhibits a large interfacial electron transfer resistance between the redox probe and the modified PANI/GO composite electrode. The PANI/GO electrodes show lower interfacial electron resistance in the Nyquist plot, which indicates that the structure of the PANI/GO composite electrode stimulates electron transfer, which demonstrates the superb electrochemical action of the PANI/GO composite electrode.

FTIR Analysis

The PANI/GO composite and EDTA modified PANI/GO composite were further characterized by FTIR spectroscopy, as depicted in **Figure 5**. Peaks at 1690 cm^{-1} and 1510 cm^{-1} in every spectrum confirm the presence of C = O and C-O functional groups. C = N stretching is clearly observed at 1120 cm^{-1} in the EDTA modified PANI/GO composite. This stretching indicates strong interaction with the EDTA ligand. The peak perceived at 2340 cm^{-1} relates to the (isocyanate group) N = C = O asymmetric vibrations.

Surface Morphologies of GO, PANI/GO Composite, and EDTA Modified PANI/GO

The surface morphologies of the prepared samples were studied with an atomic force microscope (AFM). **Figure 6** represents the surface morphology of (A) bare GO, (B) PANI/GO composite, and (C) EDTA modified PANI/GO composite, which plainly reveals the transformations in surface morphology. The plot in **Figure 7** distinguishes the roughness parameters of graphene oxide drop-casted on a glass substrate, PANI/GO composite synthesized by the electrochemical method, and PANI/GO composite modified with EDTA by dip coating.

Figure 8 shows the height distribution of (A) GO, (B) PANI/GO composite, and (C) EDTA modified PANI/GO composite. **Figure 8** evidently shows that there is an increasing distribution height from bare graphene oxide to PANI/GO composite to EDTA modified PANI/GO composite.

COMPARATIVE AND SELECTIVE DETERMINATION OF HG(II) IONS BY THE DPSV METHOD

The best method for the determination of mercury ions was elaborated on in section "Electrochemical Detection of Mercury [Hg (II)] Ions," Determination was performed by the differential pulse stripping voltammetry technique (DPSV) with EDTA modified PANI/GO composite on an SS electrode. The modified SS electrode was immersed in a mercury ion solution and, by following the methodology mentioned in

section "Electrochemical Detection of Mercury [Hg (II)] Ions," measurement was carried out. **Figure 9A**, represents the comparative detection of Hg (II) ions at 30 ppb with three different electrodes, that is, (A) PANI/GO composite, (B) only PANI, and (C) EDTA modified PANI/GO composite. From this, it can be easily concluded that EDTA modified PANI/GO composite is more sensitive than the PANI and PANI/GO composite electrode. Thereafter, the determination of Hg (II) ions with the EDTA modified PANI/GO composite electrode was performed at different concentrations down to as low as 1 ppb (**Figure 9B**). As the concentration increases, the measured value of the current also increases linearly, as depicted in **Figure 10A**. An estimation of the determination and linearity of the device has been made by way of the calibration plot in **Figure 10B**. The gadget revealed a linearity factor R^2 = 0.91283 for room temperature estimation. The sensitivity of the SS_EDTA modified PANI/GO composite was 12.42 mA/ppb, and the limit of detection (LOD) was 0.612 ppb.

The limit of detection was determined by utilizing the equation,

$$\text{LOD} = 3.3 \times (\text{Standard deviation of the regression line}/\text{Slope})$$

Selective determination was carried out from the solution containing Cu, Pb, and Hg ions. For selectivity, the potential (vs. Ag/AgCl) was applied from −0.6 to 0.4 V. The sharp apex is observed at 0.2 V, which clearly indicates the presence of Hg (II) ions (**Figure 11**). It can be concluded that the EDTA modified PANI/GO composite electrode is selective to Hg (II) ions only.

CONCLUSION

An EDTA modified PANI/GO composite on stainless steel (SS) electrode for use in the detection of Hg (II) ions was synthesized and characterized effectively. Electron transfer resistance between the redox probe and EDTA modified PANI/GO composite or PANI/GO composite was clearly observed. Modification by the EDTA chelating ligand increases the affinity of PANI/GO composite toward Hg (II) ions. An EDTA modified PANI/GO electrode shows excellent response to Hg (II) ions from 30 to 1 ppb, which is well below MCL (2 ppb). A successful and linear determination of Hg (II) was performed by differential pulse stripping voltammetry (DPSV) down to 1 ppb.

DATA AVAILABILITY STATEMENT

The datasets generated for this study are available on request to the corresponding author.

AUTHOR CONTRIBUTIONS

MM and MS conceived of the presented idea and developed the theory. MM performed the experiments and computations. HP and GB encouraged the investigation and verified the analytical methods. NI, PS, TA-G, and SS assisted with CV, FTIR, and EIS measurements. All authors discussed the outcomes and added to inscribe the final manuscript. MS contributed to the final version of the manuscript and supervised the project.

FUNDING

The authors extend their earnest gratitude to the Inter-University Accelerator Center (IUAC), New Delhi, India (UFR no. 62321 and UFR no. 62320), SARTHI-Government of Maharashtra, DST—SERB, New Delhi (Project No. EEQ/2017/000645), UGC—DAE CSR (RRCAT), Indore (Project No. CSR-IC-BL66/CRS-183/2016-17/847), Rashtria Uchachatar Shiksha Abhiyan (RUSA), the UGC-SAP Programme (F.530/16/DRS-I/2016 (SAP-II) Dt.16-04-2016), and DST-FIST (Project No. SR/FST/PSI-210/2016(C) dtd. 16/12/2016) for providing financial support.

REFERENCES

Bánfalvi, G. (2011). "Heavy metals, trace elements and their cellular effects," in *in Cellular Effects of Heavy Metals*, ed. G. Banfalvi (Berlin: Springer), 3–28. doi: 10.1007/978-94-007-0428-2_1

Bansod, B., Kumar, T., Thakur, R., Rana, S., and Singh, I. (2017). A review on various electrochemical techniques for heavy metal ions detection with different sensing platforms. *Biosens. Bioelectron.* 94, 443–455. doi: 10.1016/j.bios.2017.03.031

Chang, J., Zhou, G., Christensen, E. R., Heideman, R., and Chen, J. (2014). Graphene-based sensors for detection of heavy metals in water: a review. *Anal. Bioanal. Chem.* 406, 3957–3975. doi: 10.1007/s00216-014-7804-x

Charlier, J.-C., Eklund, P., Zhu, J., and Ferrari, A. (2007). "Electron and phonon properties of graphene: their relationship with carbon nanotubes," in *Carbon Nanotubes*, eds M. Endo, S. Iijima, and M. S. Dresselhaus (Berlin: Springer), 673–709. doi: 10.1007/978-3-540-72865-8_21

Chen, K., Lu, G., Chang, J., Mao, S., Yu, K., Cui, S., et al. (2012). Hg (II) ion detection using thermally reduced graphene oxide decorated with functionalized gold nanoparticles. *Anal. Chem.* 84, 4057–4062. doi: 10.1021/ac3000336

Choi, H.-J., Jeon, I.-Y., Kang, S.-W., and Baek, J.-B. (2011). Electrochemical activity of a polyaniline/polyaniline-grafted multiwalled carbon nanotube mixture produced by a simple suspension polymerization. *Electroch. Acta* 56, 10023–10031. doi: 10.1016/j.electacta.2011.08.103

Das, T. K., and Prusty, S. (2012). Review on conducting polymers and their applications. *Polym. Plast. Technol. Eng.* 51, 1487–1500.

Deshmukh, M. A., Celiesiute, R., Ramanaviciene, A., Shirsat, M. D., and Ramanavicius, A. (2018a). EDTA_PANI/SWCNTs nanocomposite modified electrode for electrochemical determination of copper (II), lead (II) and mercury (II) ions. *Electroch. Acta* 259, 930–938. doi: 10.1016/j.electacta.2017.10.131

Deshmukh, M. A., Patil, H. K., Bodkhe, G. A., Yasuzawa, M., Koinkar, P., Ramanaviciene, A., et al. (2018b). EDTA-modified PANI/SWNTs nanocomposite for differential pulse voltammetry based determination of Cu (II) ions. *Sens. Actuators B Chem.* 260, 331–338. doi: 10.1016/j.snb.2017.12.160

Dreyer, D. R., Park, S., Bielawski, C. W., and Ruoff, R. S. (2010). The chemistry of graphene oxide. *Chem. Soc. Rev.* 39, 228–240. doi: 10.1039/b917103g

Gilje, S., Han, S., Wang, M., Wang, K. L., and Kaner, R. B. (2007). A chemical route to graphene for device applications. *Nano Lett.* 7, 3394–3398. doi: 10.1021/nl0717715

Gumpu, M. B., Sethuraman, S., Krishnan, U. M., and Rayappan, J. B. B. (2015). A review on detection of heavy metal ions in water–an electrochemical approach. *Sens. Actuators B Chem.* 213, 515–533. doi: 10.1016/j.snb.2015.02.122

Gumpu, M. B., Veerapandian, M., Krishnan, U. M., and Rayappan, J. B. B. (2017). Simultaneous electrochemical detection of Cd (II), Pb (II), As (III) and Hg (II) ions using ruthenium (II)-textured graphene oxide nanocomposite. *Talanta* 162, 574–582. doi: 10.1016/j.talanta.2016.10.076

Herrera-Herrera, A. V., González-Curbelo, M. Á, Hernández-Borges, J., and Rodríguez-Delgado, M. Á (2012). Carbon nanotubes applications in separation science: a review. *Anal. Chim. Acta* 734, 1–30. doi: 10.1016/j.aca.2012.04.035

Jan, A. T., Azam, M., Siddiqui, K., Ali, A., Choi, I., and Haq, Q. M. (2015). Heavy metals and human health: mechanistic insight into toxicity and counter defense system of antioxidants. *Int. J. Mol. Sci.* 16, 29592–29630. doi: 10.3390/ijms161226183

Lansdown, A. B. (2013). *The Carcinogenicity of Metals: Human Risk Through Occupational and Environmental Exposure*. London: Royal Society of Chemistry.

Lei, W., Si, W., Xu, Y., Gu, Z., and Hao, Q. (2014). Conducting polymer composites with graphene for use in chemical sensors and biosensors. *Microch. Acta* 181, 707–722. doi: 10.1007/s00604-014-1160-6

McAllister, M. J., Li, J.-L., Adamson, D. H., Schniepp, H. C., Abdala, A. A., Liu, J., et al. (2007). Single sheet functionalized graphene by oxidation and thermal expansion of graphite. *Chem. Mater.* 19, 4396–4404. doi: 10.1021/cm0630800

Musameh, M. M., Hickey, M., and Kyratzis, I. L. (2011). Carbon nanotube-based extraction and electrochemical detection of heavy metals. *Res. Chem. Int.* 37, 675–689. doi: 10.1007/s11164-011-0307-x

Nagajyoti, P. C., Lee, K. D., and Sreekanth, T. (2010). Heavy metals, occurrence and toxicity for plants: a review. *Environ. Chem. Lett.* 8, 199–216. doi: 10.1007/s10311-010-0297-8

Oztekin, Y., Yazicigil, Z., Ramanaviciene, A., and Ramanavicius, A. (2011). Polyphenol-modified glassy carbon electrodes for copper detection. *Sensors and Actuators B Chemical* 152, 37–48. doi: 10.1016/j.snb.2010.09.057

Patil, H. K., Deshmukh, M. A., Bodkhe, G. A., Shirsat, S. M., Asokan, K., and Shirsat, M. D. (2018). Dimethylglyoxime modified swift heavy oxygen ions irradiated polyaniline/single walled carbon nanotubes composite electrode for detection of cobalt ions. *Materi. Res. Express* 5:065048. doi: 10.1088/2053-1591/aaccb3

Rao, C. E. N. E. R., Sood, A. E. K., Subrahmanyam, K. E. S., and Govindaraj, A. (2009). Graphene: the new two-dimensional nanomaterial. *Angew. Chem. Int. Ed.* 48, 7752–7777. doi: 10.1080/1061186X.2018.1437920

Roth, S., and Carroll, D. (2015). *One-Dimensional Metals: Conjugated Polymers, Organic Crystals, Carbon Nanotubes and Graphene*. Hoboken, NJ: John Wiley & Sons.

Shahriary, L., and Athawale, A. A. (2014). Graphene oxide synthesized by using modified hummers approach. *Int. J. Renew. Energy Environ. Eng.* 2, 58–63.

Stankovich, S., Piner, R. D., Chen, X., Wu, N., Nguyen, S. T., and Ruoff, R. S. (2006). Stable aqueous dispersions of graphitic nanoplatelets via the reduction of exfoliated graphite oxide in the presence of poly (sodium 4-styrenesulfonate). *J. Mater. Chem.* 16, 155–158. doi: 10.1039/b512799h

Strong, V., Dubin, S., El-Kady, M. F., Lech, A., Wang, Y., Weiller, B. H., et al. (2012). Patterning and electronic tuning of laser scribed graphene for flexible all-carbon devices. *ACS Nano* 6, 1395–1403. doi: 10.1021/nn204200w

Tekaya, N., Saiapina, O., Ouada, H. B., Lagarde, F., Ouada, H. B., and Jaffrezic-Renault, N. (2013). Ultra-sensitive conductometric detection of pesticides based on inhibition of esterase activity in *Arthrospira platensis*. *Environ. Pollut.* 178, 182–188. doi: 10.1016/j.envpol.2013.03.013

Turdean, G. L. (2011). Design and development of biosensors for the detection of heavy metal toxicity. *Int. J. Electrochem.* 2011:5.

Ullah, N., Mansha, M., Khan, I., and Qurashi, A. (2018). Nanomaterial-based optical chemical sensors for the detection of heavy metals in water: recent advances and challenges. *TrAC Trends Anal. Chem.* 100, 155–166.

Vadivel, S., Theerthagiri, J., Madhavan, J., and Maruthamani, D. (2016). Synthesis of polyaniline/graphene oxide composite via ultrasonication method for photocatalytic applications. *Mater. Focus* 5, 393–397. doi: 10.1166/mat.2016.1367

Wang, H., Hao, Q., Yang, X., Lu, L., and Wang, X. (2010). Effect of graphene oxide on the properties of its composite with polyaniline. *ACS App. Mater. Interfaces* 2, 821–828. doi: 10.1021/am900815k

Yi, W., He, Z., Fei, J., and He, X. (2019). Sensitive electrochemical sensor based on poly (L-glutamic acid)/graphene oxide composite material for simultaneous detection of heavy metal ions. *RSC Adv.* 9, 17325–17334. doi: 10.1039/c9ra01891c

Zagal, J., Del Rio, R., Retamal, B., and Biaggio, S. (1996). Stability and electrical properties of polyaniline films formed with EDTA and FeEDTA in the electrolyte. *J. Appl. Electroch.* 26, 95–101. doi: 10.1007/bf00248194

Zhang, Y.-J., Lin, Y.-W., Chang, C.-C., and Wu, T.-M. (2011). Conducting and magnetic behaviors of polyaniline coated multi-walled carbon nanotube composites containing monodispersed magnetite nanoparticles. *Synth. Metals* 161, 937–942. doi: 10.1016/j.synthmet.2011.02.026

Zhao, D., Guo, X., Wang, T., Alvarez, N., Shanov, V. N., and Heineman, W. R. (2014). Simultaneous detection of heavy metals by anodic stripping voltammetry using carbon nanotube thread. *Electroanalysis* 26, 488–496. doi: 10.1021/acs.analchem.6b04724

Zhou, Q., Li, Y., Huang, L., Li, C., and Shi, G. (2014). Three-dimensional porous graphene/polyaniline composites for high-rate electrochemical capacitors. *J. Mater. Chem. A* 2, 17489–17494. doi: 10.1039/c4ta03639e

Zhu, Y., Murali, S., Cai, W., Li, X., Suk, J. W., Potts, J. R., et al. (2010). Graphene and graphene oxide: synthesis, properties, and applications. *Adv. Mater.* 22, 3906–3924.

Conflict of Interest: The authors declare that the research was conducted in the absence of any commercial or financial relationships that could be construed as a potential conflict of interest.

frontiers in Materials

ORIGINAL RESEARCH
published: 15 May 2020
doi: 10.3389/fmats.2020.00093

Sulfur Dioxide (SO_2) Detection Using Composite of Nickel Benzene Carboxylic (Ni_3BTC_2) and OH-Functionalized Single Walled Carbon Nanotubes (OH-SWNTs)

*Nikesh Ingle[1], Savita Mane[1], Pasha Sayyad[1], Gajanan Bodkhe[1], Theeazen AL-Gahouari[1], Manasi Mahadik[1], Sumedh Shirsat[2] and Mahendra D. Shirsat[1]**

[1] Department of Physics, RUSA Centre for Advanced Sensor Technology, Dr. Babasaheb Ambedkar Marathwada University, Aurangabad, India, [2] Department of Electronics and Telecommunication Engineering, Jawaharlal Nehru Engineering College, Aurangabad, India

In the present investigation, a composite of "nickel benzene carboxylic (Ni_3BTC_2)" and "OH-functionalized single walled carbon nanotubes (OH-SWNTs)" was synthesized using the solvothermal method. The synthesized Ni_3BTC_2/OH-SWNTs were drop casted on gold micro electrode tip on Si/SiO_2 substrate. The synthesized composite materials were characterized by X-ray diffraction (XRD) for structural analysis, electrical analysis using current-voltage (I/V) characteristics, Field emission scanning electron microscopy (FESEM) for surface morphology, Field effect transistor (FET) by using transfer and output characteristics, and spectroscopic analysis using Fourier-transform infrared spectroscopy (FTIR). This composite was used for the detection of SO_2. The proper incorporated OH-SWNTs in Ni_3BTC_2 MOF exhibits increased conductivity and sensing performance (better response and recovery time and repeatability). This work reveals that the composite of Ni_3BTC_2/OH-SWNTs can be used for reversible sensing of SO_2 gas in ChemFET modality at room temperature.

Keywords: metal-organic framework, single walled carbon nanotube, chemiresistive sensor, SO_2 gas sensing, reproducibility

OPEN ACCESS

Edited by:
Jaehwan Kim,
Inha University, South Korea

Reviewed by:
Jie Zhang,
Chongqing University, China
Roli Verma,
Tel Aviv University, Israel

****Correspondence:***
Mahendra D. Shirsat
mdshirsat.phy@bamu.ac.in

Specialty section:
This article was submitted to Smart Materials, a section of the journal Frontiers in Materials

Received: *09 December 2019*
Accepted: *26 March 2020*
Published: *15 May 2020*

Citation:
Ingle N, Mane S, Sayyad P, Bodkhe G, AL-Gahouari T, Mahadik M, Shirsat S and Shirsat MD (2020) Sulfur Dioxide (SO_2) Detection Using Composite of Nickel Benzene Carboxylic (Ni_3BTC_2) and OH-Functionalized Single Walled Carbon Nanotubes (OH-SWNTs). Front. Mater. 7:93. doi: 10.3389/fmats.2020.00093

INTRODUCTION

During the last two decades, Metal-Organic frameworks (MOFs) have attracted considerable attention among research communities due to their unique tunable physical and chemical properties which build on the selecting organic linker and central metal (Campbell et al., 2015; Avery et al., 2016; Bodkhe et al., 2019). MOFs have large surface areas with high porosity. MOFs have been used for various applications like gas adsorption, storage, separation, sensors, and catalysis (Koo et al., 2016; Ullman et al., 2016; Dmello et al., 2018; Li H. et al., 2018). MOFs are newly introduced materials in electronics and optoelectronic devices (Dolgopolova and Shustova, 2016; Campbell and Dincă, 2017; Stassen et al., 2017). Campbell and Dincă (2017) reported successful synthesis of $Cu_3(HITP)_2$ and $Ni_3(HITP)_2$ MOFs with high electrical conductivity and reported that it was able to be used for chemiresistive ammonia vapor sensing. The results obtained

for $Cu_3(HITP)_2$ show a good response to ammonia, whereas $Ni_3(HITP)_2$ did not show any observable response to ammonia vapor under identical experimental conditions.

SWNTs are well known for their unique electrical, mechanical, and thermal properties (Patil et al., 2017; Deshmukh et al., 2018). These properties make them a unique material for sensing applications. Pristine CNTs are not very active in a chemical process. Therefore, activation/functionalization of CNTs need to be performed through various methods viz. wet chemical methods, photo-oxidation, and oxygen-plasma or gas phase treatment, which shows great chemical reactivity of carbon nanotubes (Patil et al., 2017; Gurova et al., 2019; Hoang et al., 2019). The CNTs are familiarized with a graphite surface which contains oxygen-containing groups, mainly carboxyl and hydroxyl (Zhang et al., 2003; Yook et al., 2010; Liang et al., 2016). This introduces the possibility of further modification which will affect the solubility and reactivity of OH-SWNTs.

There are many research groups focusing on SO_2 gas sensor due to its toxicity (Farmanzadeh and Ardehjani, 2018; Li Q. et al., 2018; Nagarajan and Chandiramouli, 2018; Khan et al., 2019; Zhou et al., 2019). The Occupational Safety and Health Administration (OSHA) permissible exposure limit (PEL) for SO_2 is 5 ppm. Advancement in civilization has had severe impacts on the environment. Researchers across the globe are taking crucial efforts to scale new materials for the detection hazardous gases. Some of them are using functionalized or composites of OH-SWNTs for SO_2 detection (Li Q. et al., 2018; Nagarajan and Chandiramouli, 2018).

SWNTs have walls of graphene sheet which leads to π–π electron conjugation to interact with functional group. The functional groups on the SWNTs outer side and tips make them more active channels in a chemical reaction, which is why they have better sensitivity and repeatability. Importantly, Wen et al., 2015 reported that the SWNTs act as an excellent backbone and conductive surface with Ni-MOF. In the present investigation, the composite of Ni_3BTC_2/OH-SWNTs was synthesized through a solvothermal method and it was used for the detection of Sulfur dioxide (SO_2) in ChemFET modality. To the best of our knowledge, no one has yet reported reversible SO_2 gas sensing on a Ni_3BTC_2/OH-SWNTs composite.

EXPERIMENTAL

The Gold Microelectrodes Pattern

The gold micro electrodes on Si/SiO_2 substrate were prepared as reported earlier (Shirsat et al., 2009). The gold microelectrodes had a 3 μm gap between the two electrode tips, which had a length of 200 μm, and these microelectrodes were deposited on Si (thickness 525 μm) /SiO_2 (100 nm thickness) using a standard photolithography process. The gold (Au) had a thickness of 180 nm and the underneath layer of chromium (Cr) had a thickness of 20 nm, and these were deposited on Si/SiO_2 substrate. Finally, the desired micro-pattern was developed using Lift-off technique.

Functionalization of SWNTs

The SWNTs oxidation process was carried out by using HNO_3 oxidizing agent (Hu et al., 2003). The purified 0.1 g of SWNTs (Sigma Aldrich) was mixed with 20 ml of HNO_3. Then the mixture was continuously stirred for 20 h. The prepared suspension releases bubbles which indicates oxygen formation. Then, resultant suspension was ultrasonicated for 60 min at medium power level (VWR 100C ultrasonic bath) followed by centrifugation (REMI R-24) at 12,000 rpm for 60 min. The decanted suspension was sucked using a syringe and used for further process.

Synthesis of Ni_3BTC_2/OH-SWNTs Composite

0.1 mol of oxidized OH-SWNTs mixed with nickel (II) acetate tetrahydrate (molychem, 98%) and 3 mmol Trimesic acid (Sigma-Aldrich, 95%) mixed with 20 ml of N,N-Dimethylformamide (DMF) (Sigma-Aldrich, 99.8%) was continuously stirred for 30 min. at 1000 rpm. The solvothermal method was used for the synthesis of the desired material by using a Teflon-lined stainless-steel autoclave, sealed, and placed in a furnace. The mixture was heated for 140°C for 24 h. After the completion of the reaction, the mixture was cooled at room temperature. The resultant composite was filtered and washed with DMF. Remaining pure precipitate powder was dried at room temperature.

Finally, 0.1 mmol composite of Ni_3BTC_2/OH-SWNTs was mixed with 10 ml DMF solvent and sonicated for 60 min. at medium power. A 0.2 μl drop from the resultant suspension was used to bridge a 3 μm gap between two gold microelectrodes on Si/SiO_2 substrate, as shown in the schematic and optical image (**Figure 1**).

RESULTS AND DISCUSSION

X-Ray Diffraction

The X-ray diffraction patterns were measured using Bruker D8 Advanced system, with a potential difference of 40 kV

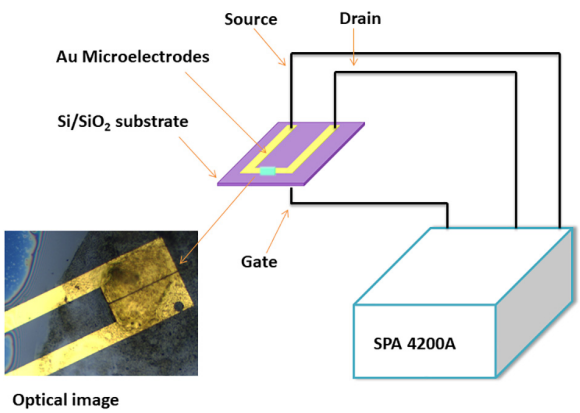

FIGURE 1 | Schematic and optical image for a single microelectrode, drop casted with Ni_3BTC_2/OH-SWNTs material.

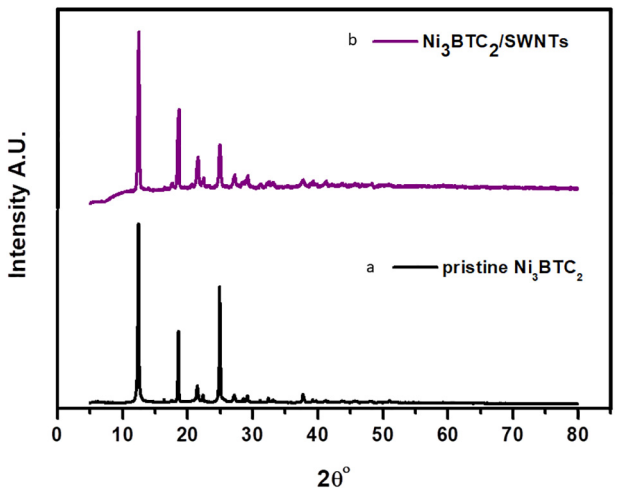

FIGURE 2 | XRD patterns, **(a)** pristine Ni_3BTC_2 and **(b)** composite of Ni_3BTC_2/OH-SWNTs.

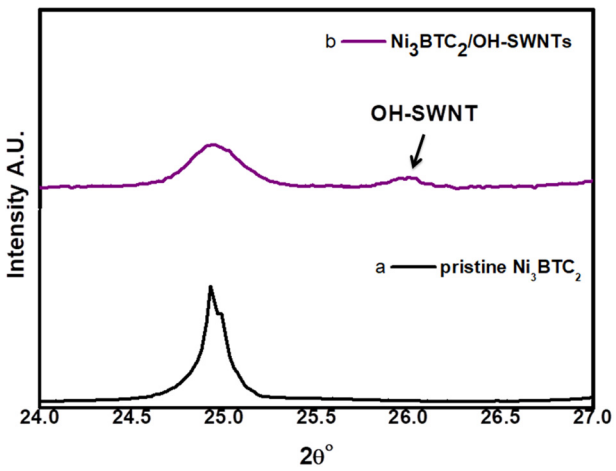

FIGURE 3 | XRD patterns (2θ° range 24° to 27°), **(a)** pristine Ni_3BTC_2 and **(b)** composite of Ni_3BTC_2/OH-SWNTs.

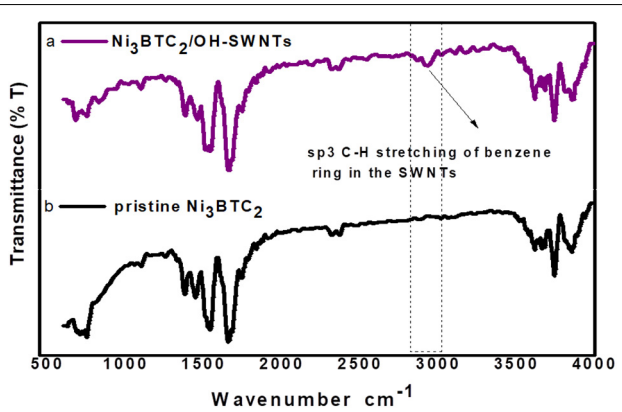

FIGURE 4 | FTIR spectras, **(a)** pristine Ni_3BTC_2 and **(b)** composite Ni_3BTC_2/OH-SWNTs materials.

and a current of 40 mA with source Cu Kα λ = 1.5406 Å radiation. The XRD patterns of pristine Ni_3BTC_2 and Ni_3BTC_2/OH-SWNTs composite were shown in **Figure 2**. The pristine Ni_3BTC_2 signature peaks (12.54°, 18.49°, 21.29°, and 25°) of the diffraction pattern are well matched with reported data (Jin et al., 2013; **Figure 2a**). The percentage of crystallinity for pristine Ni_3BTC_2 was 43.3%. The reduction in crystallinity was observed (27.1%) after incorporation of OH-SWNTs in Ni_3BTC_2, calculated by DIFFRAC.EVA software. The composite of Ni_3BTC_2/OH-SWNTs diffraction pattern (**Figure 2b**) having the same 2θ° peaks position with a decrease in intensity compared with pristine Ni_3BTC_2 pattern confirms there was no change in the crystal structure of Ni_3BTC_2. The peak intensity decreased for Ni_3BTC_2/OH-SWNTs diffraction pattern, indicating incorporation of OH-SWNTs inside the Ni_3BTC_2 MOF. The XRD pattern of functionalized OH-SWNTs incorporated in Ni_3BTC_2 is shown in **Figure 2b**, whereas the extra peak at $2\theta^o = 26^o$ confirms the existence of OH-SWNTs (**Figure 3b**) which is attributed to the graphite structure (002) of OH-SWNTs (Xiao and Xu, 2012).

The crystallite size of pristine Ni_3BTC_2 and composite Ni_3BTC_2/OH-SWNTs was calculated using the Debye–Scherrer's formula in Equation (1).

$$D = \frac{0.9\lambda}{\beta \cos\theta} \qquad (1)$$

where D is crystallite size, λ is the wavelength of x-ray source radiation, i.e., CuKα wavelength is 1.5406Å, β is full width at half maxima (FWHM) calculated from Gauss fitting, pristine Ni_3BTC_2 is 0.126, and composite Ni_3BTC_2/OH-SWNTs is 0.122. The θ° (12.44°) is the Braggs angle of diffraction. The calculated crystallite size for pristine Ni_3BTC_2 was 705.2 Å and for composite Ni_3BTC_2/OH-SWNTs was 730.1 Å.

Fourier-Transform Infrared Spectroscopy (FTIR)

The FTIR spectra was recorded using Bruker Alpha ATR with a ZnSe window in the range of 4000–500 cm^{-1}. The recorded graph shows a transmittance spectra of pristine Ni_3BTC_2 and composite of Ni_3BTC_2/OH-SWNTs as shown in **Figures 4a,b**, respectively). The spectra of pristine Ni_3BTC_2 and composite of Ni_3BTC_2/OH-SWNTs samples have been confirmed by the asymmetric and symmetric stretching peaks of the –C = O group at 1620 and 1416 cm^{-1}, respectively. The –C-OC stretching (etheric) group was found at 1080 cm^{-1} (Saber-Samandari and Gazi, 2013). The peaks at 1145 cm^{-1} were attributed to C-O group, whereas the C-C vibrations band presented at 1456 cm^{-1}. The peak at 1632 cm^{-1} was attributed to C = O functional group. The aromatic C = C stretching vibration band corresponds with 1539–1658 cm^{-1}. The intensity of mentioned peak decreases in composite Ni_3BTC_2/OH-SWNTs spectra (**Figure 4b**) as compared to pristine Ni_3BTC_2 is due to the interaction between

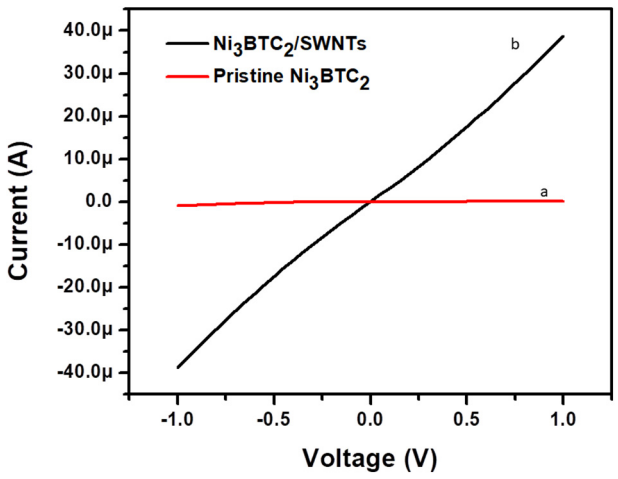

FIGURE 5 | Electrical (I-V) characteristics of **(a)** pristine Ni_3BTC_2 and **(b)** composite of Ni_3BTC_2/OH-SWNTs.

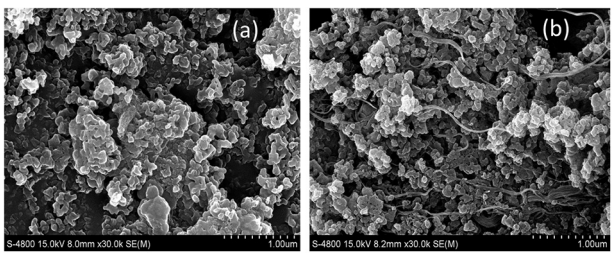

FIGURE 6 | Field emission scanning electron microscopy (FESEM) images of **(a)** pristine Ni_3BTC_2 and **(b)** composite of Ni_3BTC_2/OH-SWNTs.

carboxyl groups of Ni_3BTC_2 and amide groups of functionalized SWNTs (Karkeh-abadi et al., 2016). The stretching peak of O-H at 3024 cm^{-1} appeared in the composite material, which confirms the carboxylic group gained oxidation with HNO_3. Defect formation in sp3 C-H stretching of the benzene ring in the OH-SWNTs is shown in **Figure 4b**.

Current-Voltage (I/V) Characterization

The I/V studies were carried out using a semiconductor parameter analyzer (SPA, Keithley 4200A) at room temperature. West bond wire bounder 7476D was used to have electrical contact from gold microelectrodes to PCB for further measurements. Experimental measurements were carried out at a constant voltage range from −1 V to 1 V. Resistance of pristine Ni_3BTC_2 and composite of Ni_3BTC_2/OH-SWNTs was determined by using an inverse slope of I–V curve. Both curves of pristine and composite materials were passed through origin and show an ohmic nature of materials (**Figure 5**). The pristine material resistance was 8.85 MΩ and after incorporation of OH-SWNTs resistance decreased substantially to 25.5 KΩ. It was clearly observed that functionalized OH-SWNTs actively help in the enhancement of conduction. The micro network of OH-SWNTs into Ni_3BTC_2 has created a channel connectivity. Moreover, free electron mobility was increased due to the incorporation of OH-SWNTs into pristine Ni_3BTC_2 material. This new network has provided a conductive pathway that can charge transport though the micro network of SWNTs into Ni_3BTC_2 (Choi et al., 2012; Eletskii et al., 2015).

Field Emission Scanning Electron Microscopy (FESEM)

The morphology of pristine Ni_3BTC_2 and composite of Ni_3BTC_2/SWNTs was studied using a Field emission scanning electron microscopy (FESEM) (using Hitachi High-Tech, S-4800) (**Figure 6**). **Figure 6a** reveals the microstructure of pristine Ni_3BTC_2 in which the OH-SWNTs were apparently encapsulated, forming a micro-network structure which is visible in **Figure 6b**.

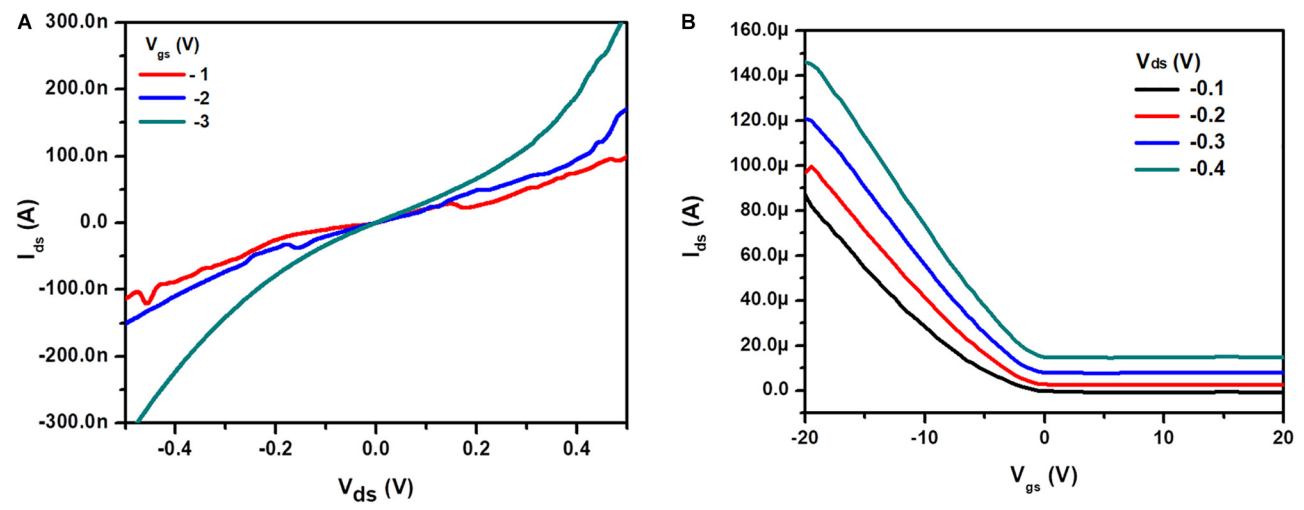

FIGURE 7 | FET measurements of Ni_3BTC_2 /OH-SWNTs composite material **(A)** Output and **(B)** Transfer characteristics.

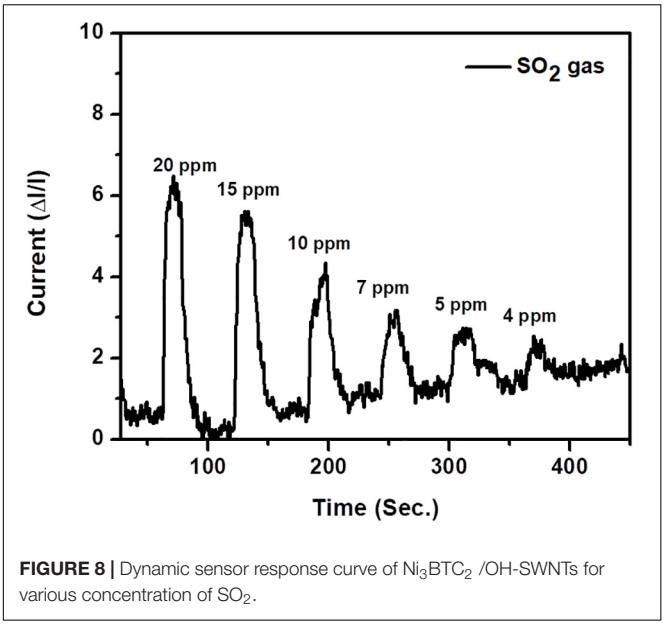

FIGURE 8 | Dynamic sensor response curve of Ni_3BTC_2 /OH-SWNTs for various concentration of SO_2.

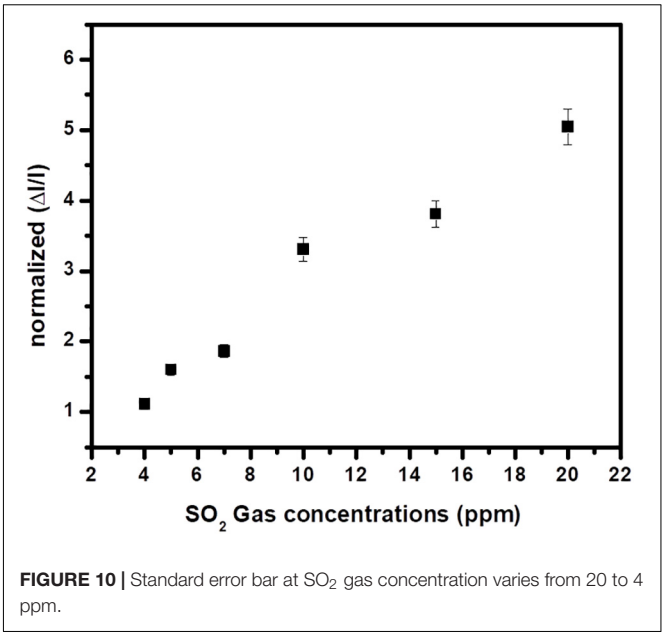

FIGURE 10 | Standard error bar at SO_2 gas concentration varies from 20 to 4 ppm.

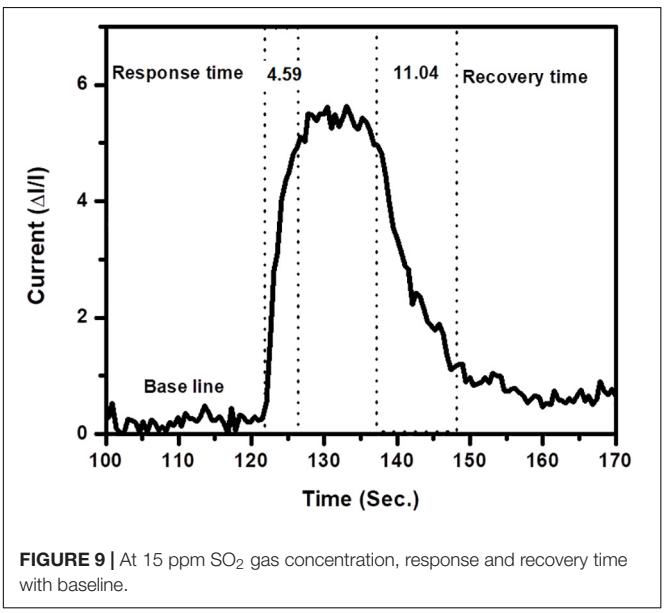

FIGURE 9 | At 15 ppm SO_2 gas concentration, response and recovery time with baseline.

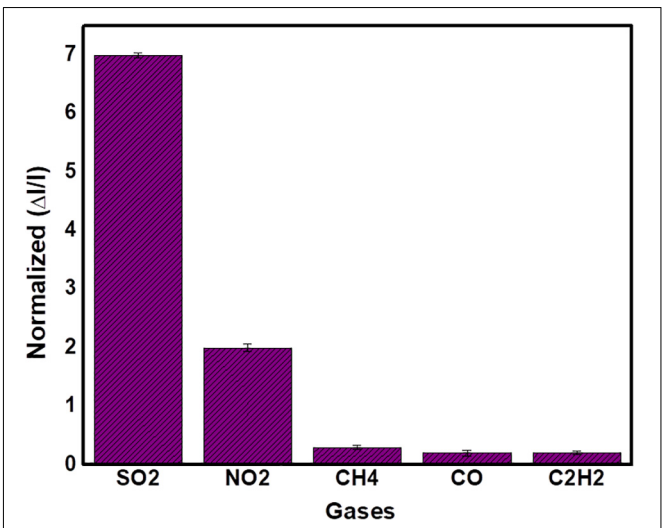

FIGURE 11 | Selectivity of the Ni_3BTC_2/OH-SWNTs composite sensor toward 5 ppm of various gas analytes.

Field Effect Transistor (FET) Measurements

The transfer and output characteristics of Ni_3BTC_2/OH-SWNTs were studied to understand the FET behavior using SPA-4200A (**Figure 7**). In this case, composite material Ni_3BTC_2/OH-SWNTs shows p-channel behavior. For FET measurement, OH-SWNTs conducting nature has effectively contributed in composite material. In output characteristics V_{ds} measurements were carried out between −0.5 to 0.5 V by varying V_{gs} −1 to −3 V with step 1V. Negative back gated voltage has created a repulsive force between the oxide layer (free charge carrier) and the silicon substrates. It has affected the depletion region populated by positive charges, which is attracted toward electrons and results in a decrease in the depletion barrier. This confirms the presence of holes as a majority charge carrier in channel. This in turn confirms the p-type behavior of Ni_3BTC_2/OH-SWNTs composite. Transfer characteristic was recorded at V_{ds} −0.1 to −0.4V with step 0.1 V by changing V_{gs} −20 to 20 V. This confirms the switching behavior of the device with threshold voltage (V_{TH}) 1.5 V at −0.1V V_{ds}.

The charge carrier mobility was calculated by using Equation (2),

$$\mu = \pm \left(\frac{\partial \sigma}{\partial \mathrm{Vgs}}\right)\left(\frac{t}{\mathrm{Cox}}\right) \quad (1)$$

The $\frac{\partial \sigma}{\partial \mathrm{Vgs}}$ was calculated from linear fit slope from transfer characteristics at V_{ds} −0.1, where t was thickness of

composite material Ni_3BTC_2/OH-SWNTs deposited on gold microelectrodes ∼50 μm and C_{ox} is capacitance per unit area of 100nm SiO_2 layer calculated by Equation (3)

$$C_{ox} = \frac{3.9\varepsilon_0}{t_0} \quad (2)$$

where, ε_0 is the permittivity of free space constant, i.e., 8.85×10^{-12} C^2/Nm^2 and t_0 is the thickness of SiO_2 layer, i.e., 100 nm. The charge carrier mobility of $\sim 2.18 \times 10^{-6}$ cm^2 V^{-1} s^{-1} was calculated from Equation (2) at V_{ds} −0.1 V.

CHEMFET SENSING STUDIES

The sensing study was carried out by using an indigenously developed dynamic gas sensing system. The V_{gs} (-3 V) and V_{ds} (-0.4 V) was kept constant. Data collection was done by Keithley SPA-4200A source measuring unit at room temperature. The gas measuring device (Ni_3BTC_2/OH-SWNTs) was kept in an ∼8 cm^3 seal packed chamber. Inserting gas concentration was balanced by using a mass flow controller (Alicat) flow rate 200 SCCM. A tedlar bag was used for accumulating different concentrations of SO_2 gas. Dry air was used to inhabit initial conditions, i.e., for baseline and balancing gas concentrations to avoid any impact from humidity. Once the initial condition was achieved, the sensor was exposed to gas analytes with various concentrations ranging from 4 to 20 ppm at a constant value of V_{gs} (-3 V) and V_{ds} (-0.4 V). The sensor device having composite material Ni_3BTC_2/OH-SWNTs shows excellence response and recovery for various (higher to lower) concentrations of SO_2 (**Figure 8**). The response time of 4.59 s. with a recovery time of 11.04 s. was recorded at 15 ppm of SO_2 concentration (**Figure 9**). The calibration plot is shown in **Figure 10**. It shows a little more deviation at higher concentrations as compared to lower concentrations.

The FET study confirms p-type Ni_3BTC_2/OH-SWNTs composite material with holes as a majority carrier. When electron acceptor (SO_2) gas analytes (Yao et al., 2011) come in contact with p-type material, it causes a transfer of electrons from the composite material, as shown in Equation (4), and generates a number of vacancies (holes). It was responsible for decreasing the resistance of the material while interacting with SO_2 gas analytes.

$$SO_2 + e^- = SO_2^- \quad (3)$$

The sensitivity of Ni_3BTC_2/OH-SWNTs composite sensor was investigated by exposing 5 ppm concentration of various gas analytes like NO_2, CH_4, CO, and C_2H_2, as shown in **Figure 11**. Using the same experimental conditions, SO_2 gas showed a much higher sensitivity when compared with other tested gas analytes. These indicate that Ni_3BTC_2/OH-SWNTs composite sensor was highly sensitive toward SO_2 gas. The low response for CH_4, CO, and C_2H_2 was attributed to the nucleophilic nature of these gases (Zhang et al., 2017).

CONCLUSION

Pristine Ni_3BTC_2 and composite of Ni_3BTC_2/OH-SWNTs were successfully synthesized using the solvothermal method. The electrical, structural, surface morphological, and spectroscopic characterization confirms the successful incorporation of OH-SWNTs in Ni_3BTC_2 MOF. The FET measurement confirms p-type behavior of Ni_3BTC_2/OH-SWNTs composite material. The ChemFET sensing at constant value of V_{gs} (-3 V) and V_{ds} (−0.4 V) shows an excellent response. The incorporated OH-SWNTs in Ni_3BTC_2 MOF enhances the sensing properties of the composite material. The lower detection limit of 4ppm with a response time of 5 s. and recovery time of 10 s. was observed. The sensor shows excellent repeatability.

DATA AVAILABILITY STATEMENT

All datasets generated for this study are included in the article/supplementary material.

AUTHOR CONTRIBUTIONS

NI, SM, and PS contributed to experimental work. NI contributed to formal analysis, GB contributed to XRD and FTIR analysis, and TA-G, MM, and SS contributed to FET analysis and gas sensing. NI contributed to the investigation and writing of the original draft. MS contributed to conceptualization, writing the review, editing, and supervision.

FUNDING

We extend their sincere thanks to Inter University Accelerator Center (IUAC), New Delhi, India (UFR nos. 62320 and 62321), UGC-DAE CSR (RRCAT), Indore (Project No. CSR-IC BL66/CRS- 183/2016-17/847), DST-SERB, New Delhi (Project No. EEQ/2017/000645), Rashtria Uchachatar Shiksha Abhiyan (RUSA), Government of Maharashtra, UGC-SAP Programme (F.530/16/DRS-I/2016 (SAP-II) Dt.16-04-2016) and DST-FIST (Project No. SR/FST/PSI-210/2016(C) dtd. 16/12/2016) for providing financial support.

REFERENCES

Avery, A. D., Zhou, B. H., Lee, J., Lee, E.-S., Miller, E. M., Ihly, R., et al. (2016). Tailored semiconducting carbon nanotube networks with enhanced thermoelectric properties. *Nat. Energy* 1:16033.

Bodkhe, G. A., Deshmukh, M. A., Patil, H. K., Shirsat, S. M., Srihari, V., Pandey, K. K., et al. (2019). Field effect transistor based on proton conductive metal organic framework (CuBTC). *J. Phys. D* 52:335105. doi: 10.1088/1361-6463/ab1987

Campbell, M., and Dincă, M. (2017). Metal-organic frameworks as active materials in electronic sensor devices. *Sensors* 17:1108. doi: 10.3390/s17051108

Campbell, M. G., Sheberla, D., Liu, S. F., Swager, T. M., and Dincã, M. (2015). Cu3 (hexaiminotriphenylene) 2: an electrically conductive 2D metal-organic framework for chemiresistive sensing. *Angew. Chem. Int. Ed.* 54, 4349–4352. doi: 10.1002/anie.201411854

Choi, H. H., Lee, J., Dong, K.-Y., Ju, B.-K., and Lee, W. (2012). Gas sensing performance of composite materials using conducting polymer/single-walled carbon nanotubes. *Macromol. Res.* 20, 143–146. doi: 10.1007/s13233-012-0030-5

Deshmukh, M. A., Patil, H. K., Bodkhe, G. A., Yasuzawa, M., Koinkar, P., Ramanaviciene, A., et al. (2018). EDTA-modified PANI/SWNTs nanocomposite for differential pulse voltammetry based determination of Cu (II) ions. *Sens. Actuators B Chem.* 260, 331–338. doi: 10.1016/j.snb.2017.12.160

Dmello, M. E., Sundaram, N. G., and Kalidindi, S. B. (2018). Assembly of ZIF−67 metal-organic framework over tin oxide nanoparticles for synergistic chemiresistive CO2 gas sensing. *Chem. A Eur. J.* 24, 9220–9223. doi: 10.1002/chem.201800847

Dolgopolova, E. A., and Shustova, N. B. (2016). Metal-organic framework photophysics: optoelectronic devices, photoswitches, sensors, and photocatalysts. *MRSBulletin* 41, 890–896. doi: 10.1557/mrs.2016.246

Eletskii, A. V., Knizhnik, A. A., Potapkin, B. V., and Kenny, J. M. (2015). Electrical characteristics of carbon nanotube-doped composites. *Phys. Uspekhi* 58, 209–251. doi: 10.3367/ufne.0185.201503a.0225

Farmanzadeh, D., and Ardehjani, N. A. (2018). Adsorption of O3, SO2 and NO2 molecules on the surface of pure and Fe-doped silicon carbide nanosheets: a computational study. *Appl. Surf. Sci.* 462, 685–692. doi: 10.1016/j.apsusc.2018.08.150

Gurova, O. A., Arhipov, V. E., Koroteev, V. O., Guselnikova, T. Y., Asanov, I. P., Sedelnikova, O. V., et al. (2019). Purification of single−walled carbon nanotubes using acid treatment and magnetic separation. *Physi. Stat. Solidi* 256:1800742. doi: 10.1002/pssb.201800742

Hoang, N. D., Van Cat, V., Nam, M. H., Phan, V. N., Le, A. T., and Van Quy, N. (2019). Enhanced SO2 sensing characteristics of multi-wall carbon nanotubes based mass-type sensor using two-step purification process. *Sens. Actuators A Phys.* 295, 696–702. doi: 10.1016/j.sna.2019.06.046

Hu, H., Zhao, B., Itkis, M. E., and Haddon, R. C. (2003). Nitric acid purification of single-walled carbon nanotubes. I. *Phys. Chem. B* 107, 13838–13842. doi: 10.1021/jp035719i

Jin, L.-N., Liu, Q., and Sun, W.-Y. (2013). Room temperature solution-phase synthesis of flower-like nanostructures of [Ni3 (BTC) 2·12H2O] and their conversion to porous NiO. *Chin. Chem. Lett.* 24, 663–667. doi: 10.1016/j.cclet.2013.05.001

Karkeh-abadi, F., Saber-Samandari, S., and Saber-Samandari, S. (2016). The impact of functionalized CNT in the network of sodium alginate-based nanocomposite beads on the removal of Co(II) ions from aqueous solutions. *J. Hazard. Mater.* 312, 224–233. doi: 10.1016/j.jhazmat.2016.03.074

Khan, M. A. H., Rao, M. V., and Li, Q. (2019). Recent advances in electrochemical sensors for detecting toxic gases: NO2, SO2 and H2S. *Sensors* 19:905. doi: 10.3390/s19040905

Koo, W.-T., Choi, S.-J., Kim, S.-J., Jang, J.-S., Tuller, H. L., and Kim, I.-D. (2016). Heterogeneous sensitization of metal-organic framework driven metal@ metal oxide complex catalysts on an oxide nanofiber scaffold toward superior gas sensors. *J. Am. Chem. Soc.* 138, 13431–13437. doi: 10.1021/jacs.6b09167

Li, H., Wang, K., Sun, Y., Lollar, C. T., Li, J., and Zhou, H.-C. (2018). Recent advances in gas storage and separation using metal-organic frameworks. *Materialstoday* 21, 108–121. doi: 10.1016/j.mattod.2017.07.006

Li, Q., Wu, J., Huang, L., Gao, J., Zhou, H., Shi, Y., et al. (2018). Sulfur dioxide gas-sensitive materials based on zeolitic imidazolate framework-derived carbon nanotubes. *J. Mater. Chem. A* 6, 12115–12124. doi: 10.1039/c8ta02036a

Liang, S., Li, G., and Tian, R. (2016). Multi-walled carbon nanotubes functionalized with a ultrahigh fraction of carboxyl and hydroxyl groups by ultrasound-assisted oxidation. *J. Mater. Sci.* 51, 3513–3524. doi: 10.1007/s10853-015-9671-z

Nagarajan, V., and Chandiramouli, R. (2018). A novel approach for detection of NO2 and SO2 gas molecules using graphane nanosheet and nanotubes-A density functional application. *Diam. Relat. Mater.* 85, 53–62. doi: 10.1016/j.diamond.2018.03.028

Patil, H. K., Deshmukh, M. A., Gaikwad, S. D., Bodkhe, G. A., Asokan, K., Yasuzawa, M., et al. (2017). Influence of oxygen ions irradiation on polyaniline/single walled carbon nanotubes nanocomposite. *RPC* 130, 47–51. doi: 10.1016/j.radphyschem.2016.07.030

Saber-Samandari, S., and Gazi, M. (2013). Removal of mercury (II) from aqueous solution using chitosan-graft-polyacrylamide semi-IPN hydrogels. *Separ. Sci. Technol.* 48, 1382–1390. doi: 10.1080/01496395.2012.729121

Shirsat, M. D., Bangar, M. A., Deshusses, M. A., Myung, N. V., and Mulchandani, A. (2009). Polyaniline nanowires-gold nanoparticles hybrid network based chemiresistive hydrogen sulfide sensor. *Appl. Phys. Lett.* 94:083502. doi: 10.1063/1.3070237

Stassen, I., Burtch, N., Talin, A., Falcaro, P., Allendorf, M., and Ameloot, R. (2017). An updated roadmap for the integration of metal-organic frameworks with electronic devices and chemical sensors. *Chem. Soc. Rev.* 46, 3185–3241. doi: 10.1039/c7cs00122c

Ullman, A. M., Brown, J. W., Foster, M. E., Léonard, F., Leong, K., Stavila, V., et al. (2016). Transforming MOFs for energy applications using the guest@MOF concept. *Inorg. Chem.* 55, 7233–7249. doi: 10.1021/acs.inorgchem.6b00909

Wen, P., Gong, P., Sun, J., Wang, J., and Yang, S. (2015). Design and synthesis of Ni-MOF/CNT compositesand rGO/carbon nitride composites for anasymmetric supercapacitor with high energy andpower density. *J. Mater. Chem. A* 3, 13874–13883.

Xiao, F., and Xu, Y. (2012). Electrochemical co-deposition and characterization of MnO2/SWNT composite for supercapacitor application. *J. Mater. Sci. Mater. Electron.* 24, 1913–1920. doi: 10.1007/s10854-012-1034-9

Yao, F., Duong, D. L., Lim, S. C., Yang, S. B., Hwang, H. R., Yu, W. J., et al. (2011). Humidity-assisted selective reactivity between NO2and SO2gas on carbonnanotubes. *J. Mater. Chem.* 21:4502. doi: 10.1039/c0jm03227a

Yook, J. Y., Jun, J., and Kwak, S. (2010). Amino functionalization of carbon nanotube surfaces with NH3 plasma treatment. *Appl. Surf. Sci.* 256, 6941–6944. doi: 10.1016/j.apsusc.2010.04.075

Zhang, D., Liu, J., Jiang, C., Li, P., and Sun, Y. (2017). High-performance sulfur dioxide sensing properties of layer-by-layer self-assembled titania-modified graphene hybrid nanocomposite. *Sens. Actuators B Chem.* 245, 560–567. doi: 10.1016/j.snb.2017.01.200

Zhang, J., Zou, H., Qing, Q., Yang, Y., Li, Q., Liu, Z., et al. (2003). Effect of chemical oxidation on the structure of single-walled carbon nanotubes. *J. Phys. Chem. B* 107, 3712–3718.

Zhou, Q., Zeng, W., Chen, W., Xu, L., Kumar, R., and Umare, A. (2019). High sensitive and low-concentration sulfur dioxide (SO2) gas sensor application of heterostructure NiO-ZnO nanodisks. *Sens. Actuators B Chem.* 298:126870.

Conflict of Interest: The authors declare that the research was conducted in the absence of any commercial or financial relationships that could be construed as a potential conflict of interest.

frontiers in Materials

ORIGINAL RESEARCH
published: 26 June 2020
doi: 10.3389/fmats.2020.00184

PANI-ZnO Cladding-Modified Optical Fiber Biosensor for Urea Sensing Based on Evanescent Wave Absorption

S. N. Botewad[1], V. G. Pahurkar[2], G. G. Muley[2], D. K. Gaikwad[1,3], Gajanan A. Bodkhe[4], Mahendra D. Shirsat[4] and P. P. Pawar[1]*

[1] Department of Physics, Dr. Babasaheb Ambedkar Marathwada University, Aurangabad, India, [2] Department of Physics, SantGadge Baba Amravati University, Amravati, India, [3] Department of Physics, ACS College, Dharangaon, India, [4] RUSA Centre for Advanced Sensor Technology, Department of Physics, Dr. Babasaheb Ambedkar Marathwada University, Aurangabad, India

In the present investigation, we demonstrated a simple, rapid, and highly sensitive cladding-modified optical fiber urea sensor based on the evanescent wave absorption (EWA) technique. Cladding modification was performed over a 2-cm unclad portion of optical fiber using a polyaniline-zinc oxide (PANI-ZnO) matrix with enzyme-Urease (Urs) cross-linked to it using glutarldehyde as a cross-linking agent. The PANI-ZnO matrix was characterized by X-ray diffraction, scanning electron microscopy, ultraviolet-visible, and Fourier transform-infrared spectroscopy to explore its various properties. The developed sensor shows a linear response to urea concentration in the range 10 nM−1 M in the form of the absorption spectrum at a wavelength of ∼250 nm with specific selectivity. Under the proper conditions (storage at temperature 4°C after each measurement), it shows 40-day stability without any decrement in the intensity of the absorption spectrum. Thus, the developed sensor is highly sensitive, stable, and specific, with a lower detection limit of a urea concentration of 10 nM.

Keywords: optical fiber, urea, PANI-ZnO, evanescent wave absorption, cladding modification

OPEN ACCESS

Edited by:
Jaehwan Kim,
Inha University, South Korea

Reviewed by:
Zhen Shou Jiang,
Shandong Normal University, China
Jie Zhang,
Chongqing University, China
Nianbing Zhong,
Chongqing University of Technology, China

***Correspondence:**
D. K. Gaikwad
dhammajyotg26@gmail.com

Specialty section:
This article was submitted to Smart Materials, a section of the journal Frontiers in Materials

Received: *23 December 2019*
Accepted: *19 May 2020*
Published: *26 June 2020*

Citation:
Botewad SN, Pahurkar VG, Muley GG, Gaikwad DK, Bodkhe GA, Shirsat MD and Pawar PP (2020) PANI-ZnO Cladding-Modified Optical Fiber Biosensor for Urea Sensing Based on Evanescent Wave Absorption. Front. Mater. 7:184. doi: 10.3389/fmats.2020.00184

INTRODUCTION

Biosensors are utilized in multidimensional fields, including medicine, home diagnosis (Mehrotra, 2016), agriculture (Velasco-Garcia and Mottram, 2003), the military (Rossi et al., 2000), environmental monitoring (Rodriguez-Mozaz et al., 2005), food preservation, fishery industries (Terry et al., 2005) etc. A biosensor is an analytical device that has extraordinary characteristics such being compact, cost-effective, ultra-sensitive, and specific and having shorter response and recovery times along with very low analyte concentration detection limits (Luong et al., 1997). Generally, a biosensor comprises three main components, viz. a bioreceptor (enzyme, nucleic acid, cells, etc.), a physicochemical transducer (electrochemical, optical, piezoelectric, thermometric, ion-sensitive, magnetic, or acoustic, etc.), and an immobilization matrix. Each component contributes to improving the reliability of the biosensor in practical applications (Turner et al., 1987; Monošík et al., 2012). The worldwide scientific and academic community has invented various types of schemes and materials for fabricating biosensors (Banica, 2012). In a sense, biosensors can be classified according to the bioreceptor and transducers used for their fabrication. As regards the selection of a physicochemical transducer, optical fiber has received incredible consideration for

chemical and biosensing applications. This is because of its distinct features viz. its miniature size, low response time, immunity to electricity, robustness in use, high sensitivity, low weight, requirement of a small sample amount, remote controllability, and facility to use in various geometries etc. (Monk and Walt, 2004; Fan et al., 2008; Martins et al., 2013). In optical fiber biosensors, the evanescent wave absorption (EWA) scheme has become popular, promising, and much used due to the enhanced sensitivity, high resolution, and low detection limit it provides (Zawawi et al., 2013; Zhong et al., 2016). Principally, an evanescent wave (EW) field is generated in optical fiber due to light decaying exponentially into a small portion of the cladding, and this is utilized for the fabrication of cladding-modified intrinsic optical fiber sensors (Sai et al., 2010; Bharadwaj et al., 2011). When applying this scheme, several critical factors arise, such as the proper incidence angle, the adjustable geometry of optical fiber (bending, tapering, etc.), and the thickness of the immobilization matrix. However, enhanced sensor credibility and performance can be achieved by the proper optimization of these factors (Iadicicco et al., 2011).

Technically, in an optical fiber biosensor, the immobilization matrix plays a considerable role, as it decides the performance as well as the efficiency of the biosensor. In biosensors, the immobilization matrix is used to maintain the stable reactivity and safe residency of bioreceptor (Ramakrishna and Sai, 2016). In an optical fiber sensor, it is used as a modified cladding that responds to chemical and biochemical reactions occurring on its surface. Thus, diverse materials with attractive properties have been synthesized and used as an immobilization matrix. For biosensor applications, intrinsic conducting polymers (ICPs) are emerging as a new class and are used as an immobilization matrix. Due to their extraordinary morphological, structural, optical, mechanical, and electrical properties, they are considered the most promising candidate for the immobilization of bioreceptor species. In the field of biosensors, two types of ICPs are considered to be especially promising: polyaniline (PANI) and polypyrrole (PPy). Polyaniline has many desirable features and properties, such as intriguing physical properties, ease of synthesis, low cost, extraordinary electrical, and optical properties, a sufficiently large surface area (morphology), adjustable transport properties, and environmental stability (Kim et al., 2010). As well as being synthesizable via a variety of methods, its sufficient solubility in innumerable solvents and capability to fabricate versatile composites/nanocomposites due to its functionality-rich chemical skeleton can be efficiently exploited for biosensor applications. With the incorporation of metal oxide nanoparticles, the properties of pure PANI change drastically, which is useful for sensing applications and improving sensitivity, selectivity, and stability (Tahir et al., 2005; Prakash et al., 2013). Owing to their good structural and optical properties and biocompatibility, PANI-metal nanoparticle composites have proven to be promising candidates for bioreceptor immobilization (Dhawan et al., 2009).

Urea (NH_2CONH_2) is a chemical species found everywhere in nature. Urea is present in the human body due to protein metabolism (Singh et al., 2008). A concentration of urea above the optimal level generates various dangerous diseases, included kidney and liver malfunction, chronic or acute renal failure, urinary tract obstruction, dehydration, shock, burns, and gastrointestinal bleeding, whereas, below a certain level, it produces hepatic failure, nephritic syndrome, and cachexia (Mostafaei and Ashkan, 2012; Mostafaei and Nasirpouri, 2014). However, urea is also found in agriculture, dairy industries, and fishery industries and performs various roles. Thus, the selective and rapid determination of urea concentration is a vital need for the abovementioned fields. Worldwide, different groups are working on the development of biosensors for detection of urea. In earlier years, various research groups have devoted their efforts to fabricating a urea biosensor using different techniques and different matrices for enzyme immobilization. Ahmad et al. reported a ZnO nanorod-based urea sensor using an electrochemical technique. The fabricated sensor shows high sensitivity toward urea in the linear range 0.001–24.0 mM, with a 10-μM lower detection limit (Ahmad et al., 2014). By modifying the ZnO structure, i.e., creating nanosheets, the same research group developed a potentiometric urea sensor and detected urea concentration with the linear range 0.05–2.0 mM with a lower detection limit of 0.019 μM and with a very short response time of ∼5 S (Ahmad et al., 2015). Babu et al. prepared a freestanding and binder-free electrospun PVdF-HFP/Ni-Co nanofiber-based urea biosensor. The developed sensor showed a rapid response time (5 S), a lower detection limit of 12 μM, and a wide linear range of 20 μM−2 mM for urea concentration detection (Babu et al., 2017). A Ali et al. reported on a potentiometric urea biosensor based on urease immobilization onto chitosan/cobalt oxide (CS/Co_3O_4) nanocomposite for the detection of urea within the range $1*10^{-4}$-$8*10^{-2}$ M with a 12-s response time (Ali et al., 2015). In a previous study, we reported on a urea sensor using pure polyaniline for cladding modification but did not achieve the desired results in terms of linearity, stability, detection limit, etc. (Botewad et al., 2018). Thus, improvement in the abovementioned characteristics of the PANI-ZnO nanocomposite sensor is required, and cladding modification and enzyme immobilization have been selected as the means to do so.

Herein, we present the EWA optical fiber intrinsic biosensor for the selective sensing and quantification of urea. The biosensor is fabricated by cladding modification with PANI-ZnO nanocomposite as an immobilization matrix. The sophisticated straight geometry of the optical fiber transducer and the experimental setup have been adapted for the development of the sensor. Using the PANI-ZnO cladding-modified matrix provides superior sensing parameter values for the developed biosensor for selective detection of urea.

EXPERIMENTAL

Materials

In the present investigation, all provided chemicals were of analytical reagent (AR) grade and used as received without any further purification. Aniline (monomer), ferric chloride (oxidant), zinc chloride, and sodium hydroxide were purchased from Fisher Scientific, India, and used to synthesize PANI-ZnO nanocomposite. The bio-receptor enzyme-urease (Urs) was

procured from Sisco Research Laboratories (SRL), India. The analyte urea, cross-linking agent glutarldehyde solution (25%), interference species glucose, thiourea, ascorbic acid, L- alanine, L-arginine were purchased from SD Fine Chemicals, India. For the formation of buffer solution (Phosphate buffer pH 7.4), potassium dihydrogen orthophosphate and sodium hydroxide were purchased from SD Fine Chemicals, India. Hydrofluoric acid and acetone for the cladding removal process and cleaning were procured from Fisher Scientific, India. All of the synthesis processes were carried out in double-distilled water. In a typical sensing procedure, the stock solutions of Urs in the proportion 1 mg/ml and urea were prepared in 0.1 M phosphate buffer of pH 7.4.

Synthesis of PANI-ZnO Nanocomposite Matrix

ZnO nanoparticles ∼26 nm in size were synthesized by a co-precipitation method using zinc chloride (oxidant) and sodium hydroxide (1:2 ratio) as source material. PANI-ZnO nanocomposite was synthesized with an *in-situ* chemical oxidation polymerization method. Initially, 0.02 M aniline was dissolved in 100 ml double-distilled water and stirred until the solution became transparent. The as-synthesized ZnO nanoparticles (0.2 M) were poured into the aniline solution, followed by constant stirring for 30 min. Further, 1 M HCl was added into the mixture of aniline-ZnO for homogeneity. An already-prepared 100 ml of stock solution of $FeCl_3$ (0.05 M) was added dropwise into the aniline-ZnO mixture with constant stirring for 1 hour. The precipitate was further centrifuged and washed several times with distilled water before characterization.

Development of Sensing Element

Half a meter of multimode plastic-clad silica (PCS) optical fiber with a specified core/cladding diameters of 450/300 μm (750 μm in total) and attenuation of 3 dB/km was selected for preparation of the sensing element. In the middle, a ∼2-cm portion of the cladding was removed carefully with a surgical blade. The unclad core was cleaned with hydrofluoric (HF) acid, acetone, and distilled water, respectively. Both ends of the optical fiber were polished with silicon carbide and very fine polish papers optimize the numerical aperture and acceptance angle. SMA905 connectors were then connected to both ends of the optical fiber. In the process of cladding modification, *in-situ* deposition on the unclad portion of the optical fiber was achieved by submerging it in the PANI-ZnO reaction container for 15 min at room temperature. Coating by this technique allows control of the thickness of the modified cladding on the core via the treatment time. Further, the enzyme-Urs was immobilized over the hydrophobic modified PANI-ZnO matrix through a cross-linking technique via 1% glutarldehyde and provided physical and chemical stability of the bio-receptor material. After that, loosely bound Urs molecules were leached out under gentle washing with phosphate buffer, followed by half an hour of drying. An adequate concentration of Enzyme-Urs was chosen to provide higher enzyme loading with excellent optical response and high retention.

Characterization

The as-synthesized ZnO nanoparticles, PANI matrix, and PANI-ZnO nanocomposites were characterized by different techniques. The structures of all synthesized materials were characterized by X-ray diffraction (XRD) and recorded on a Bruker AXS (D8 Advance, Germany) diffractometer in the scanning range 20–800 (2θ) using Cu Kα radiation with a wavelength of 1.5405 Å. Absorption spectrum studies of the materials were performed using a UV-Vis portable spectrometer (BLACK-Comet-SR, SL5-DH, Stellar Net, USA) with unpolarized light from temperature-controlled and intensity-stabilized deuterium and halogen lamps (UV-vis light source). The FTIR spectrum was recorded using an IR double beam spectrophotometer (8400S, Shimadzu, Japan) for the confirmation of functional groups in the prepared materials. The morphology of the prepared materials was studied by scanning electron microscopy (SEM) with a JEOL JSM-6360 (USA). The sensor parameters of the developed biosensor were analyzed by acquiring the absorbance spectrum by UV-Vis spectrophotometer, using an indigenously prepared sensing element connected between deuterium halogen lamps (UV-Vis light source) and the spectrophotometer. The sensing experiment was carried out in a completely dark environment to avoid interference from external light. Throughout the experiment, buffer solution (pH 7.4) was used. The sensing experimental setup shown in **Figure 1**. For the sensing parameters study, a 10 nM−1 M range of urea concentration in buffer solution was selected, with a 2-min exposure time for each concentration.

RESULTS AND DISCUSSION

Structural (XRD) and Morphological (SEM) Analysis

The structures of the incorporated ZnO nanoparticles, PANI, and PANI-ZnO nanocomposites were explored by XRD characterization, and the results are shown in **Figure 2**. The XRD pattern of the ZnO nanoparticles reveals that it is polycrystalline in nature. Their XRD pattern includes the (100), (002), (101), (102), (110), (103), (200), (112), and (201) diffraction peaks. All the observed diffraction peaks are in good agreement with ICDD pdf card No. 01-071-6424, which is for a hexagonal ZnO structure. The lattice constants of the prepared ZnO nanoparticles are found to be a = 3.249 Å, b = 3.249 Å, and c = 5.205 Å. The average crystallite size was determined by the standard Scherrer's formula and was found to be 26.06 nm. **Figure 2** shows the XRD pattern of PANI, which confirms its amorphous nature because of the absence of the characteristic peaks of the used oxidant (Kavitha et al., 2012). The XRD pattern of the ZnO-incorporating PANI matrix, also shown in **Figure 2**, provides confirmation to the formation of conducting organic–inorganic nanocomposites. The amorphous nature of PANI is affected by the incorporation of ZnO, and some characteristic peaks are observed because of the formation of hydrogen bonds between the H–N of PANI and the oxygen of ZnO. Thus, some of the peak shifts from the blue line of the PANI-ZnO matrix to the red and black lines may arise due to the interaction of ZnO nanoparticles (Deshpande et al., 2009). The

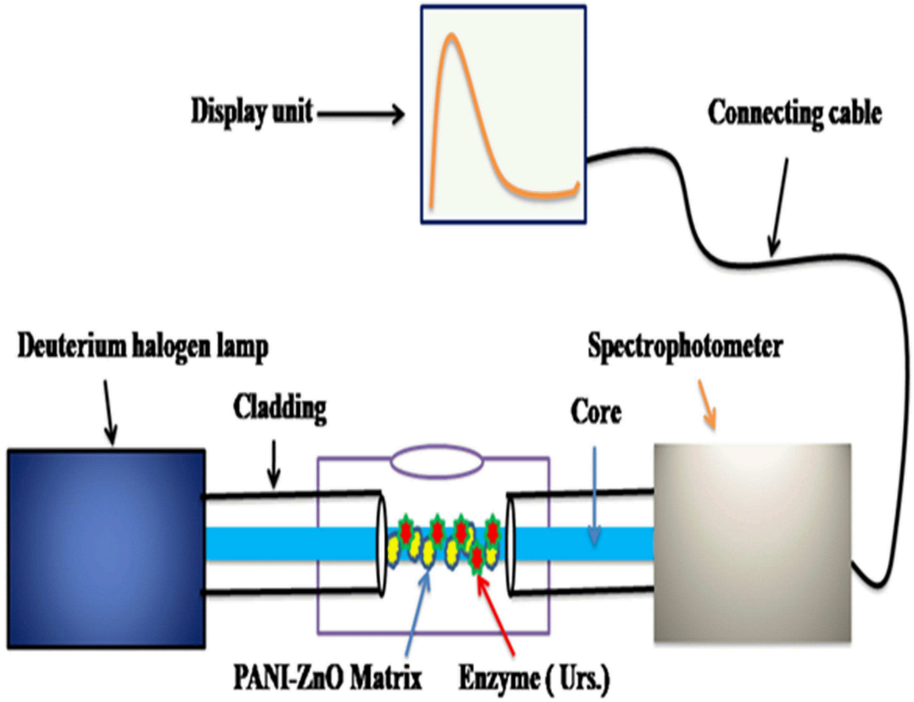

FIGURE 1 | Experimental set-up.

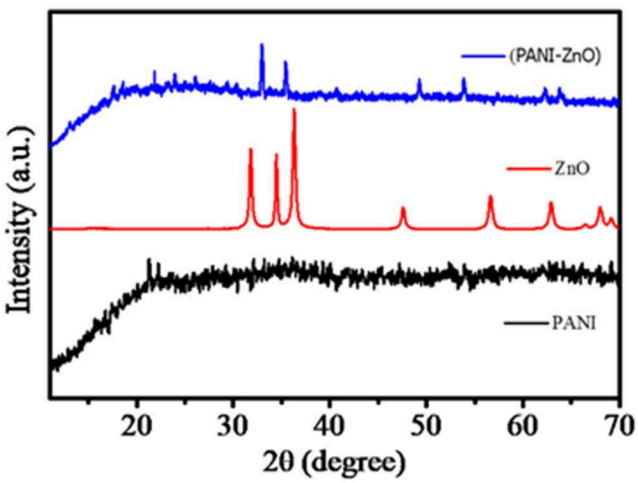

FIGURE 2 | XRD pattern of PANI, ZnO, and PANI-ZnO film.

repetition of benzenoid and quinoid rings in PANI chains and the low crystallinity of the PANI-ZnO nanocomposite shows that it is in a semiconducting state (Ali et al., 2015). Scherer's equation gives the crystalline size, D, of the PANI-ZnO nanocomposite as 33 nm.

Figure 3 shows SEM photographs of the PANI (**Figure 3A**) and PANI-ZnO (**Figure 3B**) films and reveals their morphological features. The amorphous nature and high agglomeration of pure PANI is clear in **Figure 3A**. The PANI-ZnO nanocomposite shows a cauliflower-like structure, comprising small globular particles, which is suitable for the immobilization of biomolecules. **Figure 3B** also shows that the PANI-ZnO nanocomposite has a porous morphology and is very efficient for enzyme-Urs immobilization. **Figure 3C** shows an SEM image of the cladding-modified region, confirming its uniform thickness on the nude core.

Spectroscopic Analysis

Optical Study (UV-Vis)

Optical spectroscopy provides information about the conducting states of PANI, i.e., the leucoemeraldine, pernigraniline, and emeraldine states. These states of PANI emerge from variation in the ratio of oxidant and monomer, the synthesis technique used, and the duration of the synthesis process. In biosensors, the emeraldine state of PANI is used due to this semiconducting state having better morphology (Kavitha et al., 2012).

In the present investigation, UV–visible absorption spectra of the as-synthesized PANI and PANI-ZnO nanocomposite were recorded and analyzed in the range 210–500 nm; these are shown in **Figure 4**. The absorption spectrum clearly reveals two characteristic absorption peaks at 233 and 287 nm for both PANI and PANI-ZnO nanocomposite. The observed peaks confirm that the emeraldine state of PANI is not modifies due to incorporation of ZnO within it. The observed peak at 233 may occur due to the presence of an aniline moiety (Babu et al., 2017), and the peak at 280 corresponds to the π-π^* transition of the benzenoid ring in polyaniline (Patil et al., 2015).

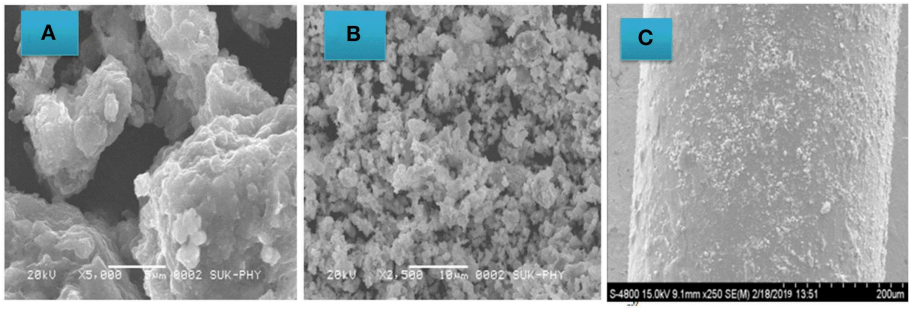

FIGURE 3 | Surface morphology of **(A)** PANI and **(B)** PANI-ZnO **(C)** Cladding modified sensing element.

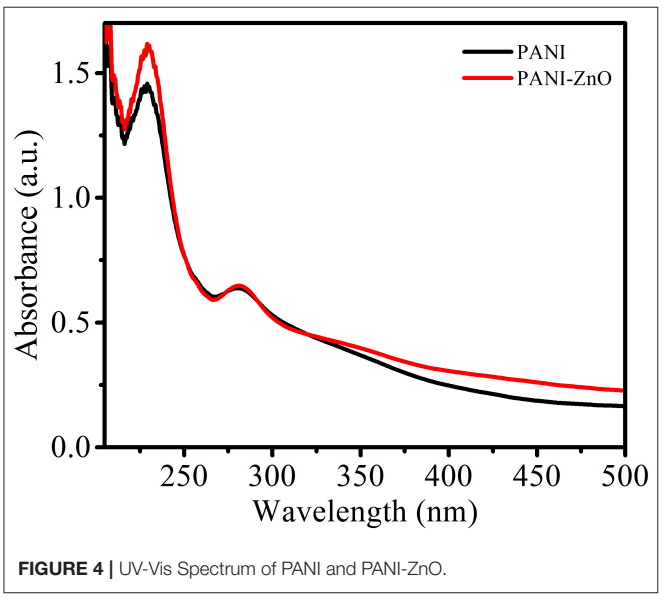

FIGURE 4 | UV-Vis Spectrum of PANI and PANI-ZnO.

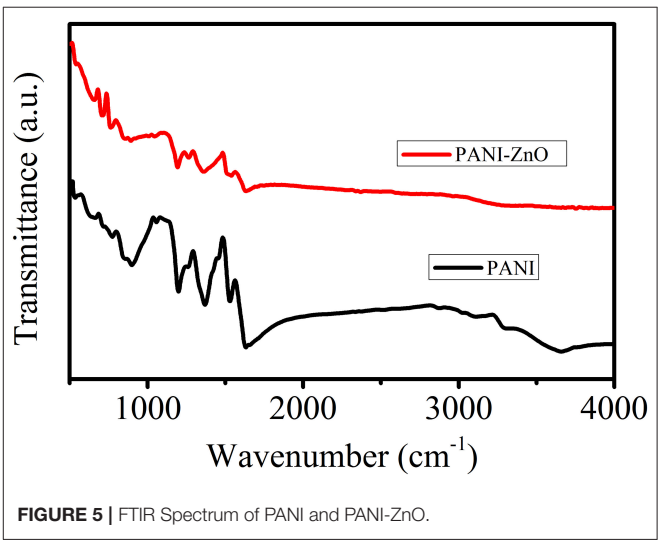

FIGURE 5 | FTIR Spectrum of PANI and PANI-ZnO.

Fourier Transform-Infrared (FTIR)

Pure PANI and PANI-ZnO nanocomposite were studied by FTIR spectroscopy, and the spectra are shown in **Figure 5**. All of the characteristic peaks of concern for the PANI and PANI-ZnO nanocomposite are exhibited. The FTIR spectra of PANI and PANI-ZnO nanocomposite show peaks within the range 643–761.21 cm^{-1} that are due to C–C bonding and aromatic C-H out-of-plane bending vibration. The peaks appearing at 1254.88 and 1269.65 cm^{-1} may be attributed to the C-N stretching of the secondary aromatic amine. The peaks at 1,364 and 1,287 cm^{-1} are assigned to asymmetric and symmetric stretching vibrations of the C=C ring. The peaks at 1358.65 and 1365.28 cm^{-1} correspond to C–N stretching and C–H bending in PANI and PANI-ZnO, respectively. The peaks at 1,412 and 1,462 cm^{-1} are attributed to C–H mixed vibrations and C–C stretch in the benzenoid ring, respectively. Because of the C=C stretching of the quinoid and benzenoid rings, a band originates at 1519.91 in both PANI and PANI-ZnO. Strong peak at 1638.16 cm^{-1} is attributed due to the C=C stretching mode of the quinoid rings results of both PANI and its composite with ZnO in emeraldine salt form (Deshpande et al., 2009; Kavitha et al., 2012). Distinct absorption peaks in PANI seen at 3657.92, 3289.42, and 3098.17 cm^{-1} are assigned to O-H stretching, N-H bending, and cross-linking moieties (Ali et al., 2015). The peaks around 3,855 cm^{-1} correspond to N-H band stretching vibration, and a broad peak appears at 3,747 cm^{-1} that can be associated with the interaction between ZnO nanoparticles and PANI, with hydrogen bonding occurring between H–N and the oxygen of ZnO (Patil et al., 2015). All of the characteristics bands of PANI are also found in the PANI-ZnO nanocomposite; however, some peaks are merged and decreased in intensity due to the incorporation of ZnO nanoparticles. This study confirms that the ZnO nanoparticles are properly incorporated into the PANI matrix.

SENSOR PERFORMANCE

The sensing parameters of the developed sensor viz. sensitivity, selectivity, stability, response time, and reusability were analyzed by studying the absorption spectrum in the evanescent wave field. The absorption spectrum of the developed sensor was studied in the wavelength range 246–256 nm.

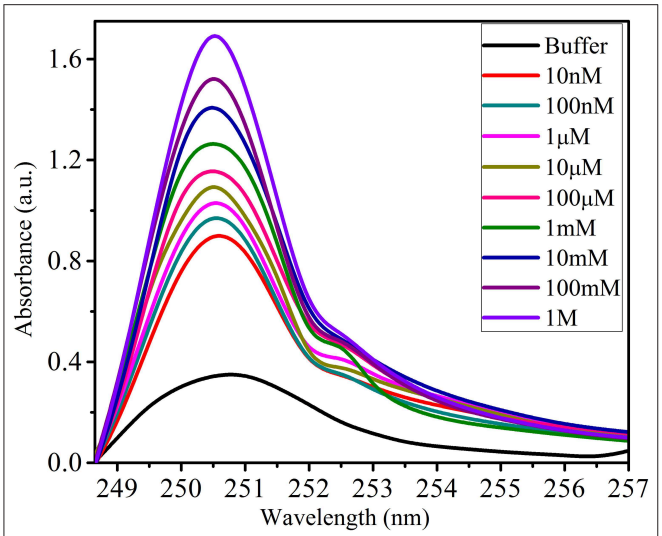

FIGURE 6 | Sensing response of developed biosensor.

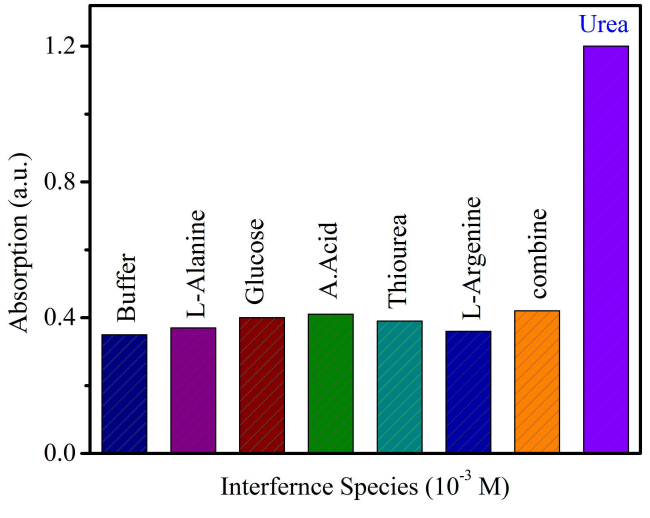

FIGURE 8 | Selectivity of developed biosensor.

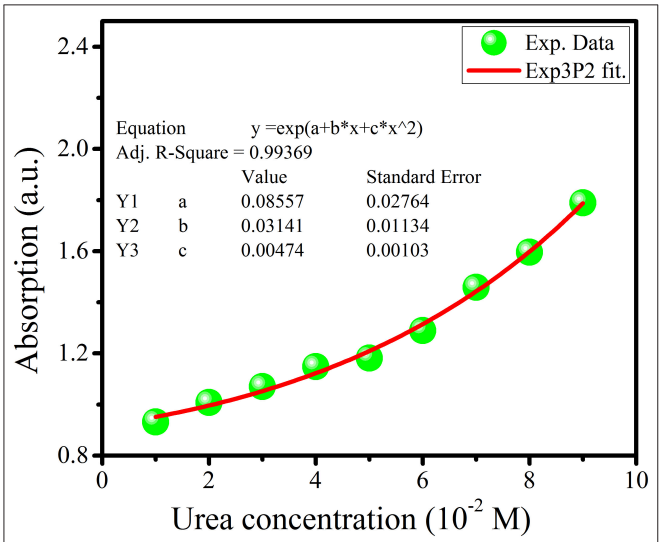

FIGURE 7 | Experimental data fitting.

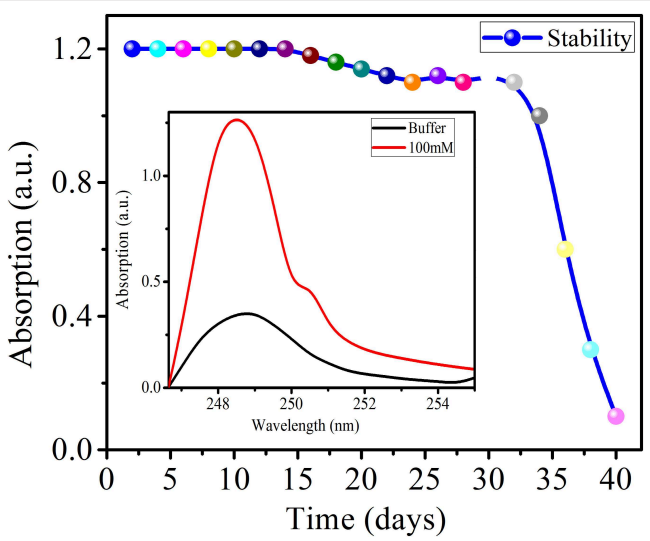

FIGURE 9 | Stability of developed biosensor.

Sensitivity

A urea concentration range from 10 nM to 1 M was used for the sensitivity study, and a 15-min incubation time was apportioned for each sample. Using the portable UV-Vis spectrophotometer, the absorption spectrum was obtained by connecting the sensing element between the light source and the spectrophotometer. The sensing response of the prepared sensor is depicted in **Figure 6** in the form of the absorption spectrum. The result obtained of sensitivity does not follow a linear function; instead, it follows an Exponential 3P2 function, as shown in **Figure 7**, with an Adj. R. Square value of 0.99369. To study the repeatability, the same conditions of the sensing element were maintained, such as the length of cladding removed, the deposition time of new cladding, the quantity of enzyme over the cladding-modified region, and the light source. Five sensors were developed, and each developed sensor showed approximately the same response toward urea.

The sensing mechanism of the developed sensor is discussed here briefly. Generally, for sensing the urea species, enzyme-Urs was used as a bioreceptor, which hydrolyzed the urea effectively with an approximate rate 1,014 times that of the non-catalyzed reaction (Kavitha et al., 2012). When the sensing element is exposed to a concentration of urea, the enzymatic reaction between urea and Urs occurs in two stages. Firstly, Urs react with urea to produce ammonia and carbamate, while in the second stage, the carbamate hydrolyzes to ammonia and carbonic acid in the following reaction (Kavitha et al., 2012).

$$NH_2CONH_2\ (urea) + 3H_2O \xrightarrow{urease} 2HCO_3^- + NH_4^+ + OH^- \ldots (1)$$

TABLE 1 | Comparison of other earlier urea sensors with that of the current study.

Immobilization matrix	Transducer	Detection technique	Detection limit	Linear range	Response time	Stability	References
ZnO nanowire	Gold-coated plastic substrates	Potentiometric	0.1 mM	0.1–40 mM	<4s	3 weeks	Usman Ali et al., 2011
ZnO nanorods	Ag sputtered glass substrate	Amperiometric	10 μM	0.001–24.0 mM	–	–	Ahmad et al., 2014
ZnO–MWCNT	Indium tin oxide coated glass slides	Cyclic voltammetry	0.23 mM	0.8–16.6 mM	4 s	>16 weeks	Tak et al., 2013
PANI grafted PAM–PVA membrane	Glassy carbon electrode	Impedance spectroscopy, differential pulse voltammetry	60 nM and 14 μM	1.5–1,000 μM	–	60 days	Das and Sarkar, 2016
PANI-ZnO matrix	Optical fiber	Absorption spectroscopy	10 nM	1 M−10 nM	45–50 s	40 days	Present work

This reaction is very beneficial for changing the microenvironment around the core, and it alters the optical properties of the modified cladding. The reaction rate and ammonia evolution from the reaction changes with change in the concentration of urea. Because of this, the refractive index of the modified cladding changes and causes this change in the intensity of the absorption spectrum. Moreover, the structural properties of the modified cladding may also change due to the effect of the reaction on the benzoid and quinoid segments of PANI-ZnO (in this study). The absorption peak at ∼250 nm seen in the sensitivity study may originate due to the immobilization of enzyme-Urs over the matrix and interaction with analyte urea. Thus, due to the alteration of the optical and structural properties of the modified cladding, the sensing response changes for each concentration of urea.

Selectivity Study

The specific selectivity toward urea for the developed sensor was studied by comparing its response to common interfering species generally found in living species. L-argenine, L- alanine, glucose, ascorbic acid, thiourea, and a combination of all of these species were used as interference species. A 100-mM solution of each interference species was prepared in buffer solution and used for the study of selectivity. **Figure 8** shows the response to the selected interfering species compared with that to urea. The absorption spectra for these species did not show any considerable response compared to that to urea, though slight variation occurred due to the refractive index of the surrounding solution. Thus, the prepared sensor is highly selective toward urea compared with the selected interference species.

Stability

The practical applicability of a sensor depends on its high sensitivity along with specific selectivity, repeatability, and stability. The stability study of the developed sensor was carried out for 52 days until there was negligible response. A 100-mM urea concentration in buffer solution was made freshly for each measurement. The stability graph is shown in **Figure 9**.

The precaution was taken of storing it at a temperature of 40°C after each day of measurement. The sensor demonstrated a stable response for 40 days and decreased slowly after that up to 52 days. The decreased response of the prepared sensor toward urea may be due to loss of the reactivity of the enzyme. The 40-day stability of the prepared sensor makes it very useful for practical applications.

Response Time and Detection Limit

Rapid response is an important feature of a sensor, and in the present study, response time was determined by considering the saturated intensity of the absorption spectrum. The developed sensor achieved a maximum saturated absorption intensity at ∼45–50 s, and this was considered as the response time of the sensor. The developed sensor showed a considerable response to a 10 nM urea concentration compared to buffer solution. Thus, for the developed sensor, we consider the response time to be ∼45–50 s and the lower limit of detection to be 10 nM.

Some earlier studies are compared with the present study in **Table 1**.

CONCLUSION

In the present report, we have successfully developed a cladding-modified intrinsic optical fiber urea sensor using PANI-ZnO as a modified cladding matrix. The properties of the PANI-ZnO matrix were explored by various characterization techniques, viz. XRD, UV-Vis, FTIR, and SEM. The developed sensor does not show a linear response but rather an exponential response toward urea concentration in the range 10 nM−1 M, with specific selectivity. The developed sensor exhibits a 10-nM lowest detection limit and a ∼45–50 s response time. The stable lifetime of the sensor was found to be 40 days when stored at 4°C after each measurement. According to the study of the sensor response, the PANI-ZnO matrix is a suitable and ideal candidate for cladding modification in an optical sensor as well as for enzyme immobilization. Lastly, we concluded that the developed sensor is efficient and useful for practical application in

biomedical industries for the detection of urea due to its features of high sensitivity, specific selectivity, stability, and low detection limit.

DATA AVAILABILITY STATEMENT

All datasets generated for this study are included in the article/supplementary material.

AUTHOR CONTRIBUTIONS

SB and VP performed experimental work and drafted the manuscript. DG and GB helped in the experiment, manuscript writing, and elucidate characterization of XRD, UV-Vis. FTIR etc. GM, MS, and PP guided for experimental work and reviewed manuscript. All authors contributed to the article and approved the submitted version.

REFERENCES

Ahmad, R., and Tripathy, N., and Hahn, Y.-B. (2014). Highly stable urea sensor based on ZnO nanorods directly grown on Ag/glass electrodes. *Sensors Actuators B Chem.* 194, 290–295. doi: 10.1016/j.snb.2013.12.098

Ahmad, R., Tripathy, N., Jang, N. K., Khang, G., and Hahn, Y. B. (2015). Fabrication of highly sensitive uric acid biosensor based on directly grown ZnO nanosheets on electrode surface. *Sensors Actuators B Chem.* 206, 146–151. doi: 10.1016/j.snb.2014.09.026

Ali, A., Israr-Qadir, M., Wazir, Z., Tufail, M., Ibupoto, Z. H., Jamil-Rana, S. A., et al. (2015). Cobalt oxide magnetic nanoparticles–chitosan nanocomposite based electrochemical urea biosensor. *Indian J. Phys.* 89, 331–336. doi: 10.1007/s12648-014-0594-3

Babu, K. J., Senthil kumar, N., and Kim, A. R. (2017). Freestanding and binder free PVdF-HFP/Ni-Co nanofiber membrane as a versatile platform for the electrocatalytic oxidation and non-enzymatic detection of urea. *Sensors Actuators B Chem.* 241, 541–551. doi: 10.1016/j.snb.2016.10.069

Banica, F. G. (2012). *Chemical Sensors and Biosensors: Fundamentals and Applications*. Chichester: John Wiley & Sons.

Bharadwaj, R., Sai, V. V. R., Thakare, K., Dhawangale, A., Kundu, T., Titus, S., et al. (2011). Evanescent wave absorbance based fiber optic biosensor for label-free detection of *E. coli* at 280 nm wavelength. *Biosens. Bioelectron.* 26, 3367–3370. doi: 10.1016/j.bios.2010.12.014

Botewad, S. N., Pahurkar, V. G., and Muley, G. G. (2018). Fabrication and evaluation of evanescent wave absorption based polyaniline-cladding modified fiber optic urea biosensor. *Optical Fiber Technol.* 40, 8–12. doi: 10.1016/j.yofte.2017.11.002

Das, J., and Sarkar, P. (2016). Enzymatic electrochemical biosensor for urea with a polyaniline grafted conducting hydrogel composite modified electrode. *RSC Adv.* 6:92520. doi: 10.1039/C6RA12159D

Deshpande, N. G., Gudage, Y. G., Sharma, R., Vyas, J. C., Kim, J. B., and Lee, Y. P. (2009). Studies on tin oxide-intercalated polyaniline nanocomposite for ammonia gas sensing applications. *Sensors Actuators B Chem.* 138, 76–84. doi: 10.1016/j.snb.2009.02.012

Dhawan, G., Sumana, G., and Malhotra, B. D. (2009). Recent developments in urea biosensors. *Biochem. Eng. J.* 44, 42–52. doi: 10.1016/j.bej.2008.07.004

Fan, X., White, I. M., Shopova, S. I., Zhu, H., Suter, J. D., and Sun, Y. (2008). Sensitive optical biosensors for unlabeled targets. A review. *Anal. Chim. Acta* 620, 8–26. doi: 10.1016/j.aca.2008.05.022

Iadicicco, A., Paladino, D., Campopiano, S., Bock, W. J., Cutolo, A., and Cusano, A. (2011). Evanescent wave sensor based on permanently bent single mode optical fiber. *Sensors Actuators B Chem.* 155, 903–908. doi: 10.1016/j.snb.2011.01.021

Kavitha, B., Prabakar, K., Siva, K., Srinivasu, D., Srinivas, C., Aswal, V. K., et al. (2012). Spectroscopic studies of nano size crystalline conducting polyaniline. *IOSR J. Appl. Chem.* 2,16–19. doi: 10.9790/5736-0211619

Kim, H. J., Park, S. H., and Park, H. J. (2010). Synthesis of a new electrically conducting nanosized Ag–polyaniline–silica complex using γ-radiolysis and its biosensing application. *Radiat. Phys. Chem.* 79, 894–899. doi: 10.1016/j.radphyschem.2010.02.005

Luong, J. H., Bouvrette, P., and Male, K. B. (1997). Developments and applications of biosensors in food analysis. *Trends Biotechnol.* 15, 369–377. doi: 10.1016/S0167-7799(97)01071-8

Martins, T. D., Ribeiro, A. C. C., de Camargo, H. S., da Costa Filho, P. A., Cavalcante, H. P. M., and Dias, D. L. (2013). "New insights on optical biosensors: techniques, construction and application," in *State of the Art in Biosensors—General Aspects*, ed T. Rinken (Rijeka: InTech), 112–139.

Mehrotra, P. (2016). Biosensors and their applications–a review. *J. Oral Biol. Craniofacial Res.* 6, 153–159. doi: 10.1016/j.jobcr.2015.12.002

Monk, D. J., and Walt, D. R. (2004). Optical fiber-based biosensors. *Anal. Bioanal. Chem.* 379, 931–945. doi: 10.1007/s00216-004-2650-x

Monošík, R., Stredanský, M., and Šturdík, E. (2012). Biosensors-classification, characterization and new trends. *ActaChimicaSlovaca* 5, 109–120. doi: 10.2478/v10188-012-0017-z

Mostafaei, A., and Ashkan, Z. (2012). Synthesis and characterization of conducting polyaniline nanocomposites containing ZnO nanorods. *Progress Nat. Sci. Mater. Int.* 22, 273–280. doi: 10.1016/j.pnsc.2012.07.002

Mostafaei, A., and Nasirpouri, F. (2014). Epoxy/polyaniline–ZnOnanorods hybrid nanocomposite coatings: synthesis, characterization and corrosion protection performance of conducting paints. *Progress Organ. Coat.* 77, 146–159. doi: 10.1016/j.porgcoat.2013.08.015

Patil, P. T., Anwane, R. S., and Kondawar, S. B. (2015). Development of electrospun polyaniline/ZnO composite nanofibers for LPG sensing. *Procedia Mater. Sci.* 10, 195–204. doi: 10.1016/j.mspro.2015.06.041

Prakash, S., Chakrabarty, T., Singh, A. K., and Shahi, V. K. (2013). Polymer thin films embedded with metal nanoparticles for electrochemical biosensors applications. *Biosens. Bioelectron.* 41, 43–53. doi: 10.1016/j.bios.2012.09.031

Ramakrishna, B., and Sai, V. V. R. (2016). Evanescent wave absorbance based U-bent fiber probe for immunobiosensor with gold nanoparticle labels. *Sensors Actuators B Chem.* 226, 184–190. doi: 10.1016/j.snb.2015.11.107

Rodriguez-Mozaz, S., de Alda, M. J. L., Marco, M. P., and Barceló, D. (2005). Biosensors for environmental monitoring: a global perspective.*Talanta* 65, 291–297. doi: 10.1016/S0039-9140(04)00381-9

Rossi, J. III, Ritchie, G. D., Nordholm, A. F., Knechtges, P. L., Wilson, C. L., Lin, J., et al. (2000). Application of neurobehavioral toxicology methods to the military deployment toxicology assessment program. *Drug Chem. Toxicol.* 23, 113–138. doi: 10.1081/DCT-100100106

Sai, V. V. R., Kundu, T., Deshmukh, C., Titus, S., Kumar, P., and Mukherji, S. (2010). Label-free fiber optic biosensor based on evanescent wave absorbance at 280 nm. *Sensors Actuators B Chem.* 143, 724–730. doi: 10.1016/j.snb.2009.10.021

Singh, M., Verma, N., Garg, A. K., and Redhu, N. (2008). Urea biosensors. *Sensors Actuators B Chem.* 134, 345–351. doi: 10.1016/j.snb.2008.04.025

Tahir, Z. M., Alocilja, E. C., and Grooms, D. L. (2005). Polyaniline synthesis and its biosensor application. *Biosens. Bioelectron.* 20, 1690–1695. doi: 10.1016/j.bios.2004.08.008

Tak, M., Gupta, V., and Tomar, M. (2013). Zinc oxide–multiwalled carbon nanotubes hybrid nanocomposite based urea biosensor. *J. Mater. Chem. B* 1:6392. doi: 10.1039/c3tb20935k

Terry, L. A., White, S. F., and Tigwell, L. J. (2005). The application of biosensors to fresh produce and the wider food industry. *J. Agric. Food Chem.* 53, 1309–1316. doi: 10.1021/jf040319t

Turner, A., Karube, I., and Wilson, G. S. (1987). *Biosensors: Fundamentals and Applications*. Oxford: Oxford University Press.

Usman Ali, S. M., Ibupoto, Z. H., Salman, S., Nur, O., Willander, M., and Danielsson, B. (2011). Selective determination of urea using urease immobilized on ZnO nanowires. *Sensors Actuators B* 160, 637–643. doi: 10.1016/j.snb.2011.08.041

Velasco-Garcia, M. N., and Mottram, T. (2003). Biosensor technology addressing agricultural problems. *Biosyst. Eng.* 84, 1–12. doi: 10.1016/S1537-5110(02)00236-2

Zawawi, M. A., O'Keffe, S., and Lewis, E. (2013). Intensity-modulated fiber optic sensor for health monitoring applications: a comparative review. *Sensor Rev.* 33, 57–67. doi: 10.1108/02602281311294351

Zhong, N., Zhao, M., Zhong, L., Liao, Q., Zhu, X., Luo, B., et al. (2016). A high-sensitivity fiber-optic evanescent wave sensor with a three-layer structure composed of Canada balsam doped with GeO_2. *Biosens. Bioelectron.* 85, 876–882. doi: 10.1016/j.bios.2016.06.002

Conflict of Interest: The authors declare that the research was conducted in the absence of any commercial or financial relationships that could be construed as a potential conflict of interest.

frontiers in Materials

ORIGINAL RESEARCH
published: 30 October 2020
doi: 10.3389/fmats.2020.520630

Martensitic Transition, Magnetic, Microstructural and Exchange Bias Properties of Melt Spun Ribbons of Mn-Ni-Sn Shape Memory Heusler Alloy

Jyoti Sharma[1]*, *K. G. Suresh*[2], *M. Manivel Raja*[3] and *Pravin Walke*[1]

[1]National Centre for Nanosciences and Nanotechnology, University of Mumbai, Mumbai, India, [2]Department of Physics, Indian Institute of Technology Bombay, Mumbai, India, [3]Defence Metallurgical Research Laboratory, Hyderabad, India

In the present report, we have studied the structural, microstructural, magnetic, exchange bias (EB) properties and magnetoresistance (MR) in Mn rich (Mn at. ~50%) $Mn_{50}Ni_{50-x}Sn_x$ (x = 10) shape memory Heusler alloy ribbons, prepared using the melt spinning method. These ribbons were found to exhibit a first order structural (i.e., martensitic) transition at around 205 K from the high temperature austenite to the low temperature martensite phase. The martensitic transition occurs at comparatively lower temperatures in these ribbons than in the same bulk alloy. Curie temperature of the austenite phase (T_C^A) is found to be larger i.e., around room temperature than that of bulk alloy. A significant EB field (H_{EB}) of around 960 Oe has been observed at 2 K for these ribbons, which is found to be comparable to that reported for other Heusler systems. The presence of the EB effect in these ribbons is attributed to the coexistence of FM/AFM exchange interactions in the martensite phase. They are also found to show a maximum negative MR of around 12% near the martensitic transition, for 50 kOe field change. Investigation of DC magnetization, AC susceptibility measurements and the observation of training effect (i.e., characteristic feature of EB) strongly corroborates with the coexistence of FM/AFM exchange interactions in the martensite phase of these ribbons, which results in the large EB. The effects of temperature and magnetic field on the EB properties and MR have also been studied here.

Keywords: martensitic transition, exchange bias effect, magnetoresistance, ferromagnetic shape memory alloys, heusler alloys

OPEN ACCESS

Edited by:
Bhaskar R. Sathe,
Dr. Babasaheb Ambedkar Marathwada University, India

Reviewed by:
Dattatray Late,
National Chemical Laboratory (CSIR), India
Sanjay Singh,
Indian Institute of Technology (BHU), India

***Correspondence:**
Jyoti Sharma
jsharma628@gmail.com

Specialty section:
This article was submitted to Smart Materials, a section of the journal Frontiers in Materials

Received: *16 December 2019*
Accepted: *09 September 2020*
Published: *30 October 2020*

Citation:
Sharma J, Suresh KG, Raja MM and Walke P (2020) Martensitic Transition, Magnetic, Microstructural and Exchange Bias Properties of Melt Spun Ribbons of Mn-Ni-Sn Shape Memory Heusler Alloy. Front. Mater. 11:520630. doi: 10.3389/fmats.2020.520630

INTRODUCTION

In recent years, Ni rich (Ni at. ~50%) Ni-Mn-Z (Z = Ga, Sb, In, and Sn) shape memory full Heusler alloys have attracted a lot of attention within the research community, owing to their multifunctional properties such as large shape memory effect, exchange bias (EB), giant magnetoresistance and large magnetocaloric effect, etc. (Ullakko et al., 1996; Pasquale et al., 2005; Khan et al., 2007; Pathak et al., 2010). These properties have been exploited in various applications such as in shape memory devices, magnetic tunnel junctions, sensors, storage and spintronic devices, etc. (Meiklejohn and Bean, 1956; Parkin et al., 1999; Marioni et al., 2005; Wang et al., 2010; Graf et al., 2011). Most of these properties are found to be associated with their first order structural transition (i.e., the martensitic transition)

from the high temperature cubic austenite phase to the low temperature tetragonal/orthorhombic/monoclinic martensite phase. Meiklejohn and Bean in 1956 discovered the EB effect at the ferromagnetic (FM)/antiferromagnetic (AFM) interface between the Co particles as FM core embedded in the CoO as AFM shell (Meiklejohn and Bean, 1956). EB is seen to arise due to the unidirectional anisotropy created at the different kind of interfaces such as FM/AFM, AFM/ferrimagnetic, FM/spin glass (SG) or ferrimagnetic/SG, when the material is cooled in presence of magnetic field, to the low temperatures (Parkin et al., 1999; Khan et al., 2007; Sharma and Suresh, 2015b). EB can be described by the magnetic hysteresis (M–H) loop shifting along the magnetic field axis, when it is recorded after the field cooling (FC) process. It can be estimated from the quantity called the EB field (H_{EB})) (Meiklejohn and Bean, 1956), for example, a maximum H_{EB} of 248 Oe has been reported in Ni rich $Ni_{50}Mn_{25+x}Sb_{25-x}$, 377 Oe in $Ni_{50-x}Mn_{37+x}Sn_{13}$ Heusler alloy and 120 Oe in $Ni_{50}Mn_{50-x}In_x$ alloy at 5 K (Khan et al., 2007; Nayak et al., 2009; Pathak et al., 2009). In contrast to the Ni rich Heusler alloys, to date Mn rich (Mn at. ~50%) Mn-Ni-Z (Z = Ga, In and Sn) shape memory Heusler alloys have been extensively studied mostly in bulk form (Xuan et al., 2010; Bachaga et al., 2015; Sharma and Suresh, 2015a; Sharma et al., 2019). The melt spinning method is seen as an effective tool to prepare the polycrystalline samples of these alloys with higher homogeneity, very refined, reduced sized and highly textured microstructure, which may result in the enhancement of various physical properties as discussed above. In literature, there are many reports available on martensitic transition, magnetic, structural, microstructural, magnetocaloric and EB properties of Ni rich Ni-Mn-Z (Z = Ga, Sb, In, and Sn) Heusler alloys ribbons (Llamazares Sánchez et al., 2013; Wang et al., 2013; Zhao G. X. et al., 2013; Maziarz et al., 2014; Chen et al., 2015; Huu et al., 2015; Louidi et al., 2018). However, Mn rich Heusler alloys in their melt spun ribbon form have not been extensively studied so far.

It is reported in literature that the magnetic properties of these shape memory Heusler alloys strongly depend upon the Mn-Mn exchange interactions. In Mn rich full Heusler alloys, excess Mn atoms have been found to occupy not only the Z sites but also the Ni sites in the lattice, which generally couple antiferromagnetically with Mn atoms at the regular sites (Wijn, 1988; Xuan et al., 2010). At the same time, the first order martensitic transition further leads to the decrease in the distance between Mn atoms at regular sites and the Mn atoms at neighboring sites (i.e., at Ni and Z sites) due to the twinning of the martensite phase variants, which further leads to the enhancement of AFM coupling in the system. Excess of Mn content in the Mn-Ni-Z alloys is thought to be responsible for the differences in physical properties observed between Mn rich and Ni rich Heusler alloys, as mostly the Mn content contributed to the magnetism of these alloys. In the present report, we have investigated the martensitic transition, magnetic, structural, microstructural, EB properties and magnetoresistance in Mn rich $Mn_{50}Ni_{50-x}Sn_x$ (x = 10) Heusler alloy melt spun ribbons.

EXPERIMENTAL CHARACTERIZATION

A polycrystalline sample of the presented $Mn_{50}Ni_{50-x}Sn_x$ (x = 10) Heusler alloy was prepared by arc melting method in the presence of highly pure argon atmosphere, by taking the stoichiometric amount of high purity elements such as Mn, Ni, and Sn. The sample was melted several times to get the homogeneity. The weight loss after melting was found to be less than 1%. After melting, the sample was annealed at 1073 K for 72 h in a sealed quartz tube, and subsequently quenched in liquid nitrogen in order to achieve better homogeneity. After that the annealed sample was taken in a quartz tube (i.e., of 1 mm diameter nozzle), and melted in the induction furnace in presence of highly pure argon atmosphere. Following this, the molten alloy was ejected through the nozzle onto a rotating wheel (made up of Cu) and made to cool rapidly, which gave the melt spun ribbons. The ejection rate of the ribbons can be changed by changing the argon gas pressure accordingly. A typical arrangement for the melt spinning process is shown in the **Figure 1**. The structural analysis for these melt spun ribbons is performed by collecting the X-ray diffraction pattern at room temperature (RT) using a PANalytical X'pert PRO diffractometer. The qualitative and the quantitative microstructural analyses were performed by scanning electron microscopy (ESEM-FEI quanta 200 model) and energy dispersive spectroscopy (EDS arrangement attached with ESEM) respectively. The magnetization measurements have been performed by using a superconducting quantum interference device magnetometer (SQUID) (Quantum Design). Magnetization as a function of temperature was recorded in zero (ZFC), FC and field heating (FH) modes. In all these modes, the sample was cooled down to 2 K from 400 K. The resistivity measurements were carried out in a vibrating sample magnetometer attached with the physical property measurement system using a four probe method.

RESULTS AND DISCUSSION

Structural and Microstructural Analysis

Figure 2 shows the RT XRD pattern for $Mn_{50}Ni_{50-x}Sn_x$ (x = 10) Heusler alloy melt spun ribbons. From the refinement (using Fullproof software), it is found that these ribbons exhibit the cubic structure at RT, with the estimated lattice parameter (a = b = c) of around 5.99 Å. The lattice parameters for ribbons are found to be almost the same as that for the same bulk sample (a = b = c = ~6.00 Å), which suggests that average size of the crystallites will be nearly the same in both of the samples. The absence of (111) peak in the XRD pattern suggests that there may be disorder present in these ribbons (Graf et al., 2011). The observation of cubic structure at RT (i.e. the austenite phase structure) indicates that their martensitic transition lies below RT. Generally the structure of the Heusler alloys is made up of four interpenetrating fcc lattices, which have the Wyckoff positions namely 4a(0,0,0), 4b(1/2,1/2,1/2), 4c(1/4,1/4,1/4) and 4d(3/4,3/4, 3/4) (Graf et al., 2011). The preferred site occupancy of 3d elements in Ni-Mn based Heusler alloys is decided by their number of valence electrons, such as the 3d elements having more

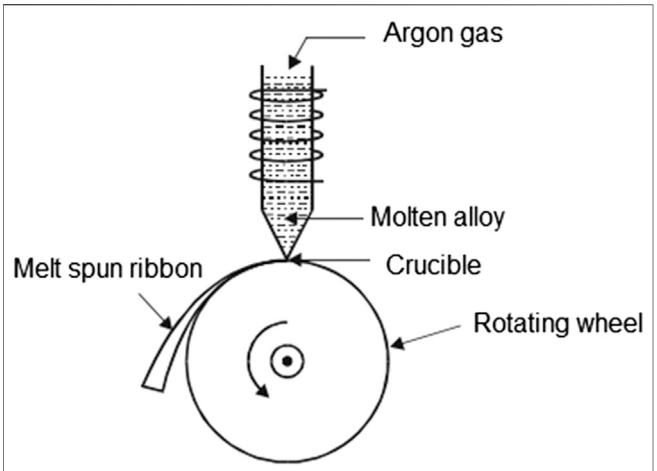

FIGURE 1 | A schematic diagram of the melt spinning method.

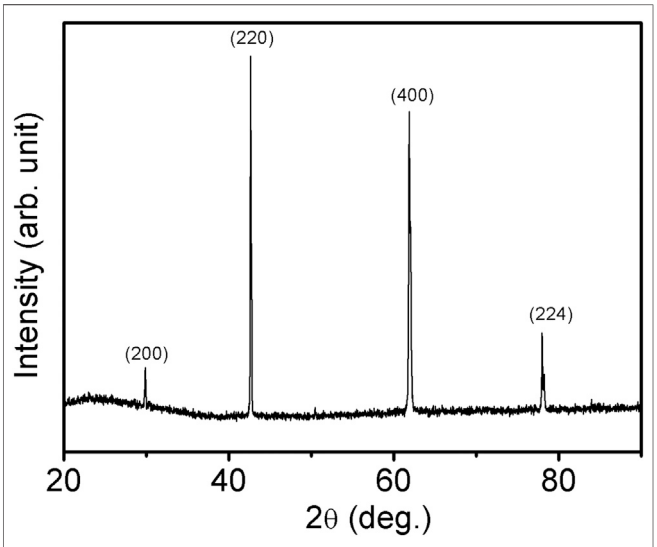

FIGURE 2 | Room temperature XRD pattern for the $Mn_{50}Ni_{50-x}Sn_x$ (x = 10) Heusler alloy melt spun ribbons.

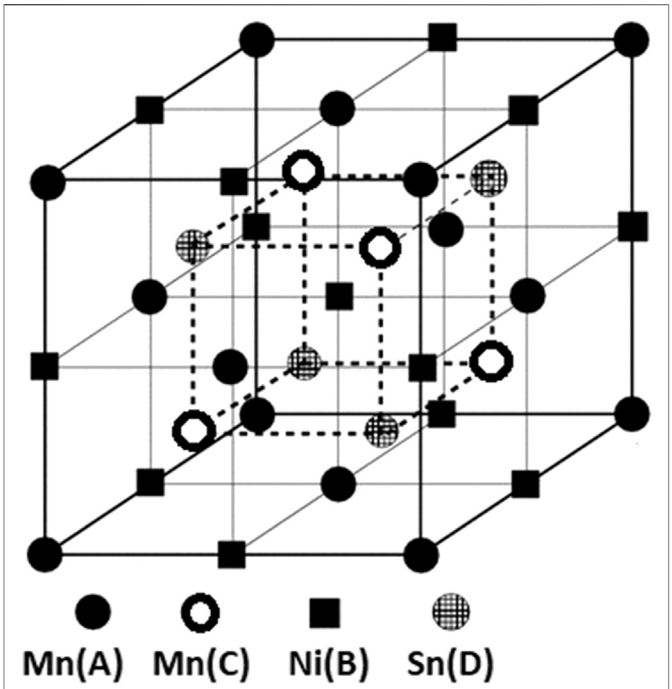

FIGURE 3 | A schematic cubic unit cell comprising of four interpenetrating fcc lattices, along with the expected site occupancies of different atoms.

valence electrons than Mn, prefer to occupy the 4a and 4b sites, and the structure is called Cu_2MnAl (regular) type. On the other hand, the 3d elements, which have the lesser valence electrons than Mn, prefer to occupy the 4a and 4c sites, and structure is known as Hg_2CuTi (inverse Heusler) type (Graf et al., 2011). Therefore, for a better understanding, a schematic of the cubic unit cell of present Heusler ribbons along with the Wyckoff positions of different atoms is shown in **Figure 3**. In the present case, Mn atoms are expected to occupy the 4a(0, 0, 0) and 4c(1/4,1/4,1/4) sites, which are denoted as the regular Mn atoms i.e., Mn(A) and Mn(C) respectively. Whereas Ni atoms occupy the 4b(1/2,1/2,1/2) sites, and Sn atoms occupy the 4d(3/4,3/4, 3/4) sites, which are denoted as Ni(B) and Sn(D) respectively. Generally it is seen in literature that, in Mn rich Heusler alloys, excess Mn atoms randomly occupy the Sn sites as well as the Ni sites, which suggests the presence of disorder in these systems, and consequently affects their electronic and magnetic properties (Xuan et al., 2010; Graf et al., 2011). The estimated nearest and next nearest inter-atomic distances (i.e., $\sqrt{3}a/4$ and $a/2$ Å respectively) between the Mn atoms suggest that there would be coexistence of AFM and FM coupling in the present ribbons.

Figure 4A,B shows the RT SEM images for the present melt spun ribbons, recorded at different areas of its free surface. It can be seen from the figure that these ribbons show a coarse granular microstructure, which consist of multiple shape grains (such as small columnar grains and tree leafs-like grains). No elongated thin plates and strips corresponding to the martensitic twin variants have been found inside the grains, this again confirm that the martensitic phase lies below the RT for these ribbons, which is in agreement with the XRD results. The average size of the grains lie between around 1–5 μm, which can be attributed to the different grain growth dynamics as a result of rapid solidification process. EDS analysis has also been performed on these ribbons (figure is not shown here), which confirmed the homogeneous composition throughout the sample. The chemical composition for these ribbons is found to be $Mn_{48.78}Ni_{40.76}Sn_{10.46}$. Standard deviation in elemental chemical composition obtained from EDS analysis is around 1.22 at. % for Mn, 0.76 at. % for Ni and 0.46 at. % for Sn respectively.

DC Magnetization Measurements

Figure 5 shows the magnetization as a function of temperature (M-T) curves for present ribbons in ZFC, FC and FH modes, measured in presence of 1 kOe field. It can be seen from the figure that the ribbon undergoes a first order structural (i.e., called

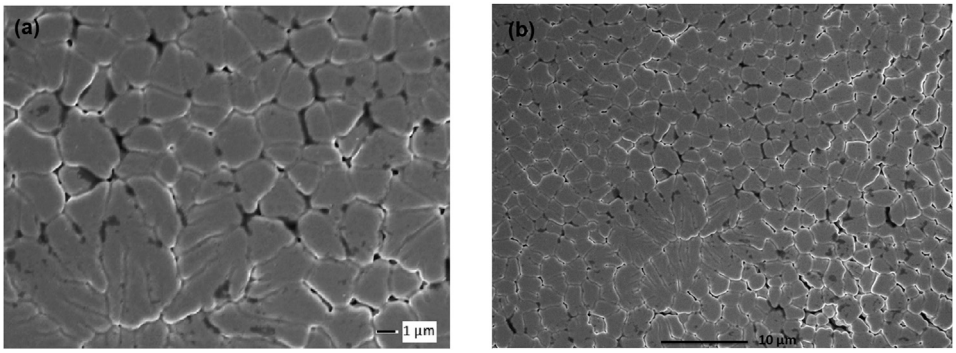

FIGURE 4 | (A,B) Room temperature SEM micrographs of these melt spun ribbons collected at different areas of its free surface.

martensitic) transition at around 205 K with a sudden increase in magnetization value (i.e., the maximum magnetization value), which corresponds to martensitic start temperature (M_s). It gets the minimum magnetization value at around 165 K, which corresponds to martensitic finish temperature (M_f). This corresponds to the forward martensitic transition. Similarly, we can notify the martensitic transition in terms of austenite start temperature (A_s) and the austenite finish temperature (A_f), as also marked in the **Figure 5**, that corresponds to the reverse martensitic transition. Curie temperature of austenite phase (T_C^A) occurs at around RT. As the temperature decreases below M_f, the magnetization starts to increase again, and ZFC, FC M-T curves show splitting at around 120 K. The ZFC curve shows a hump at around 66 K followed by that ZFC magnetization decreases with the further decrease in temperature down to 2 K. This splitting suggests the presence of the magnetic frustration at low temperatures in the martensite phase, which may be due to the presence of SG or coexistence of AFM/FM exchange interactions in these ribbons (Giri et al., 2011; Sharma and Suresh, 2015b). The first order nature of the martensitic transition is confirmed by the hysteresis observed between FC and FH M-T curves. The martensitic transition temperatures for these ribbons are found to be lower than that for the same bulk alloy, as M_s and M_f for the bulk composition are around 228 and 171 K respectively. Whereas T_C^A for the ribbons (i.e., around RT) is found to be higher than that for the bulk alloy (i.e., T_C^A = 278 K) (Sharma and Suresh, 2015a). The decrease in the martensitic transition temperatures for these ribbons comparative to the bulk composition may be attributed to the change in exchange interactions, as a result of the change in grain size after rapid solidification process. **Table 1** shows the better comparison of different martensitic transition temperatures observed in other Heusler alloys ribbons with the present case. One can see from the **Table 1** that the observed values of martensitic transition temperatures in the present case are in agreement with those obtained for other Heusler ribbons (Rama Rao et al., 2007; Maziarz et al., 2013; González-Legarreta et al., 2015).

To study the nature of the low temperature frustrated magnetic state of these ribbons, AC susceptibility as a function of temperature has been measured, at different frequencies

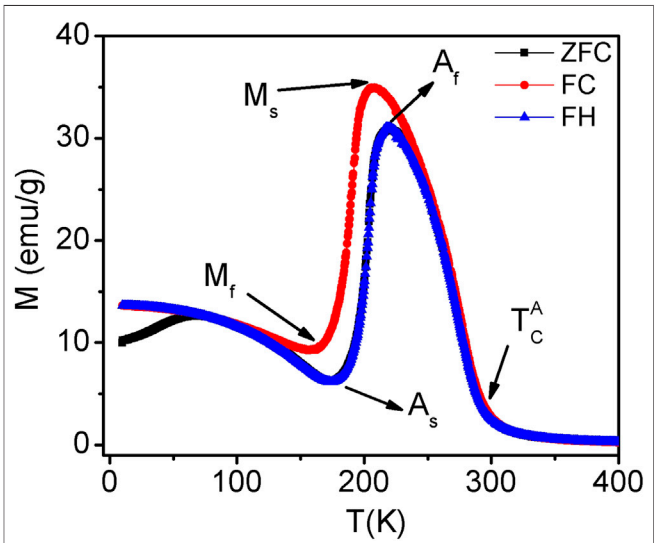

FIGURE 5 | The ZFC, FC and FH, magnetization as a function of temperature (M-T) curves measured at 1 kOe field.

ranging from 10 to 995 Hz, such as the data is shown in the **Figure 6**. It can be seen from the figure that at 10 Hz frequency, there is broad peak observed at around 150 K (marked as T_P in the figure), which occurs at a significantly higher temperature than that observed in DC M-T curve (**Figure 5**). A small frequency dependence of this peak at 250 Hz can be seen from the figure, but it is not measurable due to the broadness of the peak. Whereas for higher frequencies, there is no prominent frequency dependence observed for this peak, which rules out the possibility of a SG phase in these ribbons. Therefore the low temperature martensite phase is expected to consist of the mixed FM/AFM phases, which was expected and discussed earlier.

Exchange Bias Properties

As we have discussed from the DC magnetization and AC susceptibility measurements, there is a coexistence of FM/AFM phases in the martensite phase, which can lead to the EB effect. Therefore, to investigate the EB effect in the present ribbons, we

TABLE 1 | Comparison of various martensitic transition temperatures obtained for other Heusler alloys ribbons reported in literature with the present ribbons.

Alloy (composition)	M_s (K)	M_f (K)	$T_{A-M} = (M_s + M_f)/2$(K)	A_s (K)	A_f (K)	$T_{M-A} = (A_s + A_f)/2$ (K)	T_C^A (K)	Ref.
$Ni_{47}Mn_{41}In_{12}$	185	110	148	194	223	209	292	González-Legarreta et al. (2015)
$Ni_{53}Mn_{20.4}Ga_{26.6}$	185	178	182	190	198	194	306	Rama Rao et al. (2007)
$Ni_{48}Mn_{39.5}Sn_{12.5}$	—	—	242	—	—	258	300	Maziarz et al. (2013)
Present alloy	205	165	185	174	218	196	284	—

have collected the magnetic hysteresis (M-H) loop at 2 K in field range of ±20 kOe, after FC the sample in presence of 10 kOe. The M-H hysteresis loop at 2 K is shown in **Figure 7** in the field range of ±8 kOe for better visibility of M-H loop shifting. It is clear from the figure that the M-H loop completely shifts towards the negative field axis, which confirms the EB effect in these ribbons. A maximum value of exchange bias field (H_{EB}) of around 960 Oe has been estimated at 2 K, which is found to be comparable to that reported in other Heusler systems (Pathak et al., 2009; Xuan et al., 2010; Sahoo et al., 2013; Zhao G. X. et al., 2013; Zhao X. G. et al., 2013; Czaja et al., 2014; Sharma and Suresh, 2015a). The present ribbons are found to show improved EB as compared to the same bulk composition (as H_{EB} = 920 Oe) at the same temperature and cooling field conditions, which may be attributed the change in the strength of AFM/FM exchange interactions as a result of the change in Mn-Mn inter-atomic distances (Sharma and Suresh, 2015a). Similarly, the present ribbons also show the relatively larger EB than that observed in other related Heusler alloys ribbons, such as in $Ni_{50}Mn_{37}Sn_{13}$ ribbons (H_{EB} = ~225 Oe at 5 K), in $Ni_{45.5}Mn_{43.0}In_{11.5}$ ribbons (H_{EB} = 270 Oe at 5 K), in $Ni_{50}Mn_{38}Sn_{12}$ ribbons (H_{EB} = ~300 Oe at 5 K), in $Mn_{46}Ni_{42}Sn_{11}Sb_1$ ribbons (H_{EB} = 90 Oe at 50 K), and in $Mn_{50}Ni_{50-x}Sn_x$ (x = 11) Heusler ribbons (H_{EB} = ~213 Oe at 2 K) (Yang et al., 2012; Llamazares Sánchez et al., 2013; González-Legarreta et al., 2014; Huang et al., 2016; Sharma et al., 2020). The H_{EB} is calculated by using the formula $H_{EB} = -(H_1 + H_2)/2$, where the H_1 and H_2 are designated as the left and right coercive fields, where the magnetization vanishes. The presence of EB effect in these ribbons confirms the coexistence of FM/AFM phases at low temperatures in the martensite phase.

The training effect, which is a characteristic feature of EB, has also been investigated in the present ribbons. The training effect is defined by the decrease of EB field, when the field cooled M-H loop is repeated consecutively "n" (*n* = no. of cycles) times. To study the training effect, we have recorded M-H loops at 2 K in the consecutive field cycles (*n*), after FC the sample at 10 kOe (data not shown here). The estimated EB field, H_{EB} from these consecutive M-H loops at 2 K is shown in the inset of **Figure 7**, as a function of no. of cycles. It can be seen from the inset that H_{EB} is decreasing with the increase of *n*. This experimental data has been fitted to the simple power law (i.e., given by equation $H_{EB} - H_{EB\infty} \alpha 1/\sqrt{n}$, where $H_{EB\infty}$ is EB field in the asymptotic limit of *n*. It is clear from the inset that, our experimental data fits well with the simple power law (as shown by the solid line in the inset), and the estimated value of $H_{EB\infty}$ from the fit is around 946 Oe.

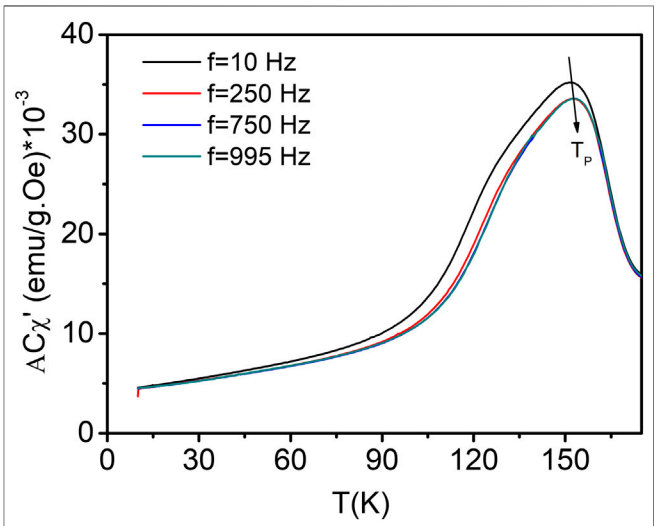

FIGURE 6 | Temperature dependence of the real part of AC susceptibility (χ′) measured at different frequencies for the present ribbons.

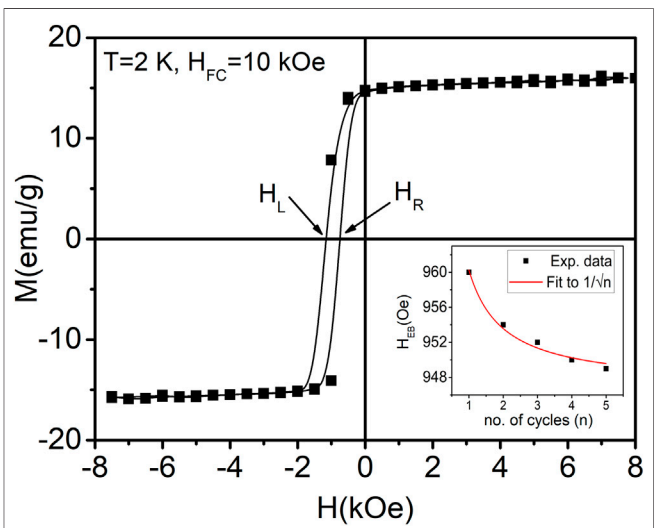

FIGURE 7 | EB effect: Magnetic hysteresis (M-H) loop measured at 2 K after field cooling process in presence of 10 kOe magnetic field. Inset shows the training effect of exchange bias observed in the present ribbons. Here solid squares show the experimental data and solid line shows the fit to simple power law ($H_{EB} - H_{EB\infty} \alpha 1/\sqrt{n}$).

Training effect is described by the fact that at the time of magnetization reversal in consecutive M-H loops, FM moments do not get reversed homogenously, which is attributed to the AFM moments rearrangement at the interfaces and this consequently results in the decrease of H_{EB} with increasing *n*.

To study the effect of temperature on EB properties, the magnetic hysteresis (M-H) loops have been recorded at different temperatures in a field range of ±20 kOe after the FC process in the presence of 10 kOe (data not shown here). The shifting of the M-H loop has been found to decrease with the increase of temperature, and vanishes at around 70 K, which corresponds to the EB blocking temperature (T_B), at which the AFM moments would not be able to pin the FM moments and consequently results in the zero EB field. The estimated value of the EB field from these M-H hysteresis loops as a function of temperature is shown in the **Figure 8**. The H_{EB} is found to decrease with increasing temperature, which may be attributed to the decrease in exchange coupling between the AFM/FM phases as a result of the increase in thermal energy. It can be noted that the present Heusler alloy ribbons show a large EB at the low temperatures, and retains the reasonable value upto around 40 K.

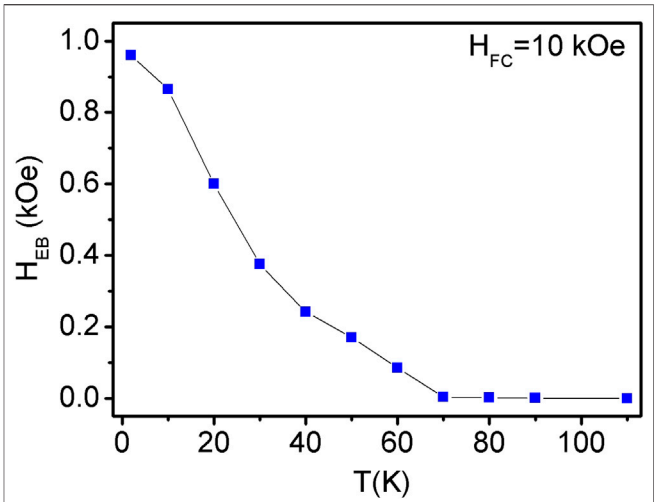

FIGURE 8 | Temperature dependence of the EB field (H_{EB}) estimated from the M-H loops recorded at different temperatures after field cooling at 10 kOe field.

Magnetoresistance

To shed more light onto the results obtained from the magnetization measurements near the first order martensitic transition of these ribbons, the electrical resistivity measurements have also been performed. The temperature dependence of resistivity (in heating and cooling modes) measured in presence of zero and 50 kOe field is shown in **Figure 9**. At higher temperatures i.e., in the austenite phase, ρ-T curves show a typical metallic behavior. As the temperature is lowered from 400 K, resistivity suddenly starts increasing and first order martensitic transition takes place. After reaching its maximum value, resistivity becomes almost constant with further lowering the temperature. The value of martensitic transition temperatures obtained from these ρ-T curves are in agreement with those obtained from the DC magnetization measurements (**Figure 5**). The hysteresis observed between the heating and cooling ρ-T curves again confirms the first order nature of the martensitic transition. It can be seen from the figure that with the application of magnetic field (50 kOe), the martensitic transition temperatures are found to decrease, which can be attributed to the fact that martensitic phase transformation gets hindered by the application of the magnetic field. At 50 kOe field, the austenite phase may not completely transform into the martensite phase i.e., the remaining phase gets kinetically arrested in the austenite state, which consequently leads to the shift in martensitic transition to lower temperature. The similar type of phenomenon i.e., kinetic arrest of the first-order martensitic transition from FM austenite phase to weakly magnetic/AFM phase has also been observed in many Heusler systems (Sharma et al., 2007; Xu et al., 2010). This implies that the application of magnetic field leads to the stabilization of the austenite phase in the present ribbons. To confirm the kinetic arrest behavior of the martensitic transition, the electrical resistivity as a function of magnetic field for the present ribbons has also been measured at

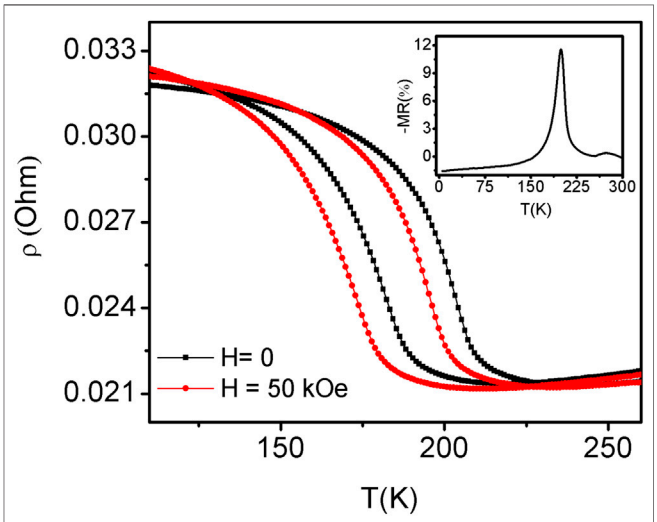

FIGURE 9 | Temperature as a function of resistivity (ρ), measured in zero and 50 kOe field. Inset shows the magnetoresistance (MR) as a function of temperature, calculated from these ρ-T curves.

various temperatures in the vicinity of martensitic transition (data not shown here). The results obtained from the $\rho(H)$ curves are found to be in agreement with those observed from $\rho(T)$ curves.

The magnetoresistance (i.e., the measure of change in resistivity with respect to the change in magnetic field) has also been calculated for the present ribbons using the resistivity data (**Figure 9**). MR (calculated by using the formula $(\rho(H) - \rho(0))/\rho(0) \times 100$) as a function of temperature for 50 kOe field change is shown in the inset of **Figure 9**. These ribbons are found to show a maximum negative MR of around 12% at 198 K for 50 kOe field change, which is comparable to that

obtained for other Heusler systems (Pathak et al., 2010; Sahoo et al., 2013). The observed MR in present ribbons is found to be larger as compared to that observed in the same bulk composition i.e., MR = −6.4% for same field change (Sharma et al., 2019). Similarly, a relative improvement in MR is also obtained in the present ribbons as compared to that observed in some other Heusler alloys ribbons, such as MR = −10% is obtained in Ni-Co-Mn-Sb as spun ribbons, and a maximum negative MR of 9% is obtained in Ni–Fe–Ga Heusler ribbons (Sahoo et al., 2013; Tolea et al., 2017). MR shows the maximum value near the martensitic transition temperature, as it arises due to the field induced nature of the first order martensitic transition.

SUMMARY

Here the first order martensitic transition, magnetic, structural, microstructural, EB properties and MR of $Mn_{50}Ni_{50-x}Sn_x$ (x = 10) shape memory Heusler alloy melt spun ribbons have been studied. These ribbons were prepared by melt spinning method. The RT structure is found to be cubic for these ribbons with the estimated lattice parameters (a = b = c) of 5.99 Å. They have been found to undergo a first order martensitic transition at around 205 K from the cubic austenite phase to the martensite phase, which is comparatively lower than that for the same bulk composition. This can be attributed to the change in strength of AFM/FM exchange interactions, as a result of the change in grain size during the melt spinning process. Curie temperature of the austenite phase (T_C^A) lies around RT. These ribbons show a significant EB effect with EB field of 960 Oe at 2 K, after FC in presence of 10 kOe, which is found to be relatively larger than that reported in some other Heusler systems. The H_{EB} decreases with the increase in temperature. The presence of EB in these melt spun ribbons can be attributed to the coexistence of FM/AFM exchange interactions in the martensite phase. DC magnetization, AC susceptibility measurements and the observation of training effect confirm the presence of coexistence of FM/AFM exchange interactions at low temperatures. They have also been found to show a maximum negative MR of 12% around the martensitic transition for 50 kOe field change. Resistivity measurements show that the application of a magnetic field leads to the stabilization of the austenite phase. Thus the present results suggest that the melt spinning may be used as an effective method of material preparation, so that various physical properties of Heusler alloys, such as the magnetic, magnetocaloric effect, EB and MR, etc. can be modified according to the fundamental research as well as from the application point of view.

DATA AVAILABILITY STATEMENT

The raw data supporting the conclusions of this article will be made available by the authors, without undue reservation, to any qualified researcher.

AUTHOR CONTRIBUTIONS

JS performed all the experiments shown in the manuscript. Melt spun ribbons were prepared at DMRL, hyderabad with the help of MR. JS discussed the results with KS and PW.

ACKNOWLEDGMENTS

Authors would like to acknowledge the SERB Govt. of India for the financial assistance granted through a national post doctoral fellowship (NPDF) project.

REFERENCES

Bachaga, T., Daly, R., Khitouni, M., Escoda, L., Saurinal, J., and Suño, J. J. (2015). Thermal and structural analysis of $Mn_{49.3}Ni_{43.7}Sn_{7.0}$ Heusler alloy ribbons. *Entropy* 17, 646–657. doi:10.3390/e17020646

Chen, X., Naik, B. V., Mahendiran, R., and Ramanujan, V. R. (2015). Optimization of Ni–Co–Mn–Sn Heusler alloy composition for near room temperature magnetic cooling. *J. Alloys Compd.* 618, 187–191. doi:10.1016/j.jallcom.2014.08.032

Czaja, P., Maziarz, W., Przewoznik, J., Kapusta, C., Hawelek, L., Chrobak, A., et al. (2014). Magnetocaloric properties and exchange bias effect in Al for Sn substituted $Ni_{48}Mn_{39.5}Sn_{12.5}$ Heusler alloy ribbons. *J. Magn. Magn. Mater.* 358–359, 142–148. doi:10.1016/j.jmmm.2014.01.069

Giri, C. S., Patra, M., and Majumdar, S. (2011). Exchange bias effect in alloys and compounds. *J. Phys. Condens. Matter.* 23, 073201. doi:10.1088/0953-8984/23/7/073201

González-Legarreta, L., González-Alonso, D., Rosa, W. O., Caballero-Flores, R., Suñol, J. J., González, J., et al. (2015). Magnetostructural phase transition in off-stoichiometric Ni–Mn–In Heusler alloy ribbons with low in content. *J. Magn. Magn. Mater.* 383, 190–195. doi:10.1016/j.jmmm.2014.10.152

González-Legarreta, L., Rosa, O.W., García, J., Ipatov, M., and Hernando, B. (2014). Annealing effect on the crystal structure and exchange bias in Heusler Ni45.5Mn43.0In11.5 alloy ribbons. *J. Alloys Compd.* 582, 588–593. doi:10.1016/j.jallcom.2013.08.078

Graf, T., Felser, C., and Parkin, S. S. P. (2011). Simple rules for the understanding of Heusler compounds. *Prog. Solid State Ch.* 39, 1–50. doi:10.1016/j.progsolidstchem.2011.02.001

Huang, Q., Chen, F., Zhang, M., and Xu, X. (2016). Magnetoresistance and exchange bias in high Mn content melt-spun $Mn_{46}Ni_{42}Sn_{11}Sb_1$ alloy ribbon. *Chin. Phys. B.* 25, 057305. doi:10.1088/1674-1056/25/5/057305

Huu, D. T., Yen, N. H., Thanh, P. T., Mai, N. T., Thanh, T. D., Phan, T. L, et al. (2015). Magnetic, magnetocaloric and critical properties of $Ni_{50-x}Cu_xMn_{37}Sn_{13}$ rapidly quenched ribbons. *J. Alloys Compd.* 622, 535–540. doi:10.1016/j.jallcom.2014.10.126

Khan, M., Dubenko, I., Stadler, S., and Ali, N. (2007). Exchange bias in bulk Mn rich Ni–Mn–Sn Heusler alloys. *Appl. Phys. Lett.* 91, 072510. doi:10.1063/1.2818016

Llamazares Sánchez, L. J., Flores-Zúñiga, H., Ríos-Jara, D., Sánchez-Valdes, F. C., García-Fernández, T., Ross, A. C., et al. (2013). Structural and magnetic characterization of the intermartensitic phase transition in NiMnSn Heusler alloy ribbons. *J. Appl. Phys.* 113, 17A948. doi:10.1063/1.4800836

Louidi, S., Sunol, J. J., Ipatov, M., and Hernando, B. (2018). Effect of cobalt doping on martensitic transformations and the magnetic properties of $Ni_{50-x}Co_xMn_{37}Sn_{13}$ (x = 1, 2, 3) Heusler ribbons. *J. Alloys Compd.* 739, 305–310. doi:10.1016/j.jallcom.2017.12.280

Marioni, M. A., O'Handley, R. C., Allen, S. M., Hall, S. R., Paul, D. I., Richard, M. L., et al. (2005). The ferromagnetic shape-memory effect in Ni–Mn–Ga. *J. Magn. Magn. Mater.* 290, 35. doi:10.1016/j.jmmm.2004.11.156

Maziarz, W., Czaja, P., Szczerba, M. J., Przewoźnik, J., Kapusta, C., Żywczak, A., et al. (2013). Room temperature magneto-structural transition in Al for Sn substituted Ni–Mn–Sn melt spun ribbons. *J. Magn. Magn. Mater.* 348, 8–16. doi:10.1016/j.jmmm.2013.08.005

Maziarz, W., Czaja, P., Szczerba, M. J., Przewoźnik, J., Kapusta, C., Żywczak, A., et al. (2014). Surface topography, microstructure and magnetic domains in Al for Sn substituted metamagnetic Ni-Mn-Sn Heusler alloy ribbons. *Intermetallics* 55, 1–8. doi:10.1016/j.intermet.2014.07.001

Meiklejohn, W. H., and Bean, C. P. (1956). New magnetic anisotropy. *Phys. Rev.* 102, 1413. doi:10.1103/PhysRev.102.1413

Nayak, A. K., Suresh, K. G., and Nigam, A. K. (2009), Observation of enhanced exchange bias behaviour in NiCoMnSb Heusler alloys. *J. Phys. D: Appl. Phys.* 42, 115004. doi:10.1088/0022-3727/42/11/115004

Parkin, S. S. P., Roche, K. P., Samant, M. G., Rice, P. M., Beyers, R. B., Scheuerlein, R. E., et al. (1999). Exchange-biased magnetic tunnel junctions and application to nonvolatile magnetic random access memory (invited). *J. Appl. Phys.* 85, 5828. doi:10.1063/1.369932

Pasquale, M., Sasso, C. P., Lewis, L. H., Giudici, L., Lograsso, T., and Schlagel, D. (2005). Magnetostructural transition and magnetocaloric effect in $Ni_{55}Mn_{20}Ga_{25}$ single crystals. *Phys. Rev. B* 72, 094435. doi:10.1103/PhysRevB.72.094435

Pathak, A. K., Dubenko, I., Pueblo, C., Stadler, S., and Ali, N. (2010). Magnetoresistance and magnetocaloric effect at a structural phase transition from a paramagnetic martensitic state to a paramagnetic austenitic state in $Ni_{50}Mn_{36.5}In_{13.5}$ Heusler alloys. *Appl. Phys. Lett.* 96, 172503. doi:10.1063/1.3422483

Pathak, A. K., Khan, M., Gautam, B. R., Stadler, S., Dubenko, I., and Ali, N. (2009). Exchange bias in bulk Ni–Mn–In-based Heusler alloys. *J. Magn. Magn. Mater.* 321, 963–965. doi:10.1016/j.jmmm.2008.03.008

Rama Rao, N. V., Gopalan, R., Manivel Raja, M., Chelvane, J. A., Majumdar, B., and Chandrasekaran, V. (2007). Magneto-structural transformation studies in melt-spun Ni–Mn–Ga ribbons. *Scr. Mater.* 56, 405–408. doi:10.1016/j.scriptamat.2006.10.037

Sahoo, R., Raj Kumar, M. D., Babu, A. D., Suresh, G. K., Nigam, K. A., and Raja, M. M. (2013). Effect of annealing on the magnetic, magnetocaloric and magnetoresistance properties of Ni-Co-Mn-Sb melt spun ribbons. *J. Magn. Magn. Mater.* 347, 95–100. doi:10.1016/j.jmmm.2013.07.027

Sharma, J., Coelho, A. A., Repaka, D. V. M., Ramanujan, R. V., and Suresh, K. G. (2019). Pressure induced martensitic transition, magnetocaloric and magneto-transport properties in Mn-Ni-Sn Heusler alloy. *J. Magn. Magn. Mater.* 487, 165307. doi:10.1016/j.jmmm.2019.165307

Sharma, J., Nag, J., Suresh, G. K., Manivel Raja, M., and Walke, P. (2020). Martensitic transition, magnetic and exchange bias properties in Mn rich Heusler alloy ribbons. *AIP Conf. Proc.* 2220, 110021. doi:10.1063/5.0001389

Sharma, J., and Suresh, K. G. (2015a). Investigation of multifunctional properties of $Mn_{50}Ni_{40-x}Co_xSn_{10}$ (x=0–6) Heusler alloys. *J. Alloys Compd.* 620, 329–336. doi:10.1016/j.jallcom.2014.09.141

Sharma, J., and Suresh, K. G. (2015b). Observation of giant exchange bias in bulk $Mn_{50}Ni_{42}Sn_8$ Heusler alloy. *Appl. Phys. Lett.* 106, 072405. doi:10.1063/1.4913268

Sharma, V. K., Chattopadhyay, M. K., and Roy, S. B. (2007). Kinetic arrest of the first order austenite to martensite phase transition in $Ni_{50}Mn_{34}In_{16}$: dc magnetization studies. *Phys. Rev. B.* 76, 140401. doi:10.1103/PhysRevB.76.140401

Tolea, F., Tolea, M., Sofronie, M., Popescu, B., Crisan, A., Leca, A., et al. (2017). Specific changes in the magnetoresistance of Ni–Fe–Ga Heusler alloys induced by Cu, Co, and Al substitutions. *IEEE Trans. Magn.* 53 (4), 1–7. doi:10.1109/TMAG.2016.2628386

Ullakko, K., Huang, J. K., Kantner, C., O'Handley, R. C., and Kokorin, V. V. (1996). Large magnetic-field-induced strains in Ni_2MnGa single crystals. *Appl. Phys. Lett.* 69, 1966. doi:10.1063/1.117637

Wang, W., Liu, E., Kodzuka, M., Sukegawa, H., Wojcik, M., Jedryka, E., et al. (2010). Coherent tunneling and giant tunneling magnetoresistance in Co2FeAl/MgO/CoFe magnetic tunneling junctions. *Phys. Rev. B.* 81, 140402. doi:10.1103/PhysRevB.81.140402

Wang, W., Yu, J., Zhai, Q., Luo, Z., and Zheng, H. (2013). Origin of retarded martensitic transformation in Heusler Ni-Mn-Sn melt-spun ribbons. *Intermetallics* 42, 126–129. doi:10.1016/j.intermet.2013.06.002

Wijn, H. R. J. (1988). *Alloys and compounds of d-elements with main group elements*. Editors P. J. Webster and K. R. A. Ziebeck (Berlin, Germany: Springer), Vol. 19/c.

Xu, X., Ito, W., Tokunaga, M., Umetsu, R. Y., Kainuma, R., and Ishida, K. (2010). Kinetic arrest of martensitic transformation in NiCoMnAl metamagnetic shape memory alloy. *Mater. Trans.* 51, 1357–1360. doi:10.2320/matertrans.M201009

Xuan, H. C., Cao, Q. Q., Zhang, C. L., Ma, S. C., Chen, S. Y., Wang, D. H., et al. (2010). Large exchange bias field in the Ni–Mn–Sn Heusler alloys with high content of Mn. *Appl. Phys. Lett.* 96, 202502. doi:10.1063/1.3428782

Yang, B. Y., Ma, B. X., Chen, G. X., Wei, Z. J., Wu, R., Han, Z. J., et al. (2012). Structure and exchange bias of $Ni_{50}Mn_{37}Sn_{13}$ ribbons. *J. Appl. Phys.* 111, 07A916. doi:10.1063/1.3672244

Zhao, G. X., Tong, M., Shih, W. C., Li, B., Chang, C. W., Liu, W., et al. (2013). Microstructure, martensitic transitions, magnetocaloric, and exchange bias properties in Fe-doped Ni-Mn-Sn melt-spun ribbons. *J. Appl. Phys.* 113, 17A913. doi:10.1063/1.4794881

Zhao, X. G., Hsieh, C. C., Lai, J. H., Cheng, X. J., Chang, W. C., Cui, W. B., et al. (2013). Effects of annealing on the magnetic entropy change and exchange bias behavior in melt-spun Ni-Mn-In ribbons. *Scr. Mater.* 63, 250–253. doi:10.1016/j.scriptamat.2010.03.067

Conflict of Interest: The authors declare that the research was conducted in the absence of any commercial or financial relationships that could be construed as a potential conflict of interest.

Advantages of publishing in Frontiers

OPEN ACCESS
Articles are free to read for greatest visibility and readership

FAST PUBLICATION
Around 90 days from submission to decision

HIGH QUALITY PEER-REVIEW
Rigorous, collaborative, and constructive peer-review

TRANSPARENT PEER-REVIEW
Editors and reviewers acknowledged by name on published articles

Frontiers
Avenue du Tribunal-Fédéral 34
1005 Lausanne | Switzerland

Visit us: www.frontiersin.org
Contact us: frontiersin.org/about/contact

REPRODUCIBILITY OF RESEARCH
Support open data and methods to enhance research reproducibility

DIGITAL PUBLISHING
Articles designed for optimal readership across devices

FOLLOW US
@frontiersin

IMPACT METRICS
Advanced article metrics track visibility across digital media

EXTENSIVE PROMOTION
Marketing and promotion of impactful research

LOOP RESEARCH NETWORK
Our network increases your article's readership